NPS-OC-98-004

NAVAL POSTGRADUATE SCHOOL
MONTEREY, CALIFORNIA

THESIS

ANALYSIS OF EDDY RESOLVING MODEL OF THE CALIFORNIA CURRENT SYSTEM

by

Nicholas J. Cipriano

September 1998

Thesis Advisor: Mary L. Batteen

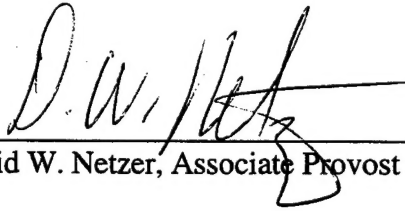**Approved for public release; distribution is unlimited.**

19981215 125

NAVAL POSTGRADUATE SCHOOL
MONTEREY, CALIFORNIA

Rear Admiral Robert C. Chaplin
Superintendent

This thesis was prepared in conjunction with research sponsored in part by the Office of Naval Research, 800 N. Quincy Street, Arlington, VA 22217.

Reproduction of all or part of this report is authorized.

Released by:

David W. Netzer, Associate Provost and Dean of Research

REPORT DOCUMENTATION PAGE

Form Approved OMB No. 0704-0188

1. AGENCY USE ONLY *(Leave blank)*	2. REPORT DATE September 1998	3. REPORT TYPE AND DATES COVERED Master's Thesis

4. TITLE AND SUBTITLE ANALYSIS OF EDDY RESOLVING MODEL OF THE CALIFORNIA CURRENT SYSTEM	5. FUNDING NUMBERS
6. AUTHOR(S) Nicholas J. Cipriano in conjunction with Mary L. Batteen and James T. Monroe	

7. PERFORMING ORGANIZATION NAME(S) AND ADDRESS(ES) Naval Postgraduate School Monterey, CA 93943-5000	8. PERFORMING ORGANIZATION REPORT NUMBER NPS-OC-98-004

9. SPONSORING/MONITORING AGENCY NAME(S) AND ADDRESS(ES) Office of Naval Research 800 N. Quincy Street, Arlington, VA. 22217	10. SPONSORING/MONITORING AGENCY REPORT NUMBER

11. SUPPLEMENTARY NOTES The views expressed in this thesis are those of the author and do not reflect the official policy or position of the Department of Defense or the U.S. Government.

12a. DISTRIBUTION/AVAILABILITY STATEMENT Approved for public release; distribution is unlimited.	12b. DISTRIBUTION CODE

13. ABSTRACT *(maximum 200 words)*

A high-resolution, multi-level, primitive equation ocean model is used to investigate the combined role of seasonal wind forcing, thermohaline gradients, and coastline irregularities on the formation of currents, meanders, eddies, and filaments in the California Current System from 22.5° N to 47.5° N. An investigation of the dynamical reasons for the generation and growth of meanders and eddies is conducted along with a sensitivity study to investigate the formation of the Davidson Current.

Model results are consistent with the generation of eddies from instabilities of the equatorward current and poleward undercurrent via barotropic and baroclinic instability processes. The meandering equatorward jet south of Cape Blanco is shown to be a continuous feature, which divides coastally-influenced water from water of offshore origin. The area off southern Baja is shown to be a highly dynamic environment for meanders, filaments, and eddies, while the area off Point Eugenia is shown to be a persistent cyclonic eddy generation region. Both the Southern California Countercurrent rounding Point Conception and the shoaling of the poleward undercurrent are shown to play important roles in generating the Davidson Current in the fall.

14. SUBJECT TERMS Primitive equation model, California Current System, currents, meanders, eddies, filaments			15. NUMBER OF PAGES 113
			16. PRICE CODE

17. SECURITY CLASSIFICATION OF REPORT Unclassified	18. SECURITY CLASSIFICATION OF THIS PAGE Unclassified	19. SECURITY CLASSIFICATION OF ABSTRACT Unclassified	20. LIMITATION OF ABSTRACT UL

ANALYSIS OF EDDY RESOLVING MODEL OF THE CALIFORNIA CURRENT SYSTEM

Nicholas J. Cipriano
Lieutenant Commander, United States Navy
B.S., United States Naval Academy, 1987

Submitted in partial fulfillment
of the requirements for the degree of

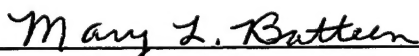## MASTER OF SCIENCE IN METEOROLOGY AND PHYSICAL OCEANOGRAPHY

from the

NAVAL POSTGRADUATE SCHOOL
September 1998

Author: _____

Nicholas J. Cipriano

Approved by: _____

Mary L. Batteen, Thesis Advisor

_____

Curtis A. Collins, Second Reader

_____

Roland W. Garwood Jr., Chairman
Department of Oceanography

iv

ABSTRACT

A high-resolution, multi-level, primitive equation ocean model is used to investigate the combined role of seasonal wind forcing, thermohaline gradients, and coastline irregularities on the formation of currents, meanders, eddies, and filaments in the California Current System from 22.5° N to 47.5° N. An investigation of the dynamical reasons for the generation and growth of meanders and eddies is conducted along with a sensitivity study to investigate the formation of the Davidson Current.

Model results are consistent with the generation of eddies from instabilities of the equatorward current and poleward undercurrent via barotropic and baroclinic instability processes. The meandering equatorward jet south of Cape Blanco is shown to be a continuous feature, which divides coastally-influenced water from water of offshore origin. The area off southern Baja is shown to be a highly dynamic environment for meanders, filaments, and eddies, while the area off Point Eugenia is shown to be a persistent cyclonic eddy generation region. Both the Southern California Countercurrent rounding Point Conception and the shoaling of the poleward undercurrent are shown to play important roles in generating the Davidson Current in the fall.

TABLE OF CONTENTS

LIST OF FIGURES

LIST OF PLATES

LIST OF TABLES

ACKNOWLEDGEMENT

I. INTRODUCTION

The California Current System (CCS) is the classical eastern boundary current (EBC) system located off the west coast of North America extending approximately from the Strait of Juan de Fuca southward to the tip of the Baja Peninsula (Hickey, 1998). As in other EBC regimes, satellite infrared sea surface temperature (SST) imagery of the CCS has revealed a complex flow structure with seasonal variations. Dominant mechanisms responsible for the observed large-scale structure within the CCS have been shown to be seasonal variations in alongshore wind stress (Bakun and Nelson, 1991), coastline irregularities (e.g., Batteen, 1997), bottom topography (e.g., Ikeda *et al.*, 1984), and temperature and salinity variations (Batteen *et al.*, 1995; Batteen and Vance, 1998).

The CCS is influenced by at least three different water masses. Cold, low salinity Pacific Subarctic Water is advected from the north while warmer, more saline North Pacific Central Water enters from the west. Warm, high salinity Southern Water is advected from the south by the poleward undercurrent (Hickey, 1998). Unlike other eastern boundary currents, salinity increases rather than decreases with depth in the CCS (Wooster and Reid, 1963).

The climatological mean CCS is comprised of several large-scale currents (Figure 1). The predominant flow is the California Current (CC), which, in the mean, is a broad (~1000 km offshore), shallow (surface to ~500 km), relatively slow (~10 cm/s), year-round equatorward current. Embedded within this basic flow are the California Undercurrent (CUC), the Davidson Current (DC), the Southern California Countercurrent

1

(SCC), and the Southern California Eddy (SCE). The CUC is a relatively narrow (~10-40 km width), weak (~2-10 cm/s), subsurface poleward flow which is strongest at ~100-300 m depth and varies seasonally. The DC is a weak, inshore, poleward surface flow north of Point Conception during fall and winter. Other poleward surface flows include the SCC south of Point Conception and the SCE shoreward of the Channel Islands within the Southern California Bight (Hickey, 1979, 1998).

Recent observational studies have shown that the CCS is not the stable system of currents with the well-defined, unchanging structure suggested by Figure 1. Rather, within the mean, large-scale structure of the CCS, there exist perturbations in the form of mesoscale meanders, eddies, and filaments, which vary both spatially and temporally (Bernstein et al., 1977; Chelton, 1984; Strub et al., 1991). Numerical modeling efforts by Batteen (1997) simulated this complex eddy-mean flow interaction within the CCS using a high-resolution, multi-level, primitive equation (PE) ocean model emphasizing the role of wind-forcing and coastline irregularities. Specifically, the seasonal variation of the alongshore component of wind stress was shown to be critical in generating realistic horizontal and vertical structures for the surface equatorward CC and the subsurface poleward CUC. Both baroclinic and barotropic instability mechanisms contributed to the generation of meanders, filaments, and eddies. Additionally, coastline irregularities were shown to help "anchor" upwelling filaments and to enhance the growth of meanders and eddies. In particular, the region off Cape Blanco was identified as the location where the inshore edge of the CC leaves the coast and develops a meandering jet to the south. In recent observational (Batteen et al., 1995) and modeling studies (Batteen and Vance,

2

1998) on the combined effect of temperature and salinity on density, it was shown that the distribution of salinity as well as temperature is important in defining the large-scale structure and circulation of the CCS. Although the modeling study of Batteen and Vance (1998), which included wind forcing, coastline irregularities, and thermohaline gradients, was able to reproduce some of the currents in the CCS (i.e., the CC and CUC), the model did not generate the DC, SCC, or SCE which are thought to originate south of the model domain used by Batteen and Vance (1998).

In this study, the model of Batteen (1997) and Batteen and Vance (1998), originally restricted to poleward of 35° N, is expanded by extending the model domain southward to 22.5° N. As a result, the entire CCS region from Baja to the Washington-Canada border is included, which allows all of the major currents of the CCS shown in Figure 1 as well as filaments, meanders, and eddies to be generated. Besides investigating the combined role of seasonal wind forcing, thermohaline gradients, and a realistic coastline in the generation of these features, the dynamical reasons for the generation and growth of meanders and eddies will be explored using the energy analysis technique of Batteen et al. (1992).

With the larger model domain, two key issues that have not yet been resolved can be addressed using the results of the model simulations. The first issue to address is the seasonal variability off the Baja peninsula, which, with the possible exception of northern Baja (which has been regularly sampled by CalCOFI and covers the region north of Point Baja to the U.S.-Mexico border), remains a data sparse region with a poorly known

seasonal cycle (Hickey, 1998). The second issue to address is the seasonal appearance and origin of the DC, which is not fully understood. For this, in a sensitivity study, results from a second experiment with a straight coastline south of ~35° N will be compared to the basic experiment and examined to determine the importance of coastline geometry within the California Bight to the development of the DC.

This study is organized as follows: section 2 describes the numerical model, the forcing, and the experimental conditions used in the basic experiment; section 3 includes analyses of the results of the model simulations and of the generation mechanisms for the meanders and eddies in the CCS; section 4 utilizes model results to describe the seasonal variability off the Baja peninsula and the seasonal appearance and origin of the DC.

II. MODEL DESCRIPTION

A. MODEL EQUATIONS AND METHOD OF SOLUTION

The PE model in this study was originally a coarse resolution model used in closed basin studies by Haney (1974). It has recently been adapted by Batteen (1997) for eddy-resolving, limited EBC regions with open boundaries to the north, south, and west. The model is multi-level, non-adiabatic, and uses the beta-plane approximation. It has both baroclinic and barotropic velocity components and uses the hydrostatic and Boussinesq approximations as well as a rigid lid. The governing equations are as follows:

$$\frac{du}{dt} = \frac{-1}{\rho_0}\frac{\partial p}{\partial x} + fv - A_M \nabla^4 u + K_M \frac{\partial^2 u}{\partial z^2} \tag{1}$$

$$\frac{dv}{dt} = \frac{-1}{\rho_0}\frac{\partial p}{\partial y} - fu - A_M \nabla^4 v + K_M \frac{\partial^2 v}{\partial z^2} \tag{2}$$

$$\frac{\partial u}{\partial x} + \frac{\partial v}{\partial y} + \frac{\partial w}{\partial z} = 0 \tag{3}$$

$$\frac{\partial p}{\partial z} = -\rho g \tag{4}$$

$$\rho = \rho_0 [1 - \alpha(T - T_0) + \beta(S - S_0)] \tag{5}$$

$$\frac{dT}{dt} = -A_H \nabla^4 T + K_H \frac{\partial^2 T}{\partial z^2} \tag{6}$$

$$\frac{dS}{dt} = -A_H \nabla^4 S + K_H \frac{\partial^2 S}{\partial z^2} \tag{7}$$

5

In the above equations, t is time and (x,y,z) is a right-handed Cartesian coordinate system with x pointing toward shore, y alongshore, and z upward. The corresponding velocity components are (u,v,w). T, S, and p are temperature, salinity and pressure, respectively, and ρ is density. Table 1 provides a list of other symbols found in the model equations, as well as values of constants used throughout the study.

A space-staggered B-scheme (Arakawa and Lamb, 1977) is used for the horizontal finite differencing. This scheme has been shown by Batteen and Han (1981) to be appropriate when the grid spacing is approximately the same order as, or less than, the Rossby radius of deformation. The horizontal grid spacing is 9 km in the east-west direction and 11 km in the north-south direction, while the internal Rossby radius of deformation is ~30 km.

The model uses ten vertical layers, with constant z-levels, at depths of 13, 46, 98, 182, 316, 529, 870, 1416, 2283, and 3656 m. This vertical scheme is designed to concentrate more layers above the thermocline in the dynamically active portion of the ocean.

The model domain (Figure 1) encompasses the west coast of the United States and the Baja Peninsula, from 22.5° N to 47.5° N (2816 km alongshore), and from 107.5° W to 132.5° W offshore (2304 km cross-shore). The coastal boundary of the model domain is closed, and has both tangential and normal velocity components set to zero. To isolate the role of wind forcing from the possible coupled effect of wind forcing and topography (which will be considered in a separate study), bottom topography has been omitted and

the eastern boundary is modeled as a vertical wall. The constant depth used in the model is 4500 m. A modified version of the radiation boundary conditions of Camerlengo and O'Brien (1980) is used for the open boundaries to the north, south, and west with some spatial smoothing applied in the vicinity of these boundaries (Batteen, 1997).

Biharmonic lateral heat and momentum diffusion is used in the model with the same choice of coefficients (i.e., 2.0×10^{17} cm^4/s) as in Batteen (1997). Holland (1978) showed that biharmonic diffusion acts predominantly on submesoscales, while Holland and Batteen (1986) found that baroclinic mesoscale processes can be damped by Laplacian lateral heat diffusion. As a result, the use of biharmonic lateral diffusion should allow mesoscale eddy generation via barotropic (horizontal shear) and/or baroclinic (vertical shear) instability mechanisms. As in Batteen (1997), weak (0.5 cm^2/s) vertical eddy viscosities and conductivities are used and bottom stress is parameterized by a simplified quadratic drag law (Weatherly, 1972).

The method of solution is straightforward with the rigid lid and flat bottom assumptions because the vertically integrated horizontal velocity is subsequently nondivergent. The vertical mean flow can be described by a streamfunction which can be predicted from the vorticity equation, while the vertical shear currents can be predicted after the mean vertical flow is subtracted from the original equations. The other variables, i.e., temperature, salinity, vertical velocity, and pressure, can be explicitly obtained from the thermodynamic energy equation (6), salinity equation (7), continuity equation (3), and hydrostatic equation (4) respectively (for more complete details on the method of solution see Batteen, 1997).

7

B. FORCING CONDITIONS AND EXPERIMENTAL DESIGN

Previous experiments by Batteen *et al.* (1989) investigated the role of steady alongshore, upwelling-favorable winds, with and without alongshore variability, on the generation of eddies, currents, meanders, and filaments in the CCS. More recently, Batteen (1997) studied the contributions of seasonal wind forcing and irregular coastline geometry to the generation of these features in the CCS between 35° N and 47.5° N. Following Batteen (1997), seasonal wind forcing and irregular coastline geometry, along with thermohaline gradients as used by Batteen and Vance (1998), will be used to investigate the generation of similar features throughout a larger domain encompassing the entire CCS (i.e., between 22.5° N and 47.5° N).

To explore the effects of seasonal wind forcing, the model is forced from rest with climatological wind fields from a 2.5 by 2.5 grid of European Centre for Medium-Range Weather Forecasts (ECMWF) near-surface wind analyses (Trenberth *et al.,* 1990). The monthly mean stresses based on twice daily wind analyses from 1980-1989 have been interpolated spatially to the 9 by 11 km model resolution and temporally to daily wind values.

Sample wind fields used in the basic study are shown in Figure 2, which depicts the seasonal influence and migration of flow around the North Pacific Subtropical High over the area encompassed by the model domain. Figure 2a shows a divergence of flow at the coast in the vicinity of ~40° N during the winter as the winds circulate

anticyclonically around the Subtropical High to the south and cyclonically around the Aleutian Low to the north. By spring (Figure 2b), the Subtropical High has begun its westward and northward expansion, producing increased equatorward winds over most of the model domain and causing the divergence of flow to move north to ~44° N, off the Washington coast. In July (Figure 2c), equatorward, upwelling-favorable winds dominate along the entire coastline as the Subtropical High reaches its maximum extent. Figure 2d shows a decrease in magnitude of equatorward winds during fall as the Subtropical High begins to recede southward.

The effects of thermohaline gradients in the CCS are included using monthly temperature and salinity climatology from Levitus *et al.* (1994) and Levitus and Boyer (1994) to initialize the model, and once a day to force the model at the western boundary (132.5° W). Forcing occurs over the upper seven levels, which are initially assumed to be zonally homogeneous. Since the lower three levels do not exhibit significant horizontal variation in temperature and salinity, constants are assumed for each level. Temperature values used for levels 8 (1416 m), 9 (2283 m), and 10 (3656 m) are 2.56 C, 2.08 C, and 2.00 C, respectively, while the salinity constant used for the lower three levels is 34.7. Only the upper layer (13 m and 46 m) temperature forcing conditions for the northern (47.5° N) and southern (22.5° N) boundaries show significant seasonal variability with a temperature maximum in late summer to early fall and minimum in late winter to early spring throughout the region (e.g., Figure 3). Below these depths, both the seasonal temperature fluctuations and temperature gradient weaken. Conversely, salinity forcing

conditions at all seven levels, which show less (more) saline water to the north (south), have no significant seasonal cycle (not shown).

The design of the study is as follows. To focus on the combined role of seasonal wind forcing and thermohaline gradients, model integrations start from a state of rest and once a day the model is updated with ECMWF winds and, at the western boundary with temperature and salinity fields. In the basic experiment, a realistic North American coastline is used to include the effects of irregular coastline geometry over the entire CCS region. In the second experiment, a straight coastline south of ~35° N is used to isolate the effects of coastline geometry within the California Bight. To allow the model to reach a state of quasi-equilibrium, the basic experiment is run for three years.

C. ENERGY ANALYSIS TECHNIQUE

The energy analysis technique used is the same as that used and described by Batteen *et al.* (1992) and is based on that of Han (1975) and Semtner and Mintz (1977). This analysis is done to gain a better understanding of the types of energy transfer during unstable flow in the CCS. A brief summary of the method follows.

Kinetic energy is calculated for the horizontal components. After a quasi-steady state is reached where the total kinetic energy is nearly constant, mean kinetic energy (MKE) and eddy kinetic energy (EKE) are calculated using the sum of squared mean and horizontal fields, respectively. Next, the available potential energy is calculated and used to determine when a quasi-steady state is reached and when statistics should be collected.

10

Then both mean and eddy available energies are computed. The baroclinic and barotropic energy transfers, defined by Batteen *et al.* (1992), are used to argue for the type of instability mechanism (e.g., baroclinic, barotropic, or mixed) leading to the initial eddy generation.

III. RESULTS OF THE BASIC EXPERIMENT

A. SPIN-UP PHASE

Due to the combination of thermohaline gradients and wind forcing, different oceanic responses are expected depending on the season. In the winter, in the poleward end of the model domain, the large meridional high to low atmospheric pressure gradient due to the decrease of temperature poleward (Figure 3) establishes an onshore geostrophic flow, while the poleward wind stress results in an onshore Ekman flow. On approaching the eastern boundary, the onshore flow turns and forms a poleward coastal current (e.g., Figure 4a). In the equatorward end of the model domain, the smaller pressure gradient (due to the smaller warm to cold temperature gradient) and the equatorward wind stress results in weak onshore geostrophic flow, offshore Ekman flow, and a coastal equatorward surface current (e.g., Figure 4b)

During the upwelling season (~April to September), the combination of a weakened pressure gradient and increased equatorward winds over the entire model domain lead to a strengthening of equatorward flow all along the coast and a weakening (strengthening) of onshore (offshore) flow. An equatorward coastal jet is discernible as a relatively narrow coastal flow in the north, which broadens in scope as it progresses southward (e.g., Figures 5a and 5b). Maximum speeds in the northern half of the domain are ~20 cm/s whereas current speeds associated with cyclonic eddy activity in the south are ~30-50 cm/s. There is also an inshore poleward flow discernible at ~300 m depth

13

with maximum speeds of ~15-20 cm/s which can be traced northward across the entire model domain (not shown).

A cross-section of meridional velocity at day 195 (Figures 6b and 6c) shows the typical vertical structure of the equatorward coastal jet and poleward undercurrent during the upwelling season from the northern portion of the domain through the southern portion of the domain. In the northern portion (Figure 6b) the equatorward coastal jet axis is within ~60 km of the coast and extends to ~400 m depth with a surface velocity of ~15 cm/s. A relatively weaker poleward undercurrent with a core velocity of ~5 cm/s at ~300 m depth is also seen. The offshore extent of the core of the undercurrent is confined to ~50 km of the coast. In the southern portion of the domain (Figure 6c), the coastal jet axis extends to ~250 m depth with a surface velocity of ~25 cm/s. A poleward undercurrent with a surface velocity of ~5 cm/s is found within ~100 km of the coast.

As the coastal jet and undercurrent become fully established (from day ~195 to day ~285) the currents become unstable and form meanders (e.g., Figures 5a-5b) as well as cold, upwelling filaments. As the meanders intensify, eddies are formed in the coastal, equatorward region of the domain (Figure 5b), due to the vertical and horizontal shear instabilities between the equatorward jet and the poleward undercurrent. The eddies are predominantly cold core and cyclonic, on the order of 100 km in diameter, and regularly extend to ~50-100 km off the coast. Throughout the upwelling season, which corresponds to the period of maximum equatorward wind stress (Figure 2), meanders, filaments, and eddies continue to develop equatorward of ~44° N (not shown).

14

In the fall, the Aleutian Low begins to deepen and the Subtropical High migrates toward its wintertime position in the south. With this transition, poleward wind stress returns to the northern portion of the model domain as the regional pressure gradient strengthens. The poleward flow near the coast fluctuates in depth and intensity from the northern to the southern portion of the model domain (e.g., Figures 7a-7b). For example, off Cape San Lazaro, at ~25° N, a strong poleward undercurrent is discernible below ~300 m depth with speeds up to ~15 cm/s (Figure 7a), while farther north, off Cape Blanco, ~43° N, poleward flow is found throughout the water column at the coast with a core velocity of ~7.5 cm/s centered at ~320 m depth (Figure 7b).

B. ANALYSIS OF EDDY GENERATION MECHANISMS

The dynamical reasons for the generation and stability of eddies in the CCS are examined using the energy techniques used and described by Batteen *et al.* (1992). From the energy transfer analysis, the location and magnitude of baroclinic and barotropic transfers can be found and examined to argue for the type of instability mechanism (e.g., barotropic, baroclinic, or mixed) which leads to the initial eddy generation. Analysis of typical cross-section of the meridional velocity component (e.g., Figures 6 and 7) show that there is considerable horizontal and vertical shear in the upper layer currents in the CCS. Barotropic instability can result from horizontal shear in the currents, while baroclinic instability can result from vertical shear in the currents. As a result, both types

15

of instability (mixed) can be present. Energy transfer calculations, which consist of barotropic (mean kinetic energy to eddy kinetic energy) and baroclinic (mean potential energy to eddy potential energy to eddy kinetic energy) components, were performed over the time period when the meanders and eddies developed.

Results from the instability analysis of baroclinic and barotropic transfers for days 90 to 120 (not shown) show the presence of both barotropic and baroclinic instability mechanisms (i.e., mixed). Although mixed instability mechanisms are present, baroclinic instability is the dominant generation mechanism for cyclonic meander development which, ultimately leads to the formation of cyclonic eddies as seen north of Point Eugenia by day 195 (Figure 5b). This analysis is consistent with Figure 6a, which shows a relatively stronger vertical than horizontal gradient in upper layer current shear at the time of the initial instability.

The instability analysis of barotropic and baroclinic transfers for days 180-195 in the northern portion of the domain (Plates 1a and 1b) show that there are generally coincident maxima of barotropic and baroclinic instability along most of the coast from ~35° N – 41° N. Note that the scales used in Plates 1a and 1b are different in order to highlight areas of relative maxima. These regions of baroclinic and barotropic (i.e., mixed) instability ordinarily correspond to areas of meander and eddy development that occur along the coast by day 285 (e.g., Figure 8a). It can be seen that the magnitude for each area of baroclinic instability is generally greater than its coincident area of barotropic instability, indicating a dominant baroclinic energy source and a weaker barotropic energy source. This is consistent with vertical cross-sections in this region

16

(e.g., Figure 6b) which shows that although there is both vertical and horizontal shear, the stronger vertical gradient dominates the horizontal gradient in the upper layers.

The instability analysis of barotropic and baroclinic transfers for days 180-195 in the southern portion of the domain (Plates 1c and 1d) also shows coincident maxima of barotropic and baroclinic instability along the coast extending throughout the domain. Again, the scales are different and baroclinic instability once again dominates. These results are, as expected, consistent with vertical cross-sections in the region (e.g., Figure 6c) which show that strong vertical gradients, in general, dominate horizontal gradients in the upper layers. An exception occurs near Point Eugenia (~28° N) where the magnitudes of barotropic instability are comparable to those of baroclinic instability which results in a mixed instability. The relatively strong horizontal shear off Point Eugenia at ~28° N, 116° W, compared to regions north and south, can be seen in Figure 5b.

The instability analysis of barotropic and baroclinic transfers for days 270-285, near the end of the upwelling season, in both the northern and southern portion of the domain (Plates 2a-2d) show that, although both baroclinic and barotropic instability are still present, barotropic instability dominates. The increase in barotropic instability can be qualitatively seen by comparing Figure 5 with Figure 8, which illustrates that a general increase in horizontal shear from days 195 to 285 has occurred throughout the domain. In conclusion, as the model spins-up, although both baroclinic and barotropic instability mechanisms are present, in the early generation period baroclinic instability dominates while barotropic instability is the dominant mechanism in the later period.

17

C. QUASI-EQUILIBRIUM PHASE

Longer run times (~3 years) with model output fields averaged every 3 days for the months of January, April, July, and October illustrate the seasonal variability and complex structure of the CCS. By year 3, the model CC core takes the form of a meandering jet embedded with numerous eddies and upwelling filaments (Plates 3a-3d). Although the mean direction of flow remains equatorward near the surface, the circulation contains large zonal components with relatively intense onshore and offshore transports.

Model results show that in winter (Plate 3a), flow at the coast meanders equatorward and advects colder water near the coast offshore and warmer water from the west onshore throughout the model domain. Both cyclonic and anticyclonic eddies exist on either side of the equatorward coastal jet and closed, cold-core eddies on the order of 100 km in diameter are present off San Francisco at ~38° N, 126° W, and in the southwest corner of the domain at ~25° N, 129.5° W. The coldest water found in the model is located adjacent to the southern Baja coastline coincident with persistent northwesterly winds due to the wintertime position of the Subtropical High (Figure 2a). Average current speeds of the equatorward surface jet range from ~10-50 cm/s, consistent with observations of the CC using drifters (Davis, 1985).

In spring (Plate 3b), meander activity is more pronounced along the model coastline and more closed eddies exist offshore within the core of the equatorward model

18

CC. Eddies present in January have propagated westward at speeds of ~1-3 km/day, consistent with Rossby wave propagation speeds. The coldest water has moved north up the Baja and Southern California coastline in conjunction with the seasonal migration of the Subtropical High and subsequent expansion of upwelling-favorable winds. Similarly, in the model, spring marks an increase in magnitude of the equatorward surface jet from speeds present in January. Using CalCOFI data, Lynn and Simpson (1987) noted that a large-scale intensification in equatorward flow along much of the coastal CCS accompanied the onset of springtime conditions.

In summer (Plate 3c), temperatures adjacent to the coast in the northern portion of the model (i.e., above ~40° N) have decreased as upwelling-favorable winds now approximately parallel the coastline throughout the domain (Figure 2c). Evidence of cold, offshore-flowing, upwelling filaments exists in the vicinity of Cape Blanco, Cape Mendocino, south of Point Sur, in the Southern California Bight, and below Point Eugenia. These filaments extend ~80- 200 km offshore and merge with the meandering equatorward jet that has speeds of ~30-50 cm/s and alongshore wavelengths of ~100-300 km, consistent with Brink and Cowles (1991). An example of a mesoscale disturbance embedded within the CCS is illustrated by the cyclonic meander that forms off Point Eugenia in January (Plate 3a), intensifies in April (Plate 3b), and breaks away by July (Plate 3c) to propagate southwestward in the CC. Bernstein *et al.* (1977) noted similar mesoscale activity off Point Eugenia using data from CalCOFI surveys of the CCS taken from April to July, 1952. In the vicinity of the U.S.-Mexico border (~32.5° N) within the

19

Southern California Bight, a division of flow is evident, consistent with Reid (1963), in the equatorward jet as a portion of the jet turns shoreward (Plate 3c). This division of flow is consistent with the summertime formation of the SCE (Lynn and Simpson, 1987).

The spring and summer results are in good agreement with recent satellite imagery (Strub *et al.*, 1991; Strub and James, 1995), field studies using Lagrangian drifters (Barth *et al.*, 1994; Barth and Smith, 1996a,b), and with the hypothesis that the offshore separation of the equatorward coastal jet in the vicinity of Cape Blanco marks the start of a continuous meander along a temperature front that can be traced equatorward throughout the entire CCS during spring and summer. In particular, both the model results and Strub and James (1995) (hereafter referred to as SJ95) show the connection between the equatorward flow off Oregon and the jet that meanders along the temperature front off California, i.e., the equatorward flow off Oregon and the meandering jet are part of a continuous flow that originates from farther north. In particular, SJ95 (see Figure 2a of SJ95) and the model results (Plate 3c) both show a narrow jet that is found on the offshore side of the temperature front at ~20-50 km off central Oregon at ~44.5° N. Additionally, the similar presence of coastal equatorward flow leaves the coast in the vicinity of Cape Blanco. Downstream from Cape Blanco, both results show the equatorward jet and temperature front that form a large meander around Cape Mendocino and then flows southward toward the coast where it turns south-southwest near Point Arena. Both results also show the jet and its associated temperature front between Cape Mendocino and Point Arena formed inshore of ~125° W.

By early fall (Plate 3d), as the upwelling system begins to weaken with the equatorward migration of the Subtropical High, the sharp nearshore temperature front present during summer north of Cape Blanco has become more diffuse. The coastal equatorward surface jet in this region is now oriented farther offshore and embedded streams of colder water flow southwestward into a cold-core eddy west of Cape Mendocino. South of Point Conception, the division of flow is more pronounced as a branch of the equatorward surface jet rotates onshore and poleward while the main portion of the jet continues southward offshore. This flow structure within the Southern California Bight coincides with a seasonal maximum in the SCE from summer to early fall (Hickey, 1998). As in January (Plate 3a), in the vicinity of Point Eugenia, a cyclonic meander in the equatorward jet is discernible. In time (not shown), this meander intensifies, closes off, and propagates southwestward through the stream.

D. ANALYSIS OF ENERGETICS

Horizontal maps of the upper layer mean kinetic energy (MKE) and eddy kinetic energy (EKE), averaged monthly in the quasi-equilibrium phase, are shown in Figures 9 (11) and 10 (12) in the summer and early fall in the northern (southern) portion of the model domain. Maps of MKE and EKE are suggestive of where the mean and eddy energy sources are to be found (Holland *et al.*, 1983).

A comparison of MKE (Figures 9 and 11) with the mean velocity field (Plate 3c and 3d) shows that high values of MKE are found along the axis of the meandering equatorward jet, in the coastal regions where the coastal current is the strongest, and in regions of cyclonic eddies offshore of the jet at ~41° N, 128° W, ~38° N, 129° W, ~34° N, 124° W, and ~28° N, 125° W. Maximum values of MKE are found in regions where mean equatorward flow on the eastern (western) side of anticyclonic (cyclonic) eddies enhances the flow between cyclonic and anticyclonic eddy pairs. An example of this can be seen by comparing the eddy pair at ~40.5° N 126° W off Cape Mendocino (Plate 3c) with the corresponding MKE maximum (Figure 9a). An additional example of this can be seen by comparing the eddy pair at ~25° N, 119.5° W off Cape San Lazaro (Plate 3c) with the corresponding MKE maximum (Figure 11a). MKE maxima can also be seen in regions of cyclonic eddies offshore of the jet. For example, Plates 3c and 3d show increased current velocities on the western sides of the offshore cyclonic eddies at ~41.5° N, 128.5° W and at ~38° N, 129° W which correspond to areas of higher MKE in Figures 9a and 9b.

Within the northern portion of the domain, a comparison of EKE (Figure 10) with the mean velocity field (Plate 3c and 3d) shows high values of EKE where the jet meanders off Cape Blanco at ~43° N, 126° W and on the eastern and western sides of offshore cyclonic eddies at ~41° N, 128° W and at ~38° N, 128.5° W. High EKE values are also located along the axis of the coastal equatorward jet at ~45° N, 124.5° W and in the region of the inshore cyclonic eddy at ~38° N, 124° W. Within the southern domain, a comparison of EKE (Figure 12) with the mean velocity field (Plates 3c and 3d) shows

22

maximum EKE values at 33° N, 118° W where the jet meanders toward the Southern California Bight, in the vicinity of ~28.5° N, 116° W where a cyclonic eddy is generated off Point Baja between September and October, and farther off Point Baja at ~30.5° N, 120° W where another cyclonic eddy is generated between September and October. Regions of high model EKE values correspond to areas where eddies are likely to be generated, such as off Cape Blanco, offshore and downstream of Cape Mendocino, Point Arena, and Point Baja, in the Southern California Bight, and in the coastal indentations on either side of Point Eugenia. A time series of EKE (Figures 10a-10c), depicts higher values of EKE present during late summer. For example, the maximum values of EKE for the eddy located at ~38° N, 129° W in July increased from ~25-50 cm^2/s^2, (Figure 10a), to ~75-100 cm^2/s^2 by September (Figure 10b).

A comparison of MKE (Figures 9 and 11) with EKE (Figures 10 and 12) show that maximum MKE and EKE values generally occur in the same vicinity. Additionally, for the entire model domain, the magnitudes of MKE are larger than the magnitudes of EKE for all months (including those not shown). This is consistent with the results of the model simulations which showed that eddies are generated from instabilities of the mean CC and CUC via baroclinic and/or barotropic instability processes.

Kelly *et al.* (1998) recently examined altimeter, moored ADCP, and drifter data for the CCS to determine the spatial and temporal structure of eddy fields and to investigate the variability of near-surface EKE in the CCS west of 124° W between 33° N-40.5° N. A qualitative and quantitative comparison of EKE results from the present

study with their observations shows good correlation. Both Kelly *et al.* (1998) and the model results show higher values of EKE in late summer to early fall between ~36° N- 40° N and west of ~124° W, coincident with increased equatorward flow, along with minimum values in the spring (not shown). Specifically, maximum (minimum) EKE values observed by Kelly *et al.* (1998) within their study area were ~0.02 m^2/s^2 (0.01 m^2/s^2) while maximum (minimum) values in the model were ~0.03 m^2/s^2 (0.01 m^2/s^2). These values are also similar to Strub *et al.* (1997). Additionally, both studies reveal a tendency of EKE maxima to propagate westward in time. For example, the EKE maximum located at ~38° N, 128° W in July propagates to ~38° N, 130° W by October. Thus, the results of the model instability analysis are consistent with Kelly *et al.* (1998) who also suggests that the baroclinic instability mechanism is the dominant forcing mechanism in the generation of eddies.

IV. MODEL SIMULATION APPLICATIONS

An additional goal of this study is to utilize model results to address two key issues that have not yet been resolved. The first issue is the seasonal variability off the Baja peninsula which, remains a data sparse region with a poorly known seasonal cycle (Hickey, 1998). The second issue to address is the seasonal appearance and origin of the DC which, is not fully understood. For the second issue, the results of a sensitivity study will be used.

A. SEASONAL VARIABILITY OFF THE BAJA PENINSULA

Lynn and Simpson (1987) have described the flow and water mass characteristics off the Baja Peninsula based on analyses of 23 years of CalCOFI data. Surface equatorward flow is strongest along the coast, showing significant seasonal variability, with maximum flow of ~20 cm/s occurring in March and April. This inshore equatorward flow is present most of the year with no spring transition as observed north of the border. The near-surface water mass characteristics described by Lynn and Simpson (1987) include a low-salinity minimum at ~50-100 m depth (Reid et al., 1958) close to the coast which indicates the core of the CC.

In the model, the flow results show, consistent with Lynn and Simpson (1987), that in spring and summer (e.g., Plates 3b and 3c), the equatorward surface jet off Baja is

strong and close to the coast, while during fall and winter (e.g., Plates 3a and 3d) the jet weakens, meanders farther offshore, and is embedded in a more chaotic flow regime. The model also supports maximum equatorward current speeds of ~20-30 cm/s offshore during spring (e.g., Plate 3b), coincident with the strongest equatorward wind speeds (Figure 2b). The water mass characteristics of the model simulation show, consistent with Lynn and Simpson (1987) and Reid *et al.* (1958), that south of Point Eugenia, a low salinity minimum of ~33.7 (Figure 13) is present to ~50 m depth.

The region southeast of Point Eugenia, which represents the largest coastline perturbation along the Baja Peninsula, is the location of a seasonally intensifying cyclonic eddy such that return flow north of the eddy center transports warmer water hundreds of kilometers offshore between October and January (Lynn and Simpson, 1987). The model shows that Point Eugenia and the region to the south are areas of strong seasonal variability as well as a generation region for cyclonic eddies. In January of year 3 (Plate 3a), an inshore branch of the equatorward surface jet with speeds as high as ~25 cm/s turns away from the coast in the vicinity of Point Eugenia to rejoin the main stream offshore, indicating development of a cyclonic eddy. In April (Plate 3b), the cyclonic meander is better developed and has begun to detach from the vicinity of Point Eugenia. By July (Plate 3c), the meander has closed off to form a cold-core eddy which has propagated southwestward and is now centered at ~25° N, 118.5 ° W. A thin filament of colder water extends south from Point Eugenia, transported by the high-speed inshore near-surface equatorward flow. Additionally, cyclonic turning is once again evident in the equatorward surface jet, but at a slightly different location from January, west-

26

northwest of Point Eugenia. By October (Plate 3d), cyclonic turning to the west-northwest has further intensified and approaches the pattern shown for January (Plate 3a). Note that in January (Plate 1a), a cyclonic eddy centered at ~26° N, 123 W has also formed and propagated westward in time from the same generation area. Thus, according to model results, Point Eugenia appears to play a significant role in cyclonic eddy generation and subsequent westward propagation.

Although a data sparse region, the area off southern Baja is believed to be a highly dynamic environment for meanders, filaments, and eddies (Lynn and Simpson, 1987; Poulain and Niiler, 1989; Poulain, 1990; Niiler *et al.*, 1989). Model results from year 3 support this description for the region south of Point Eugenia. Shoreward anticyclonic meanders in the equatorward surface jet (Plates 3a and 3b), sharp temperature fronts alongshore and offshore-flowing cold filaments (Plates 3c and 3d), combined with the flow field effects of cyclonic eddies detaching from Point Eugenia to propagate southwestward, all contribute toward a highly variable and complicated current structure in the model.

An example of near-surface and subsurface variability in the model for this area is illustrated through cross-sections of mean meridional velocity taken at 25° N, in the vicinity of Cape San Lazaro. In January (Figure 14a), equatorward flow persists near the surface with a maximum of ~25 cm/s nearshore and a second maximum of ~35 cm/s farther offshore. A poleward undercurrent structure is present within ~60 km of the coast with a maximum of ~10 cm/s below ~300 m depth. In April (Figure 14b), equatorward

27

flow is still present nearshore but adjacent poleward flow offshore is now surface-intensified to ~25 cm/s and extends throughout the upper water column, indicating the presence of an anticyclonic eddy nearshore. Farther offshore, the equatorward jet has intensified to ~50 cm/s in response to the occurrence of maximum equatorward winds in spring. By July (Figure 14c), alternating poleward and equatorward flow patterns are discernable, which are consistent with the presence of a cyclonic eddy near the coast and an anticyclonic eddy offshore. By October (Figure 14d), the nearshore cyclonic rotation has migrated slightly westward, giving way to a narrow band of surface-intensified equatorward flow of ~15 cm/s alongshore.

B. SEASONAL APPEARANCE AND ORIGIN OF THE DAVIDSON CURRENT

Chelton (1984) used 23 years of hydrographic measurements off Point Sur and Point Conception to show that in both locations the average poleward geostrophic flow extends to the surface from ~October to February. Lynn and Simpson (1987) refer to the seasonal change in direction of the average surface geostrophic flow, from equatorward to poleward, that occurs within ~150 km of the coast during fall and winter as the Inshore Countercurrent (IC) instead of the DC and suggest that the appearance in fall and winter of the IC is associated with the shoaling of the CUC. According to Hickey (1979, 1998), this poleward flow can be continuous around Point Conception. She notes that south of Point Conception, a branch of the equatorward CC turns shoreward then poleward and calls this flow the SCC if it rounds Point Conception and the SCE during periods when it

exists as a closed circulation within the Southern California Bight. She also points out that the SCC has a seasonal maximum which coincides with the development of the DC north of Point Conception, but that evidence also exists which attributes the DC to a shoaling of the CUC (Pavlova, 1966; Huyer and Smith, 1974).

The results of the basic experiment show that, consistent with Chelton (1984), off both Point Sur (~36.5° N) and Point Conception (~34.6° N) the average poleward flow at the coast extends throughout the upper water column from ~October to February (e.g., Figures 15a and 15b). The results also show, consistent with Lynn and Simpson (1987), the seasonal transition of the poleward undercurrent, from weak subsurface flow nearshore, to strengthening and shoaling surface poleward flow, as illustrated at 32° N in Figures 16a-16c. In September (Figure 16a), weak (~2.5 cm/s) poleward flow is centered at ~175 m depth and underlies equatorward flow at the surface. By October (Figure 16b), poleward flow extends to the surface with a core maximum of ~5 cm/s centered at ~40 m depth. By November (Figure 16c), a relatively strong coastal surface poleward current of ~12.5 cm/s is discernible.

There is also appreciable evidence in the model to support a continuous surface poleward flow (i.e., the SCC as illustrated in Figure 1) from the Southern California Bight region to north of Point Conception, which according to Hickey (1998) is caused by a wrap-around of the divergent branch of the CC. In particular, inshore poleward flow is shown to be continuous around Point Conception as illustrated for November in Figures 17a (south of Point Conception in the Southern California Bight region), 17b (off Point

Conception), and 17c (north of Point Conception). Thus, the basic experiment was able to generate surface poleward flow (i.e., the DC), which can be attributed to both the shoaling of the CUC (as in Figure 16) and to SCC rounding Point Conception (as in Figure 17).

To determine if the continuous poleward flow around Point Conception is dependent on the irregular coastline geometry of the Southern California Bight, a second experiment was run. The second experiment is identical to the basic experiment except that a straight coastline south of Point Conception (~35° N) is used (see Figure 18 for the coastline geometry). By comparing and contrasting the results of both experiments, we gain a better understanding of the importance of irregular coastline geometry south of Point Conception in the formation of surface poleward flow.

As expected, the initial oceanic response to the combination of thermohaline gradients and wind forcing results in a poleward (equatorial) flow in the northern (southern) portion of the model domain. By spring with the arrival of the North Pacific High along the west coast, surface equatorward flow extends through the model domain. A coastal, poleward undercurrent develops below the surface equatorward current, initially in the equatoward end of the model domain and, during the upwelling season, along the entire coast. During the summer and early fall as the coastal jet and undercurrent become fully established, the currents become unstable and develop meanders, eddies, and filaments in the equatorward end of the model domain (e.g., Figure 18).

Similar to the basic experiment, in the fall and winter, the coastal poleward undercurrent subsequently strengthens and shoals (e.g., Figures 19a-19c). By September (Figure 19a), poleward flow of ~7.5 cm/s, underlying equatorward flow at the surface, is generated with its core centered below ~500 m depth. By October (Figure 19b) the core of the undercurrent strengthens to ~12.5 cm/s below ~500m depth. By November (Figure 19c), a coastal poleward current of ~7.5 cm/s is present at the surface.

Unlike the basic experiment, a continuous inshore surface poleward flow around Point Conception during the fall and winter (or any other season) is not generated. For example, south of Point Conception, from ~33.5° N to ~34.5° N, inshore surface poleward flow is present (e.g., Figure 20a). Off Point Conception, from ~34.6° N to ~35.1° N, there is inshore surface equatorward flow (e.g., Figure 20b). North of Point Conception, from ~35.2° N to ~36° N inshore surface poleward flow is again discernible (e.g., Figure 19c).

A comparison of the two experiments in relation to surface poleward flow (i.e., the DC) shows that both model simulations generate a strengthening and shoaling of the poleward undercurrent nearshore, while only the basic experiment generates a continuous inshore surface poleward flow around Point Conception. The effect of irregular coastline geometry, specifically the Southern California Bight, is thus shown to play an important role in generating continuous surface poleward flow around Point Conception. Based on these results, both the shoaling of the CUC and the SCC rounding Point Conception contribute to the formation of the DC.

Overall, results from the model simulations showed that the combined effects of seasonal wind forcing and thermohaline gradients along with a realistic coastline led to the generation of all of the major currents of the CCS as well as the formation of filaments, meanders, and eddies. The eddies were shown to be generated from instabilities of the CC and CUC via barotropic and baroclinic instability processes. The relatively large magnitudes of MKE compared to those for EKE were consistent with the hypothesis that eddies are driven by the mean flow instead of the mean flow driving the eddies.

With the larger model domain, the model results showed that south of Cape Blanco the equatorward jet was a continuous feature, meandering offshore and onshore, and divided coastally-influenced water from water of offshore origin. The area off southern Baja was shown to be a highly dynamic environment for meanders, filaments, and eddies, while the area off Point Eugenia, which represents the largest coastline perturbation along the Baja peninsula, was shown to be a persistent cyclonic eddy generation region. Lastly, the results of the sensitivity study showed that both the SCC rounding Point Conception and the shoaling of the poleward undercurrent play important roles in generating the DC in the fall.
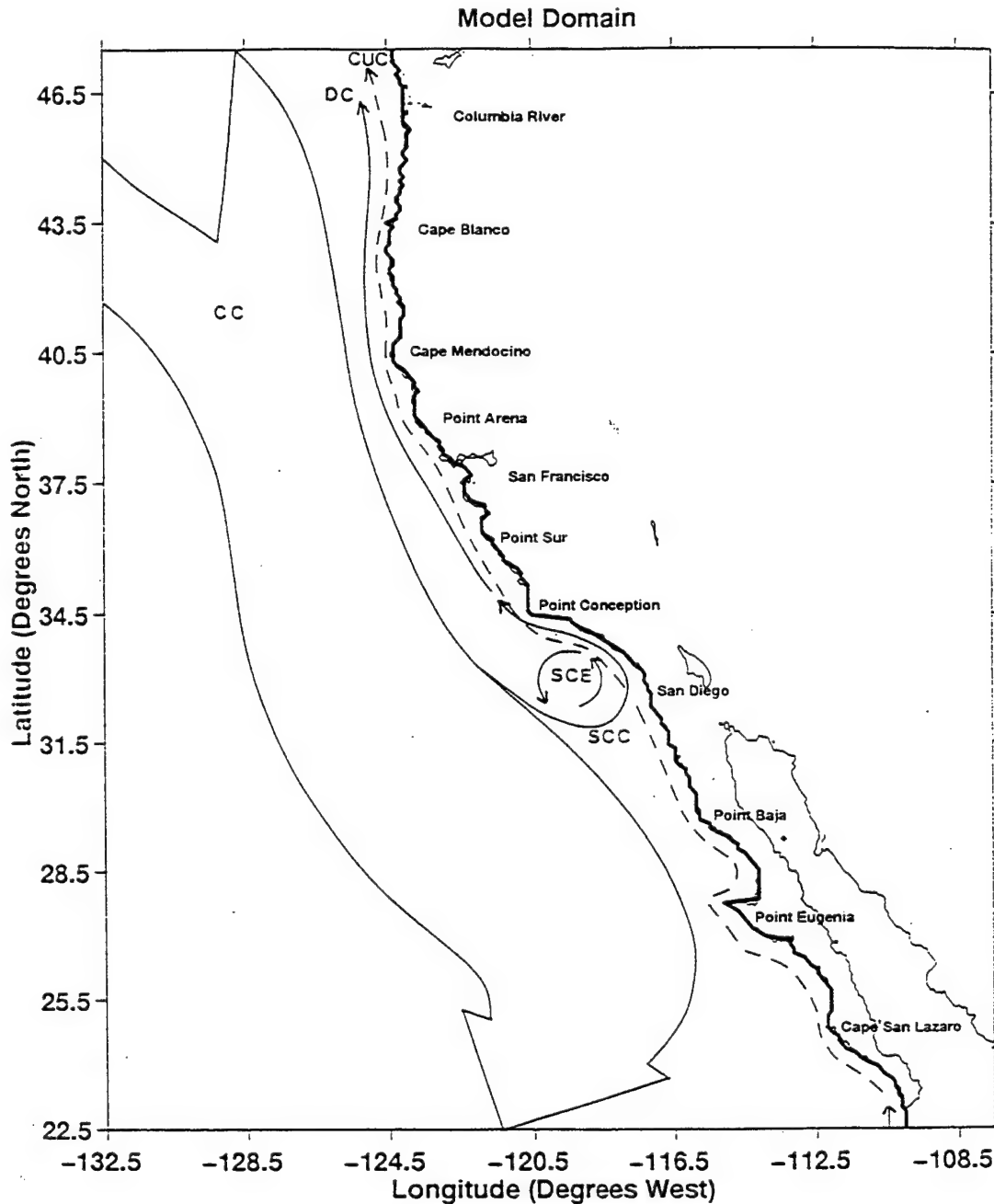
Model Domain

Figure 1. Model domain, coastline, and generalized classical circulation of the California Current System (CCS). The domain is bounded by 22.5° N to 47.5° N, 107.5° W to 132.5° W. The broad, slow surface equatorward California Current (CC) overlies the narrow, poleward California Undercurrent (CUC). Surface poleward flows include the Davidson Current (DC) north of Point Conception, and the Southern California Eddy (SCE) and Southern California Countercurrent (SCC) south of Point Conception.
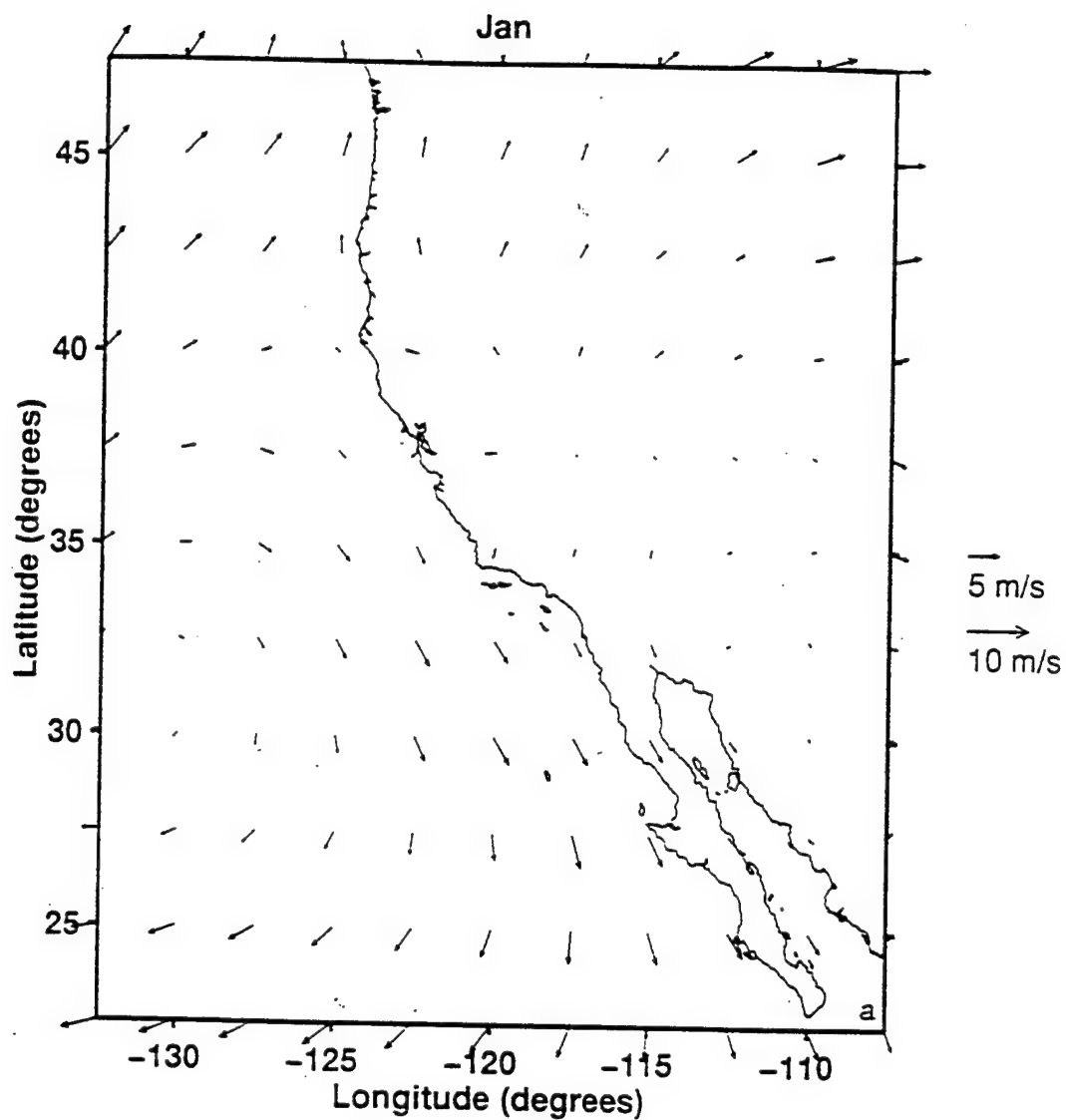
Figure 2. Climatological winds over the California Current System used to force the model. The climatological (1980-1989) ECMWF winds are shown here for (a) January, (b) April, (c) July, and (d) October

34

Apr

Jul

Oct

5 m/s

10 m/s

d

Latitude (degrees)

Longitude (degrees)

37
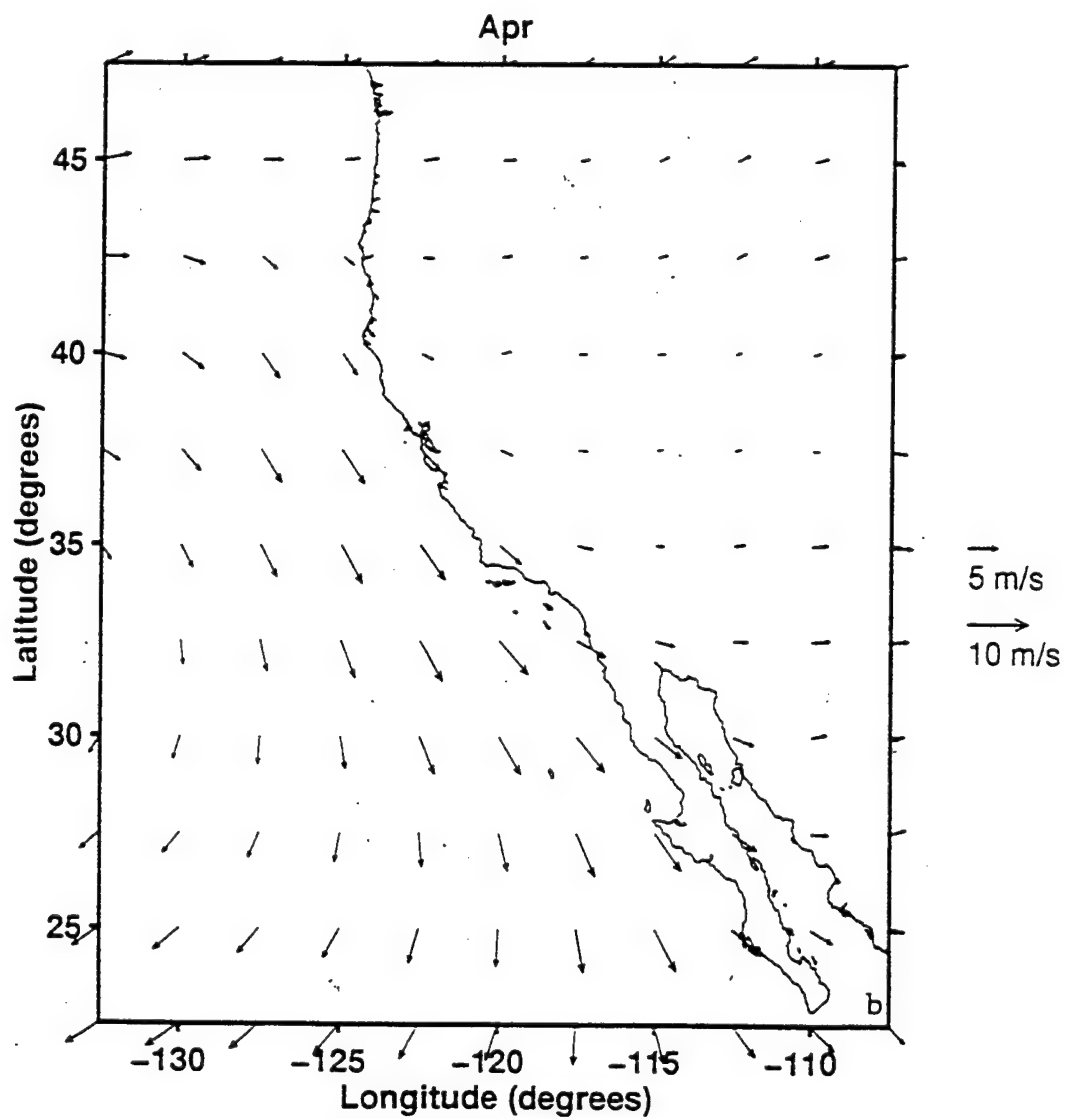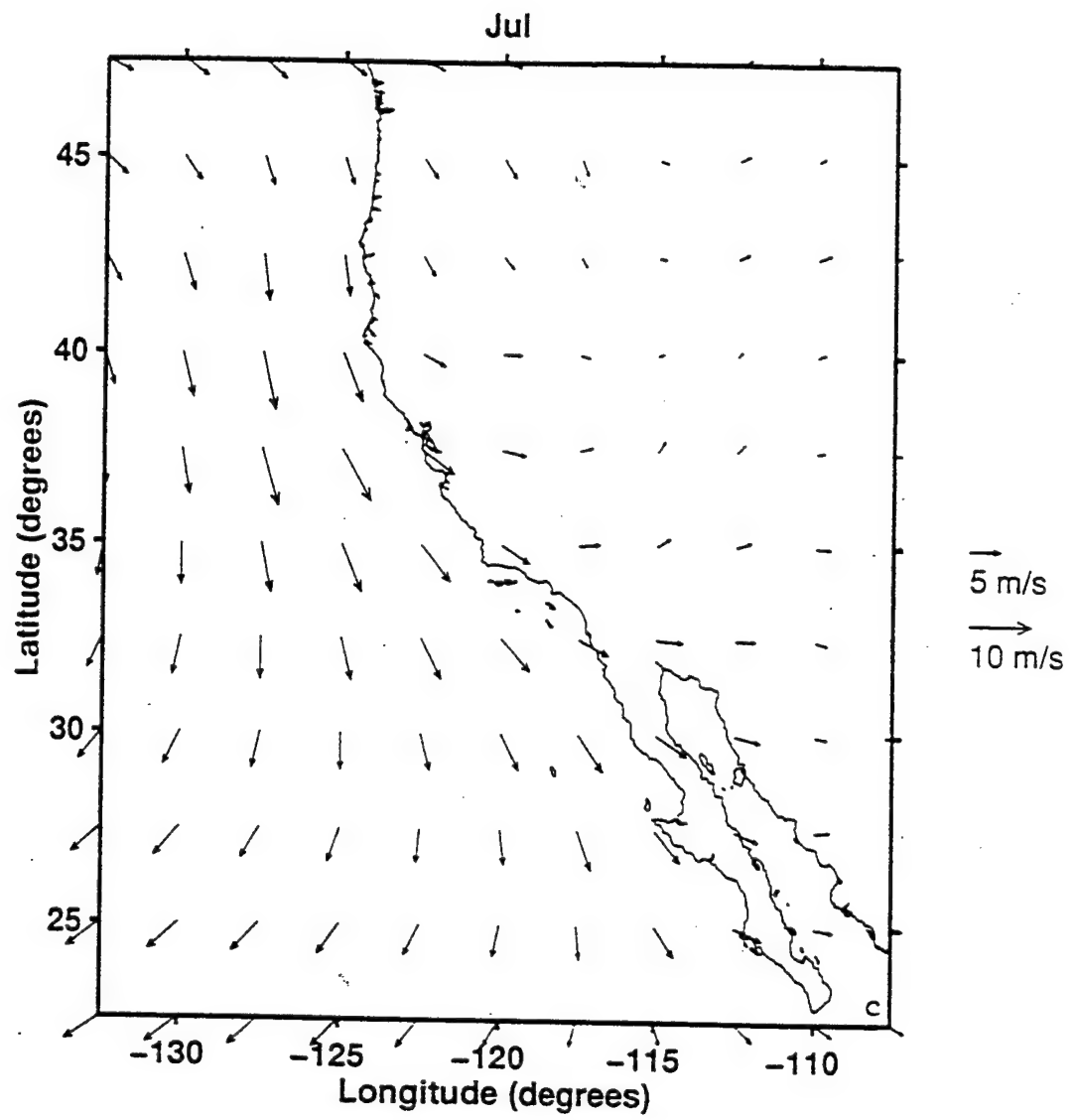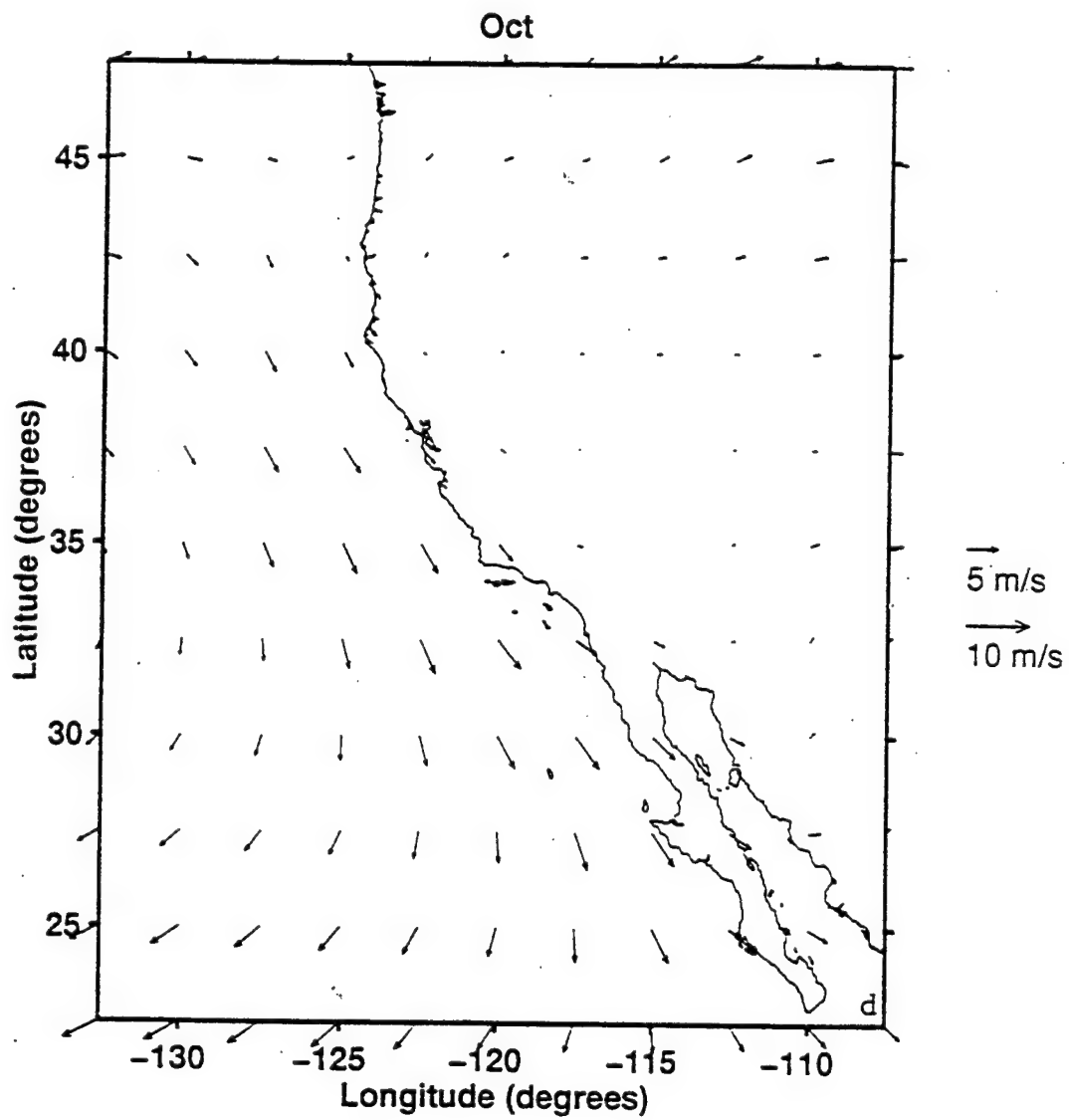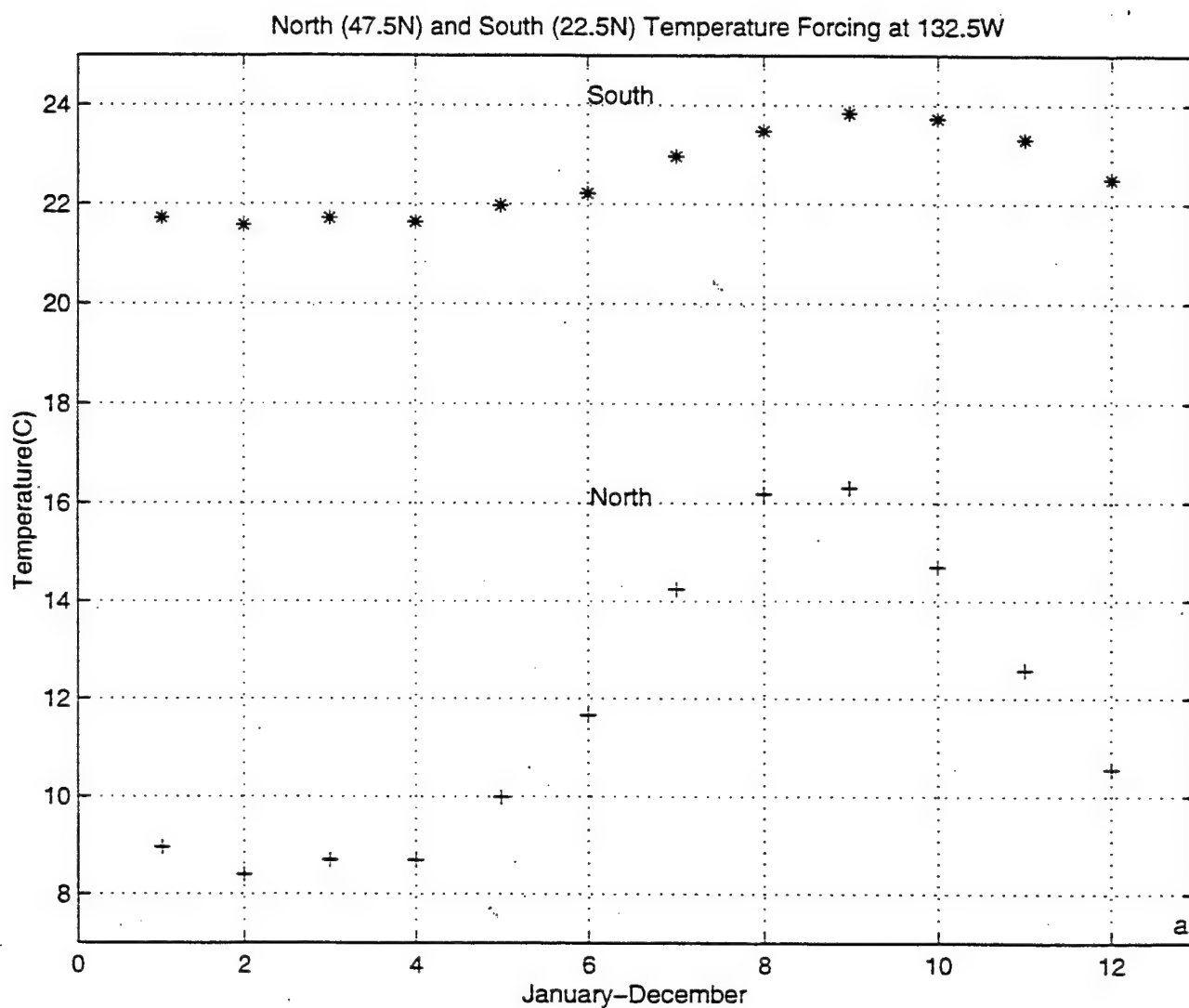
Figure 3. Time series plots of monthly temperature fields used as seasonal forcing in the basic simulation. The '*' symbol represents data at 22.5° N, 132.5° W, while the '+' symbol represents data at 47.5° N, 132.5° W for 13 m depth.

38
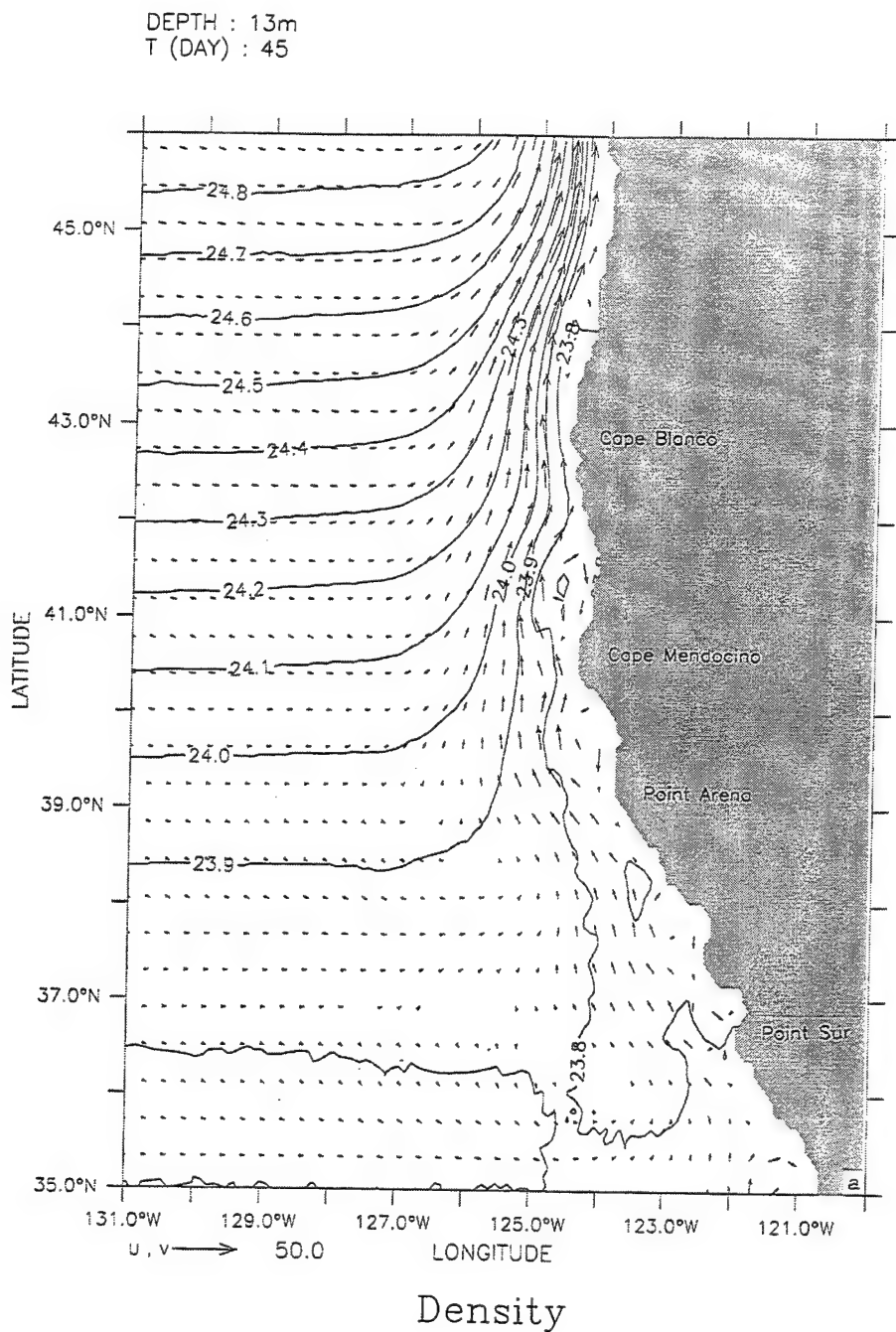
DEPTH : 13m
T (DAY) : 45

Figure 4. Day 45 density contours and velocity vectors at 13 m depth for (a) the northern half and (b) the southern half of the model domain. Contour interval is 0.1 g/cm³; maximum velocity vector is 50 cm/s.

DEPTH : 13m
T (DAY) : 45

Density

DEPTH : 13m
T (DAY) : 195
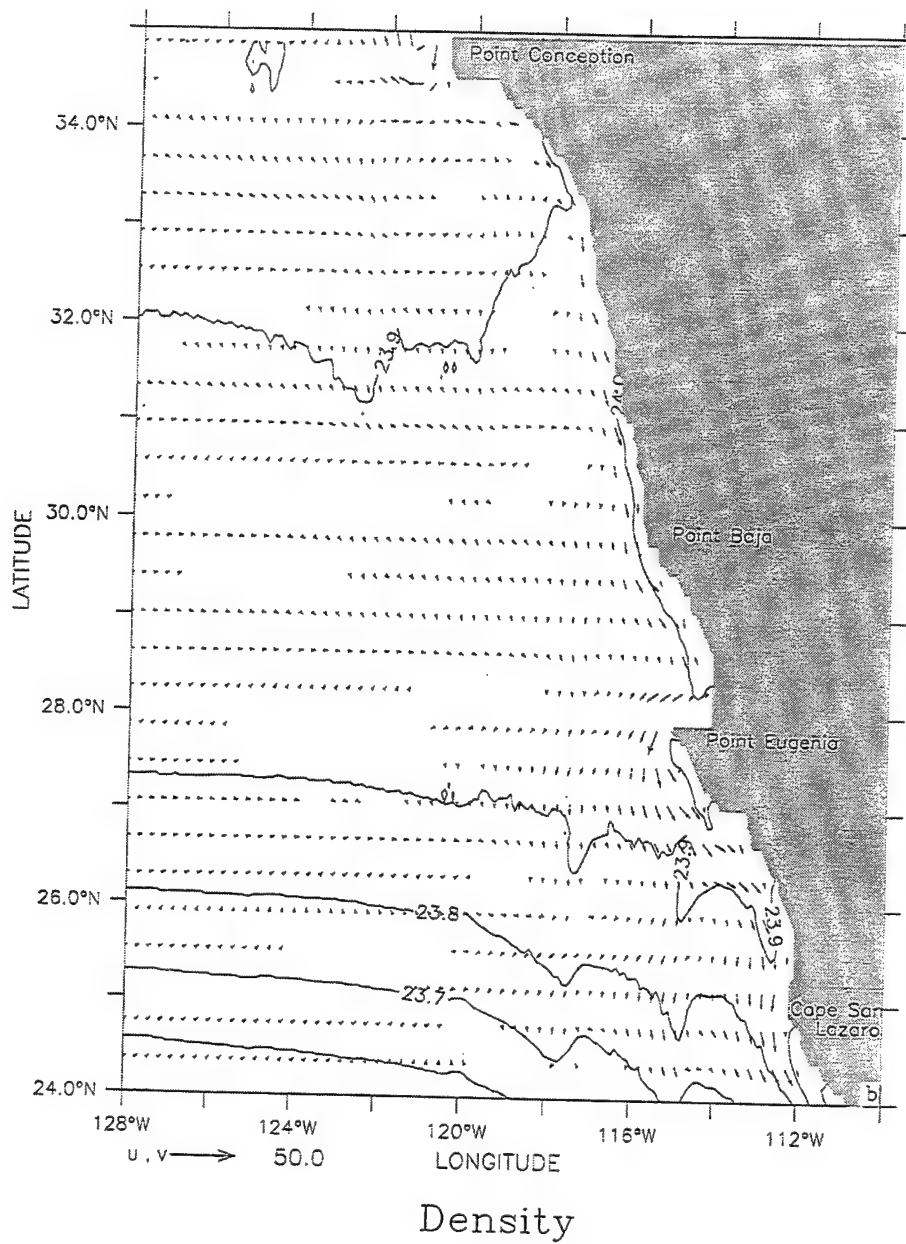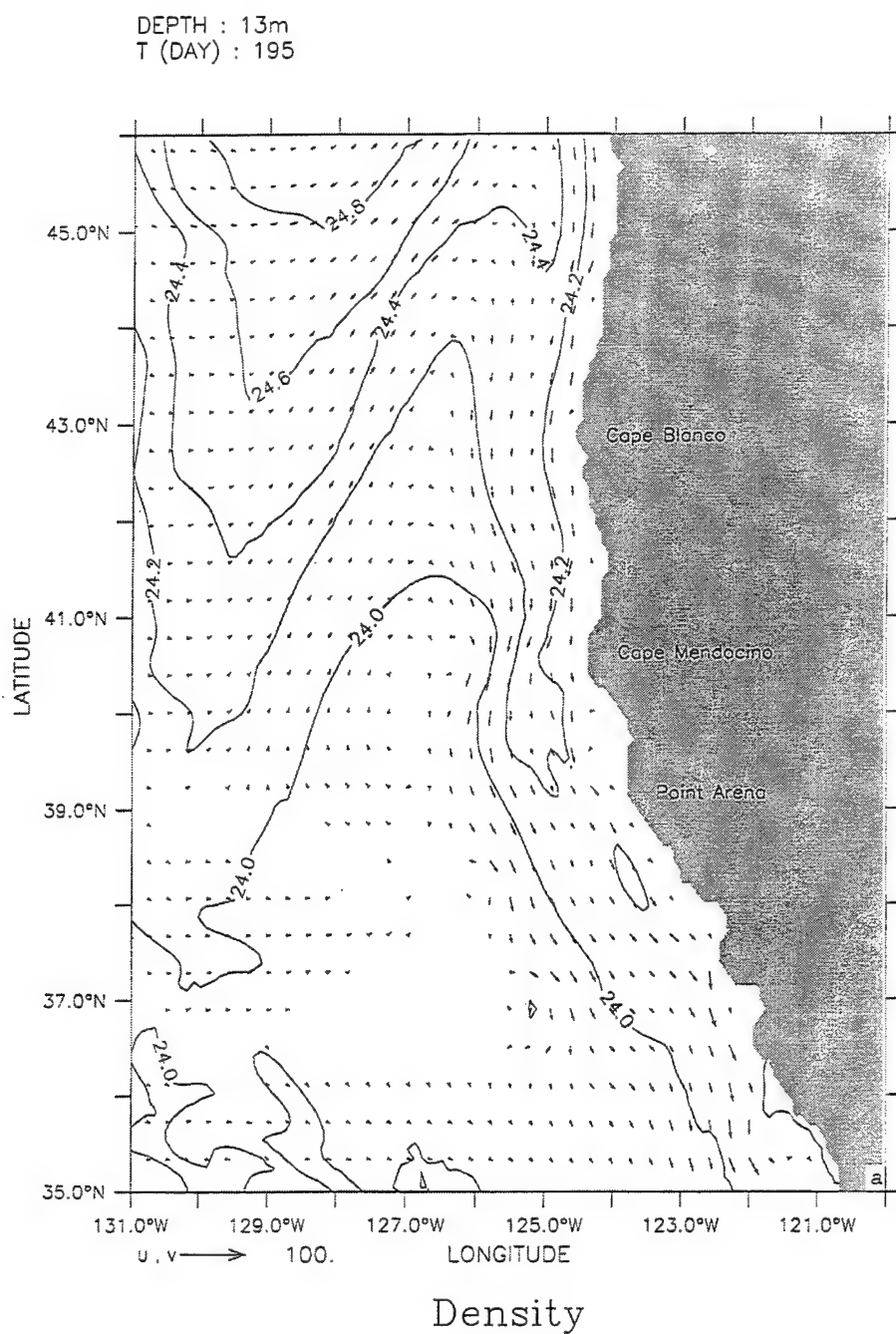
Density

Figure 5.   Day 195 density contours and velocity vectors for the northern (a) and southern (b) portions of the model domain at 13 m depth. Contour interval is 0.2 g/cm^3; maximum velocity vector is 100 cm/s.

DEPTH : 13m
T (DAY) : 195

Density
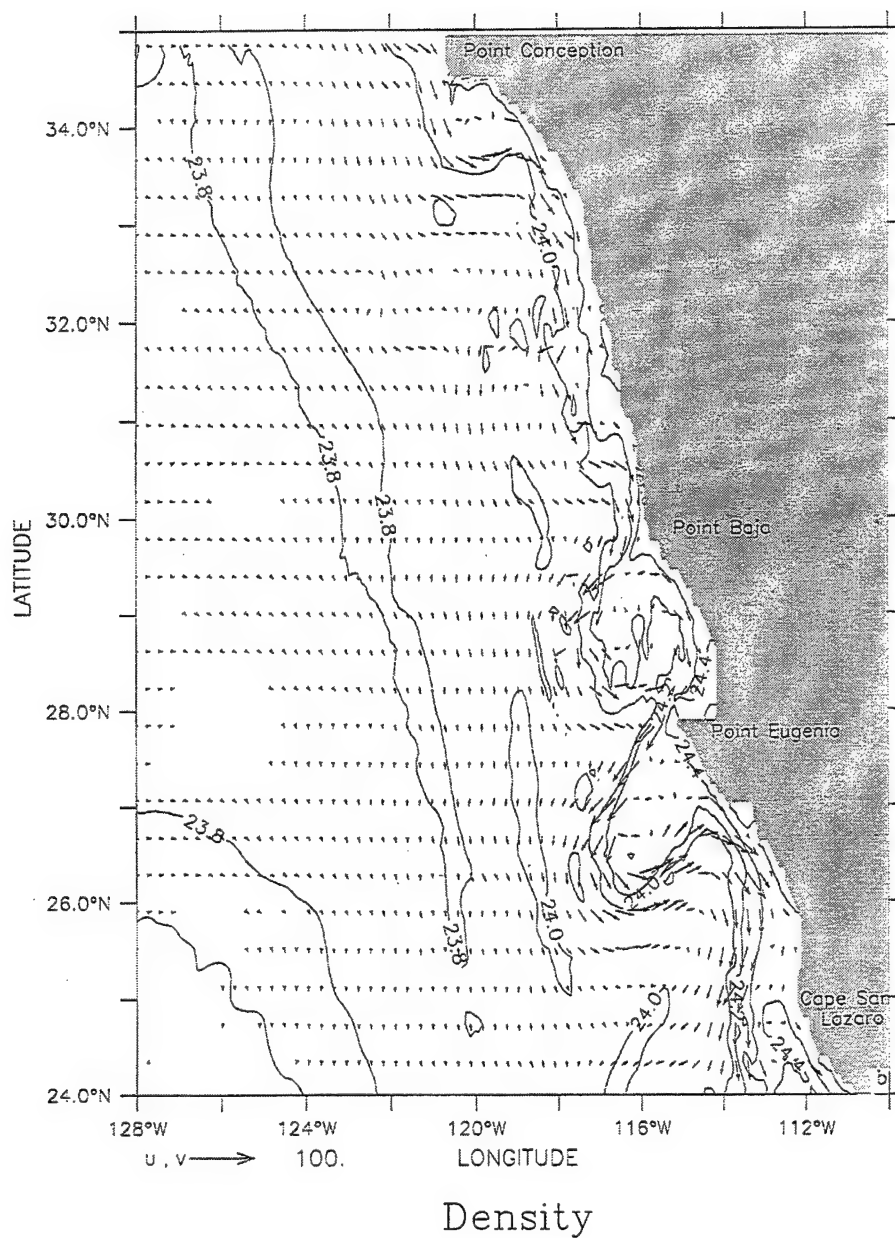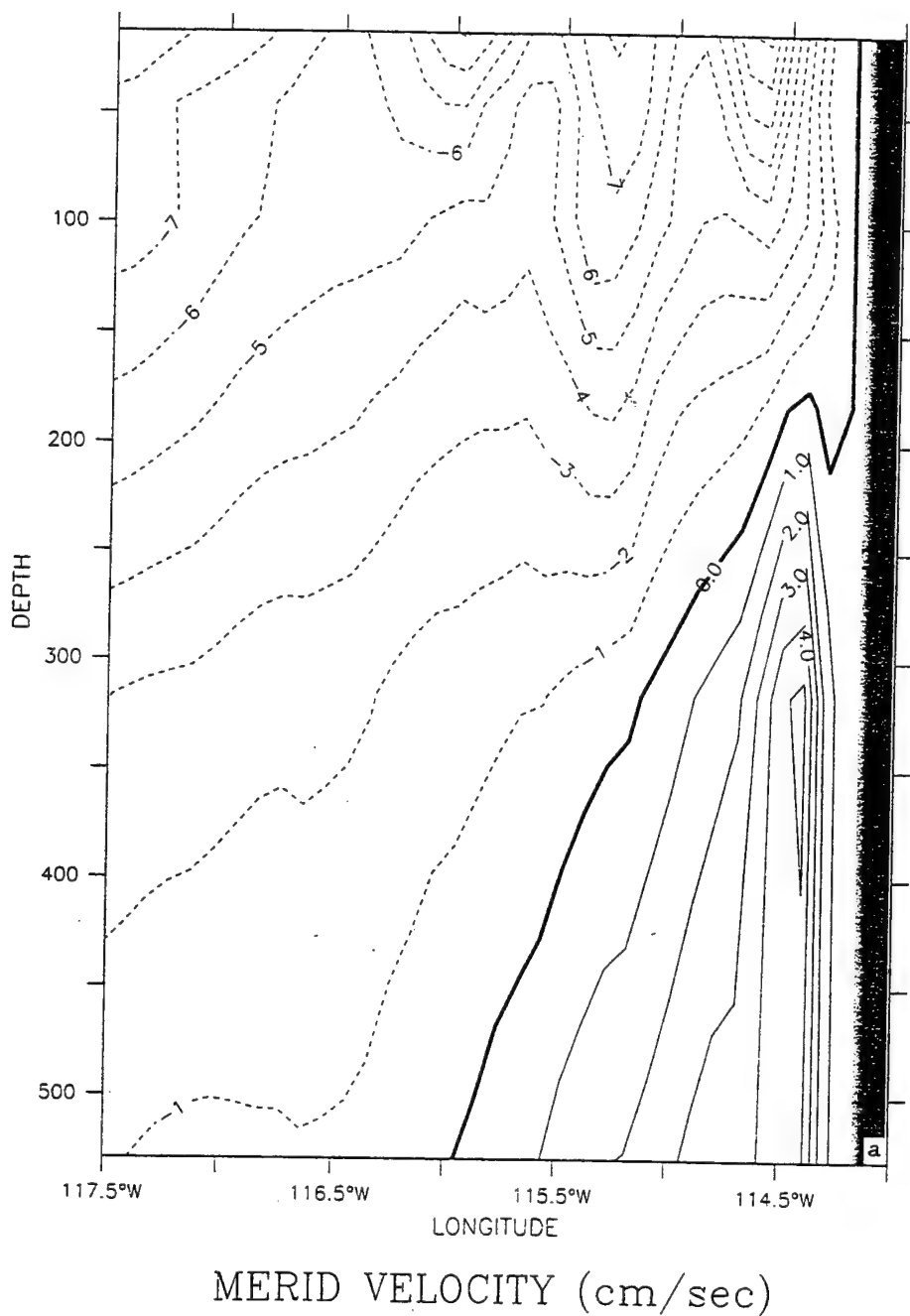
Figure 6. Cross-shore sections of meridional velocity (*v*) at (a) 28.5° N (north of Point Eugenia) on day 105, (b) 41° N on day 195, and (c) 32.5° N on day 195. The contour interval is 1.0 cm/s in (a) and 2.5 cm/s (5 cm/s) for poleward (equatorward) flow in (b) and (c).

43

LATITUDE : 41N
T (DAY) : 195

MERID VELOCITY (cm/sec)

44
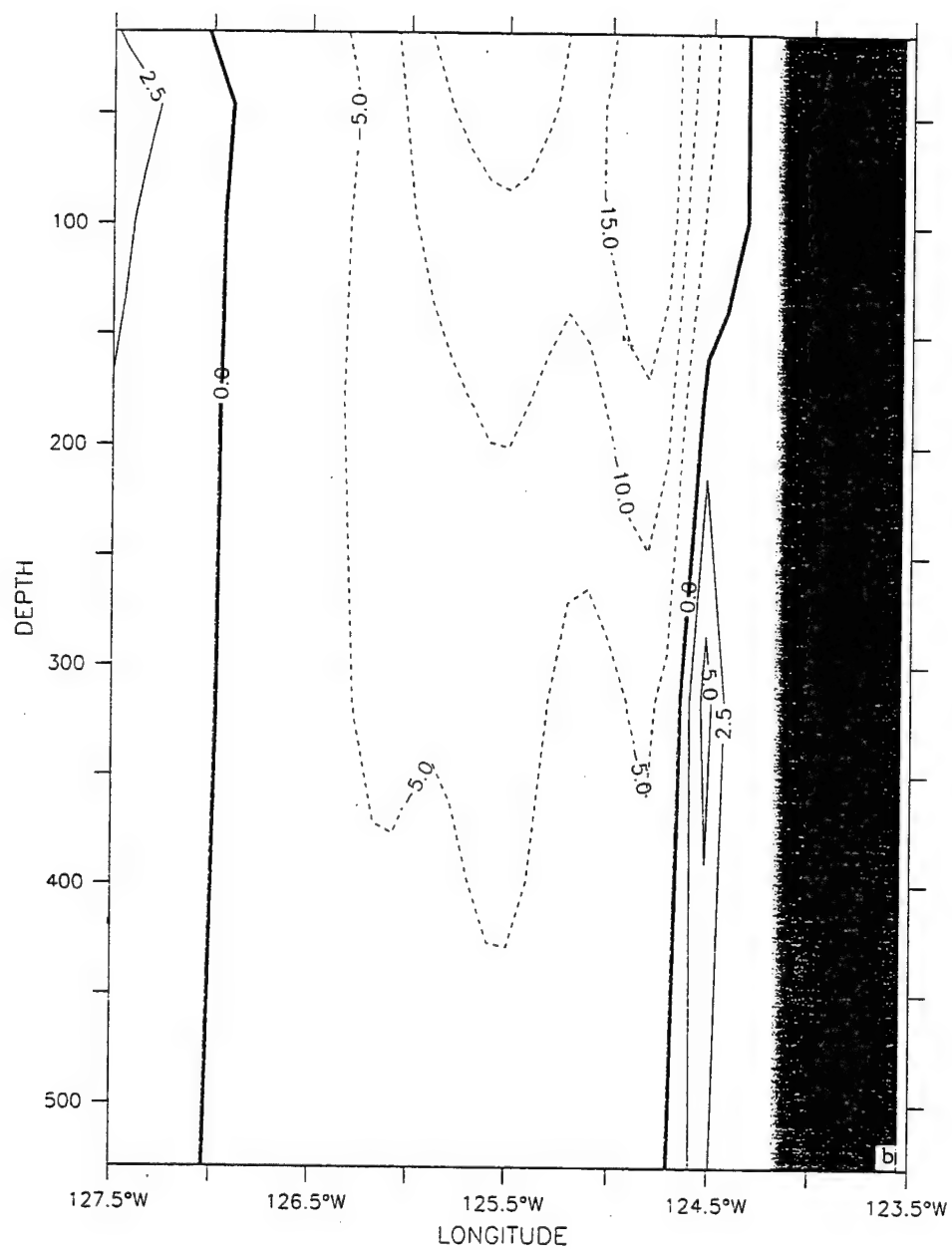
LATITUDE : 32.5N
T (DAY) : 195
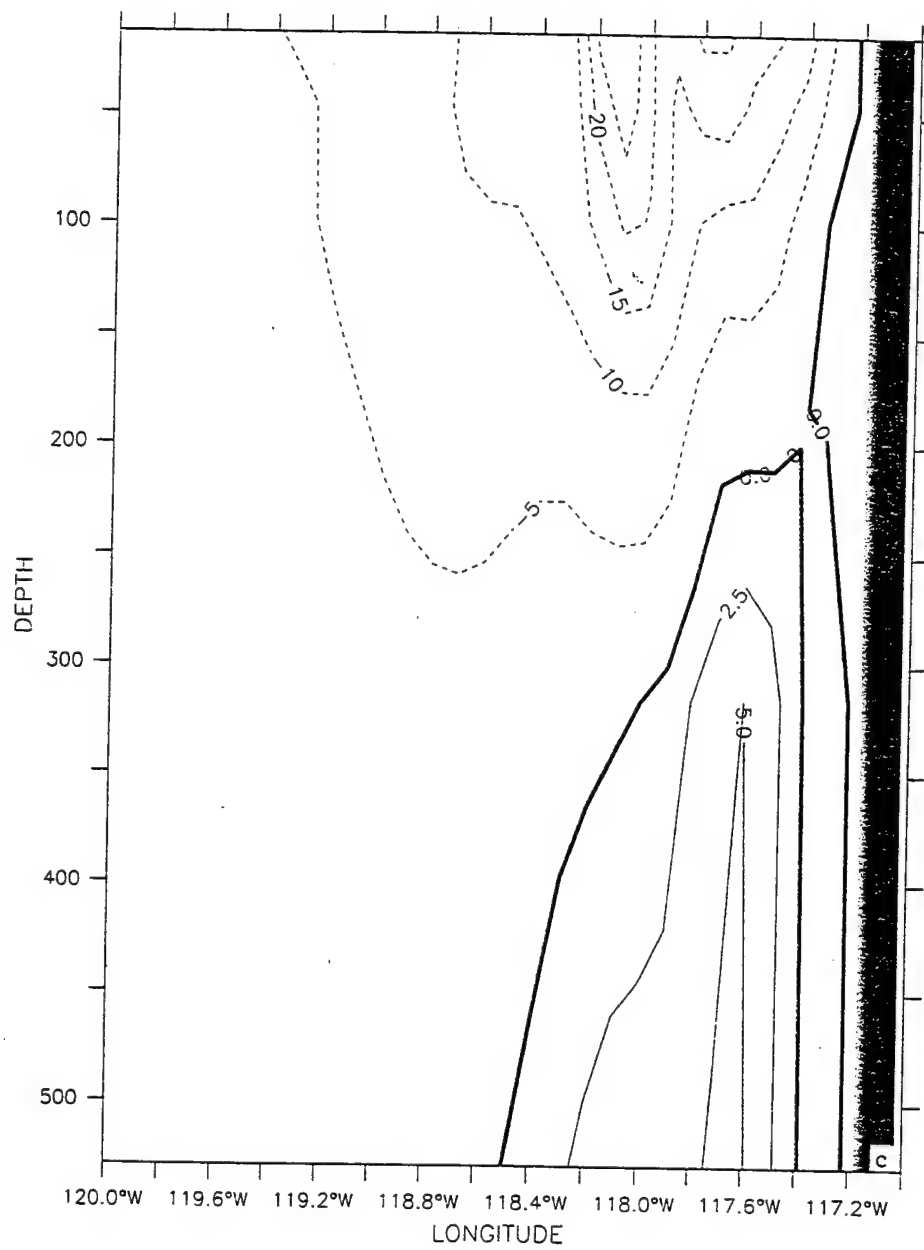
MERID VELOCITY (cm/sec)

MERID VELOCITY (cm/sec)
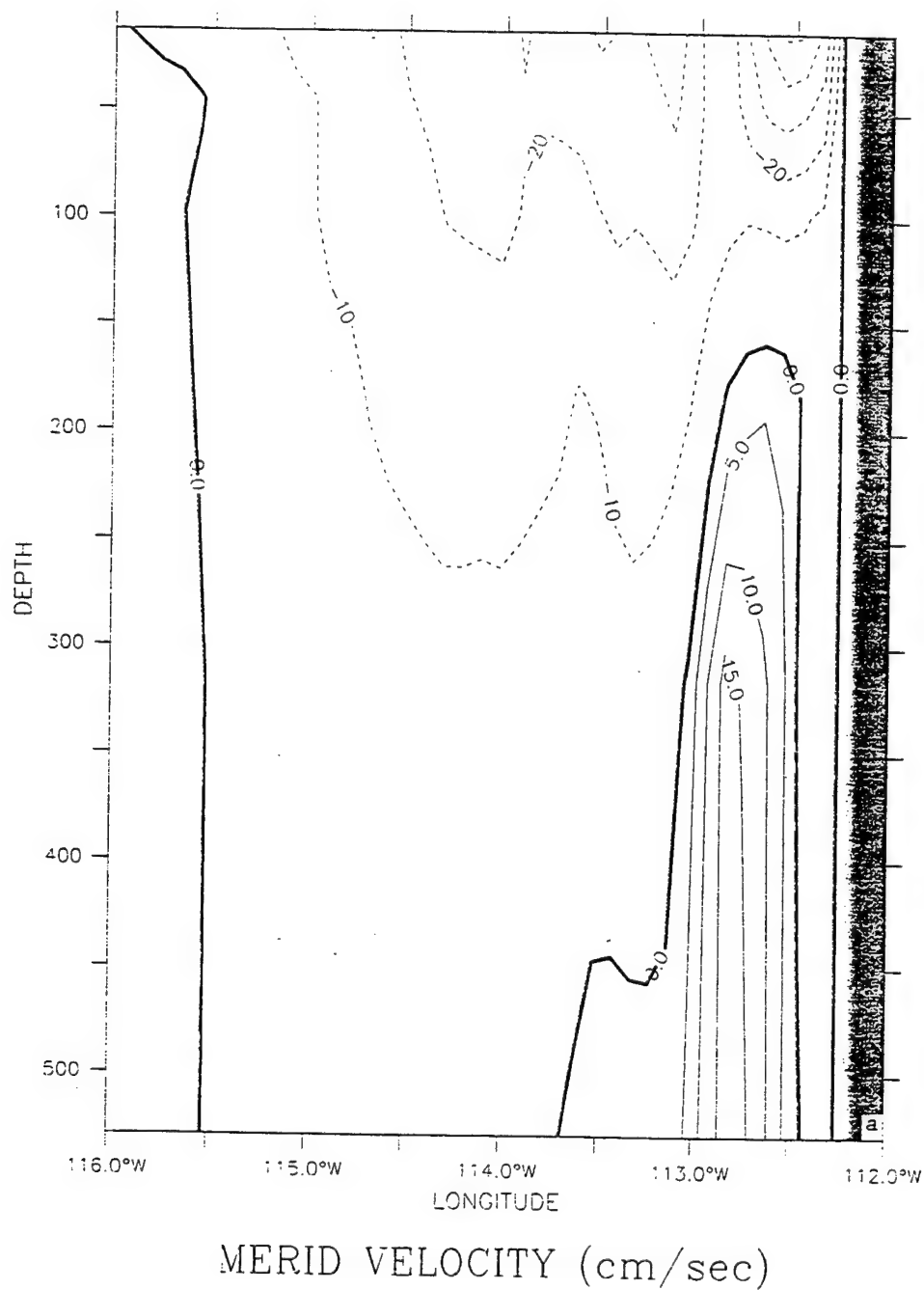
Figure 7. Cross-shore sections of meridional velocity (*v*) at (a) 25° N (off Cape San Lazaro) and (b) 43° N (off Cape Blanco) on day 285. The contour interval is 5 cm/s (10 cm/s) for poleward (equatorward) flow in (a) and 2.5 cm/s (5 cm/s) for poleward (equatorward) flow in (b).

LATITUDE : 43N
T (DAY) : 285

MERID VELOCITY (cm/sec)

47
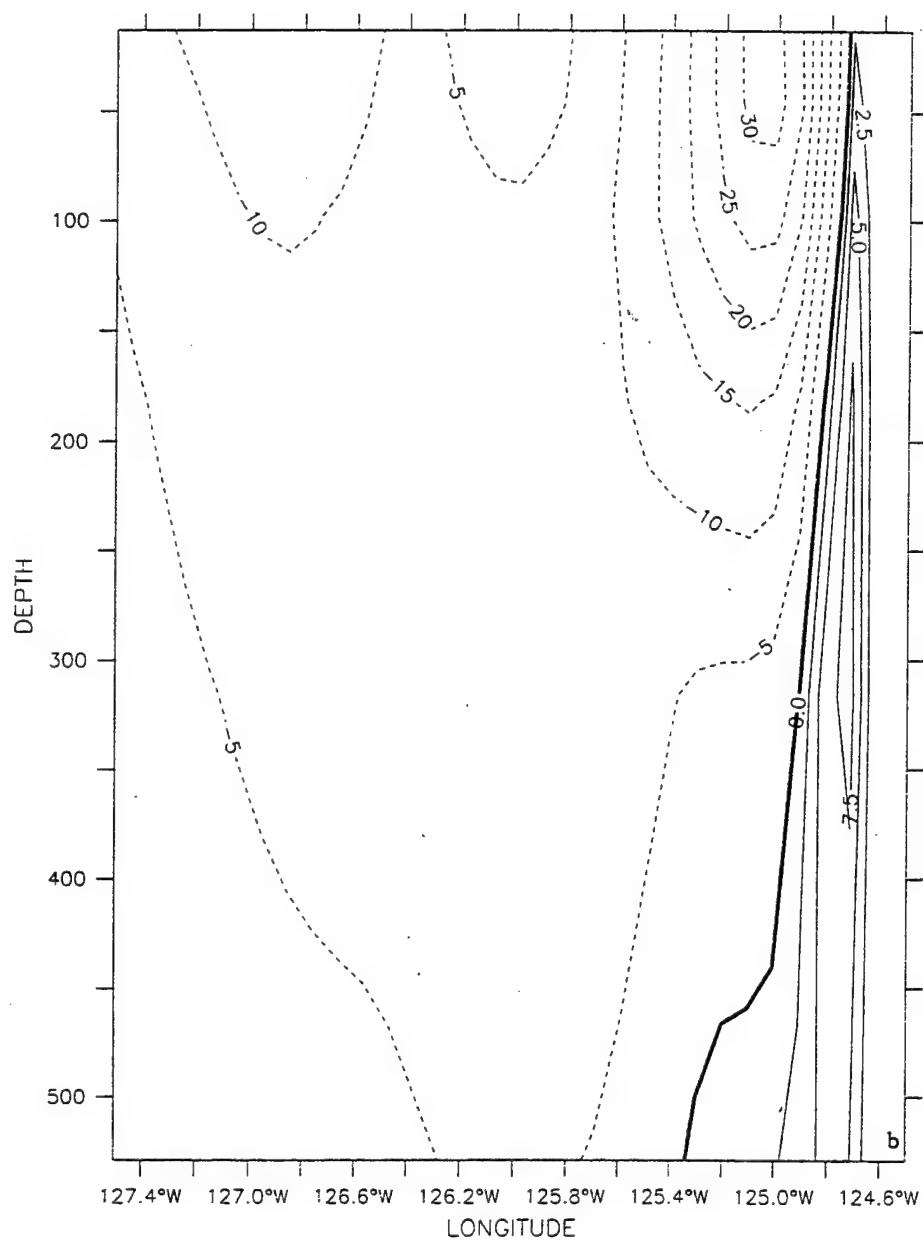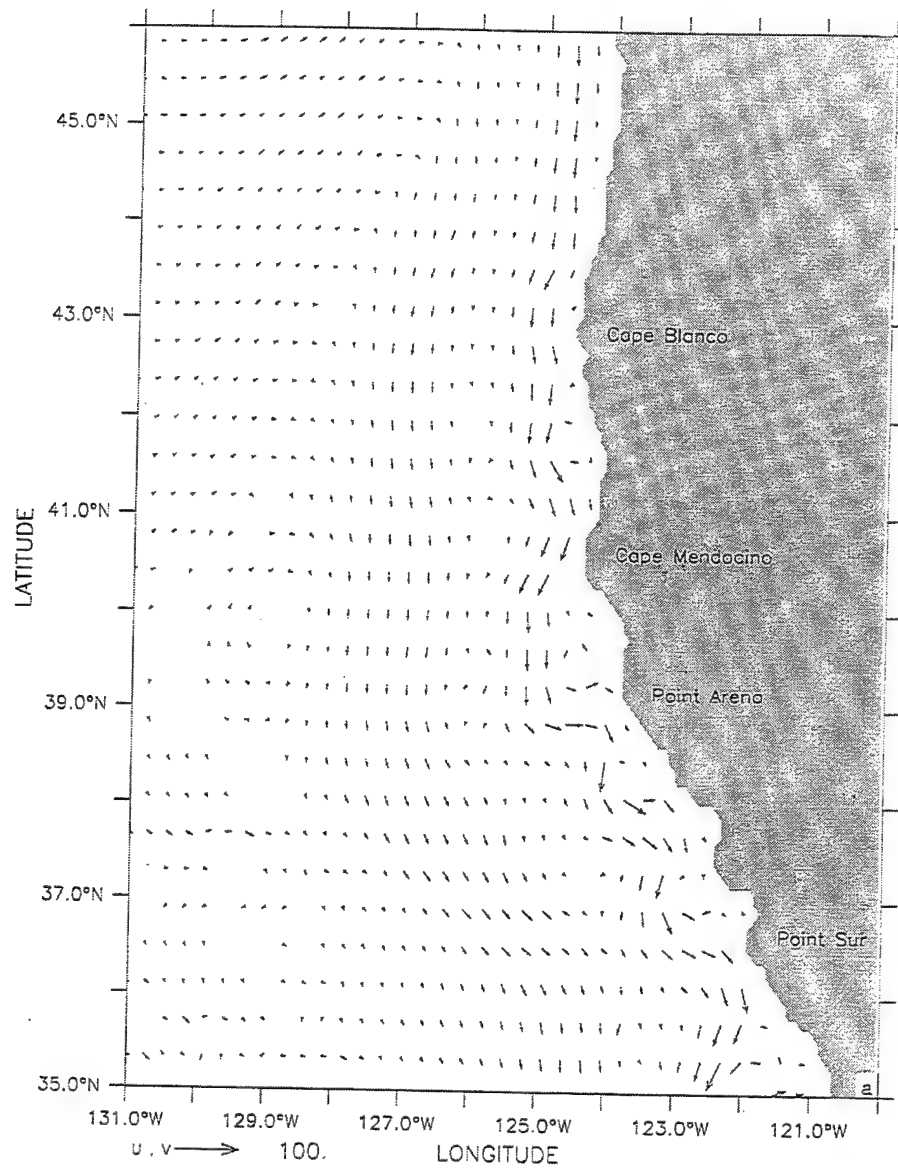
Figure 8. Day 285 velocity vectors for the northern (a) and southern (b) portions of the model domain at 13 m depth. Maximum velocity vector is 100 cm/s.

DEPTH : 13m
T (DAY) : 285

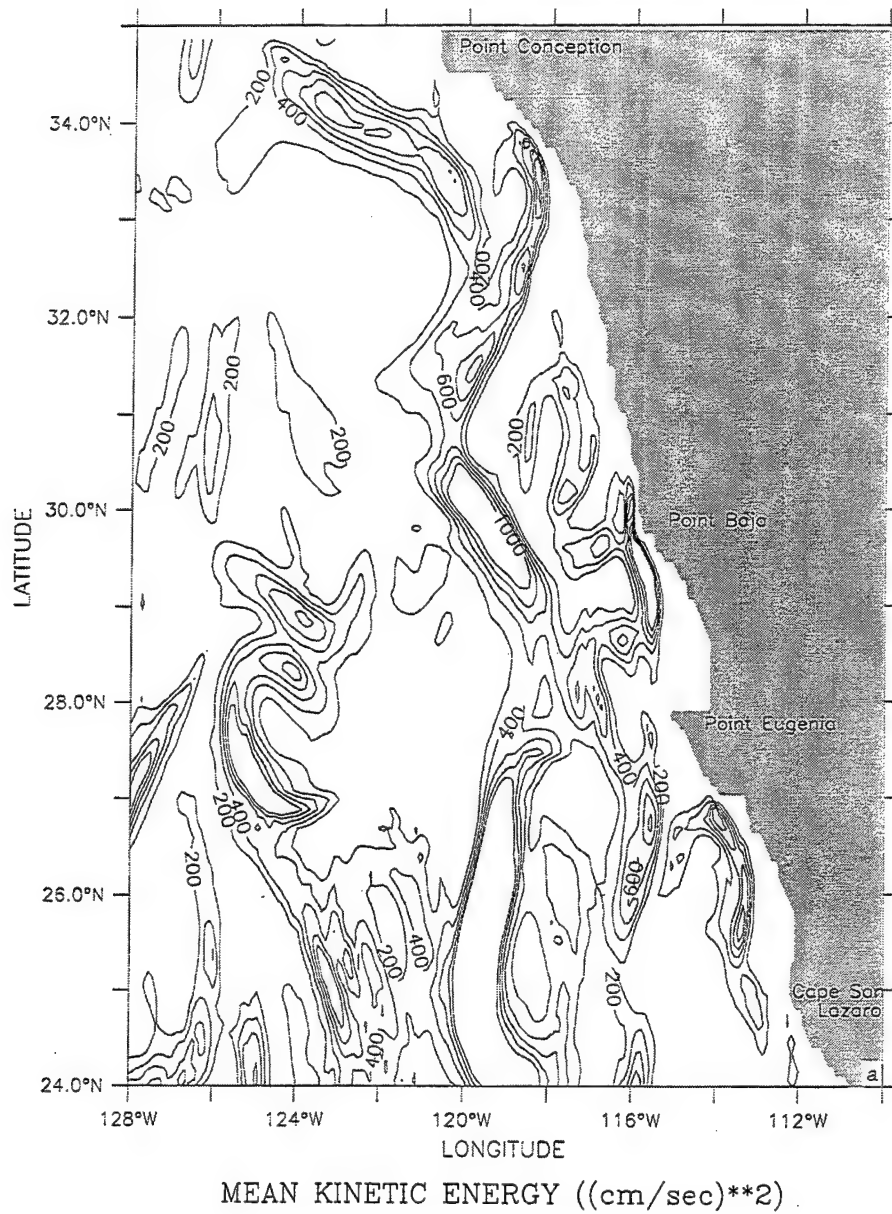DEPTH : 13m

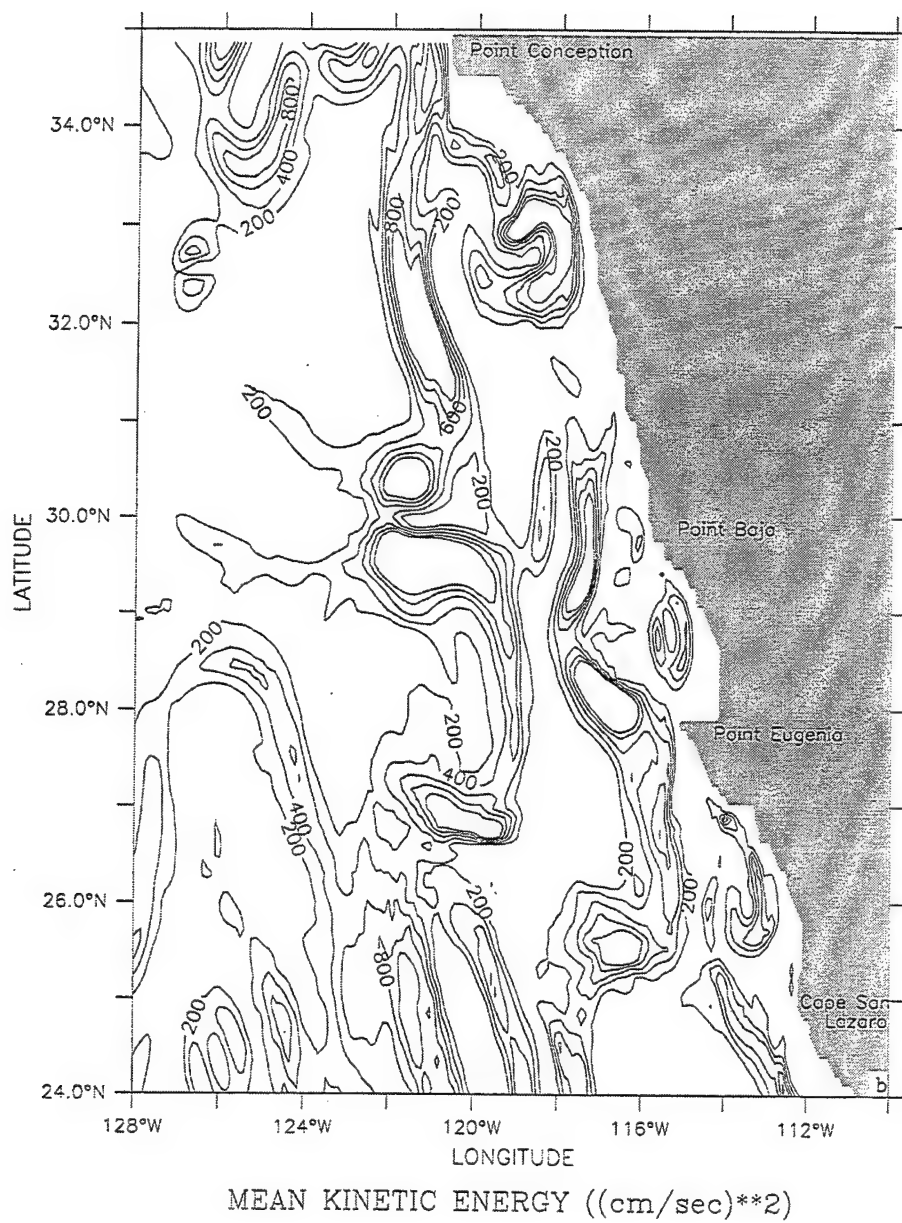LATITUDE
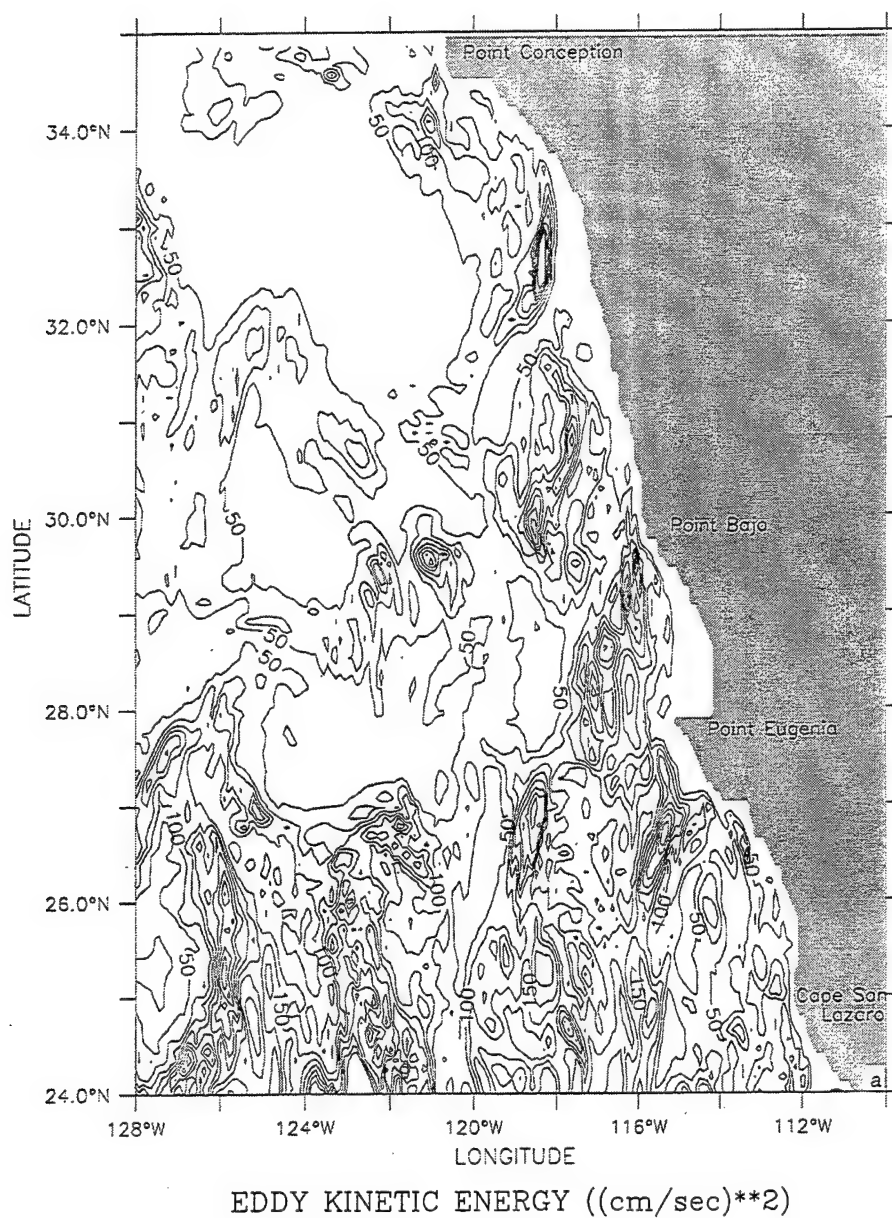
MEAN KINETIC ENERGY ((cm/sec)**2)
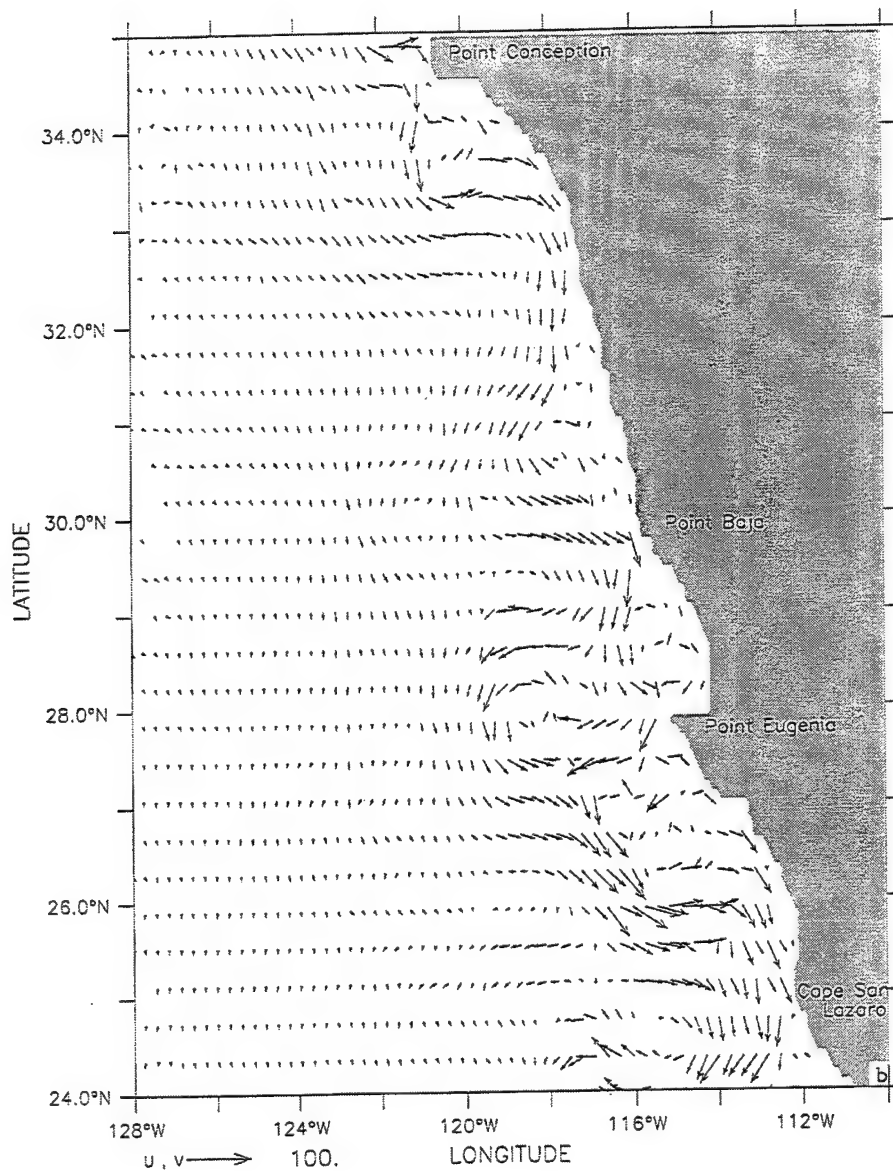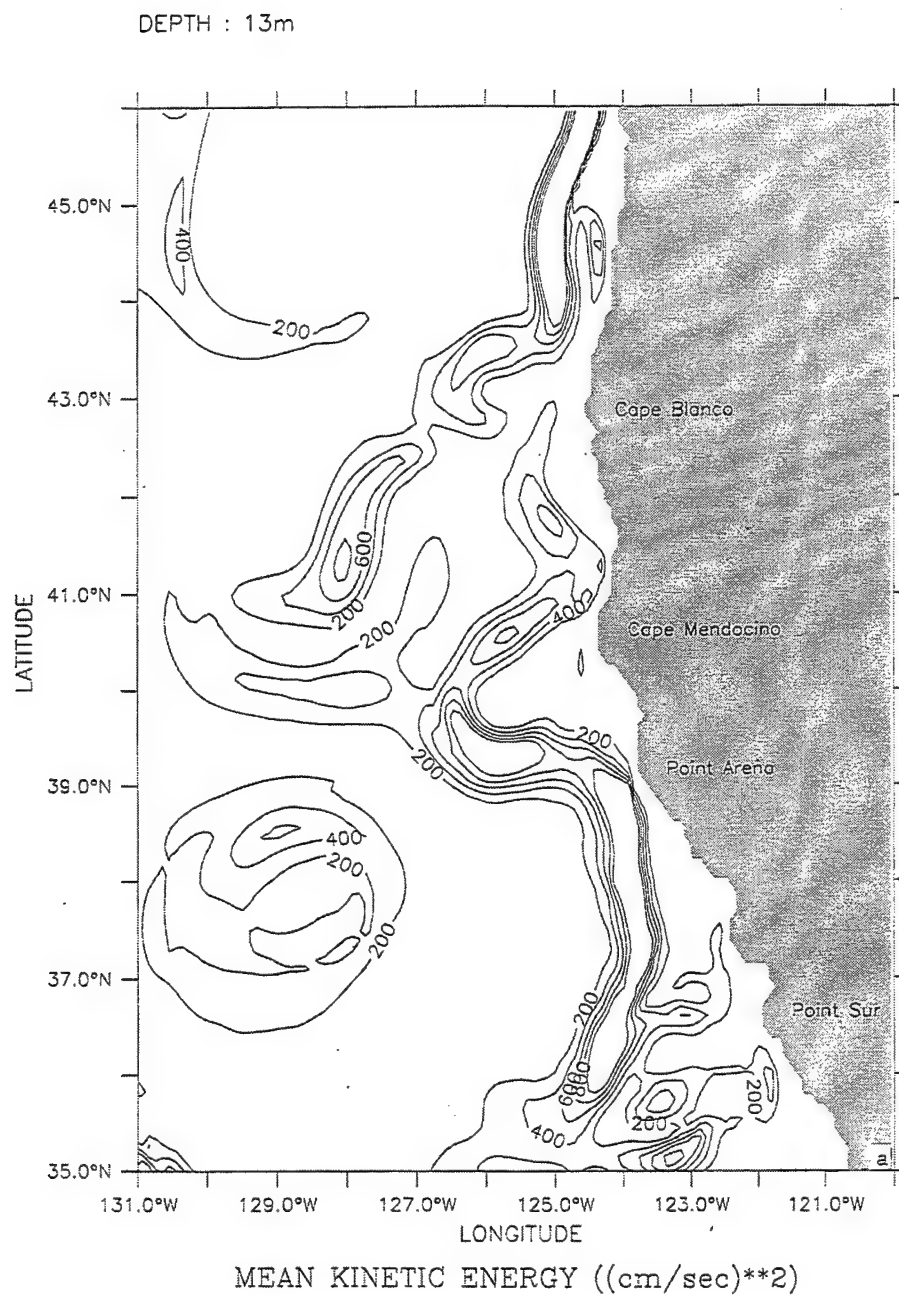
Figure 9. Horizontal maps at 13 m depth of mean kinetic energy (MKE) for the northern portion of the domain in model year 3 averaged for the months of (a) July and (b) October. Contour interval is 200 cm^2/s^2.

DEPTH : 13m

LATITUDE

LONGITUDE

MEAN KINETIC ENERGY ((cm/sec)**2)

51

DEPTH : 13m

EDDY KINETIC ENERGY ((cm/sec)**2)
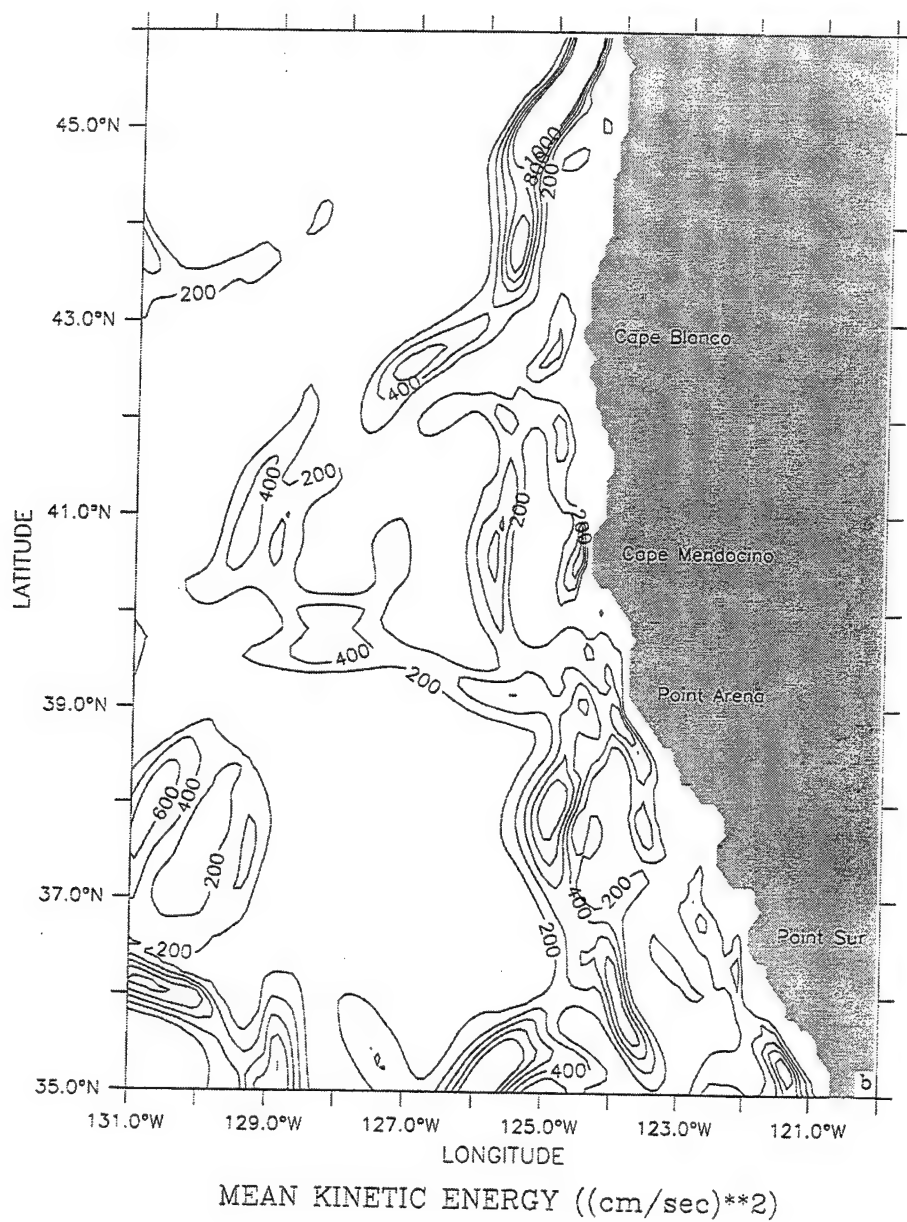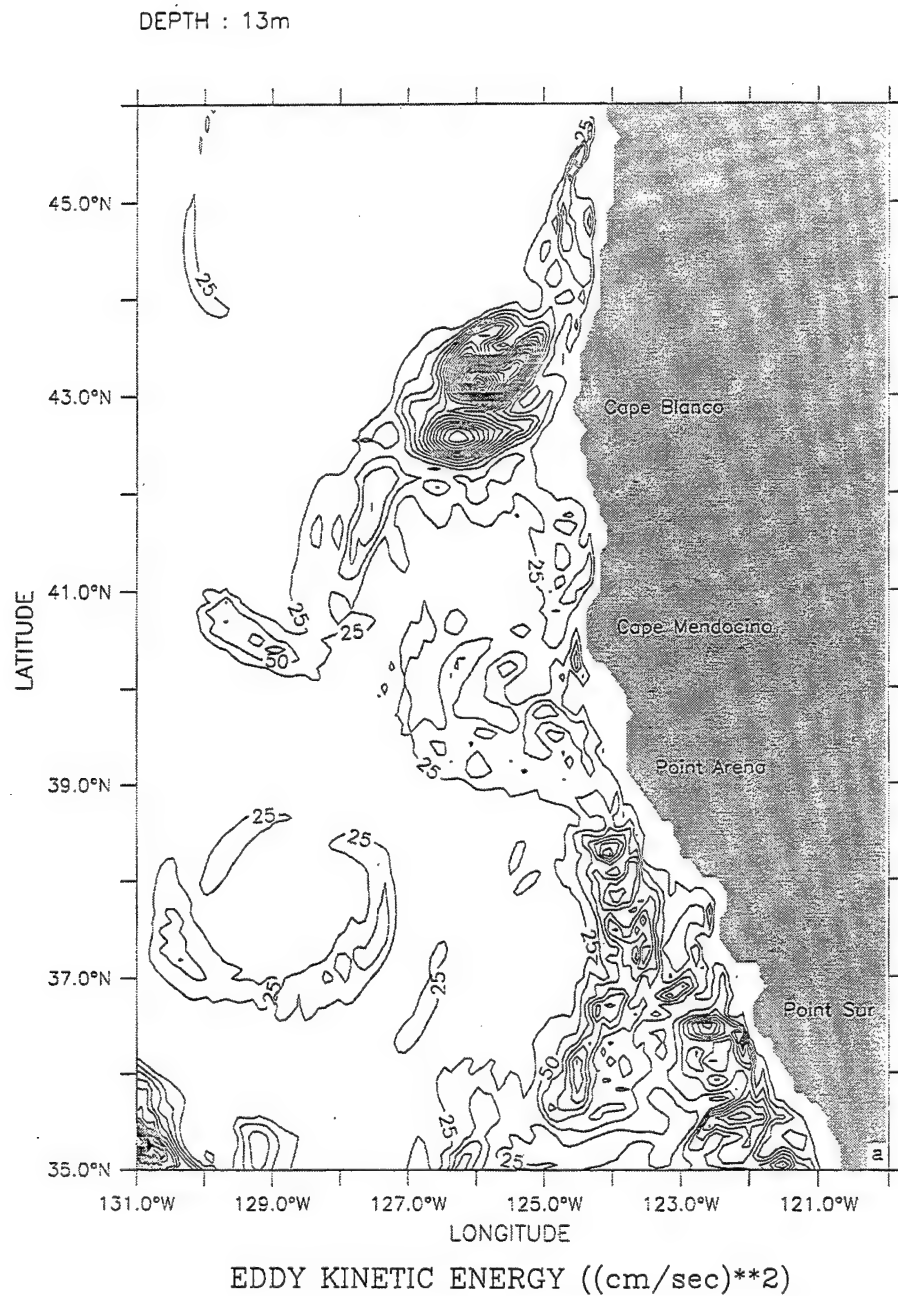
Figure 10. Horizontal maps at 13 m depth of eddy kinetic energy (EKE) for the northern portion of the domain in model year 3, averaged for the months of (a) July, (b) September, and (c) October. Contour interval is 25 cm^2/s^2.

DEPTH : 13m

EDDY KINETIC ENERGY ((cm/sec)**2)(Am=2)

53

DEPTH : 13m

EDDY KINETIC ENERGY ((cm/sec)**2)

54
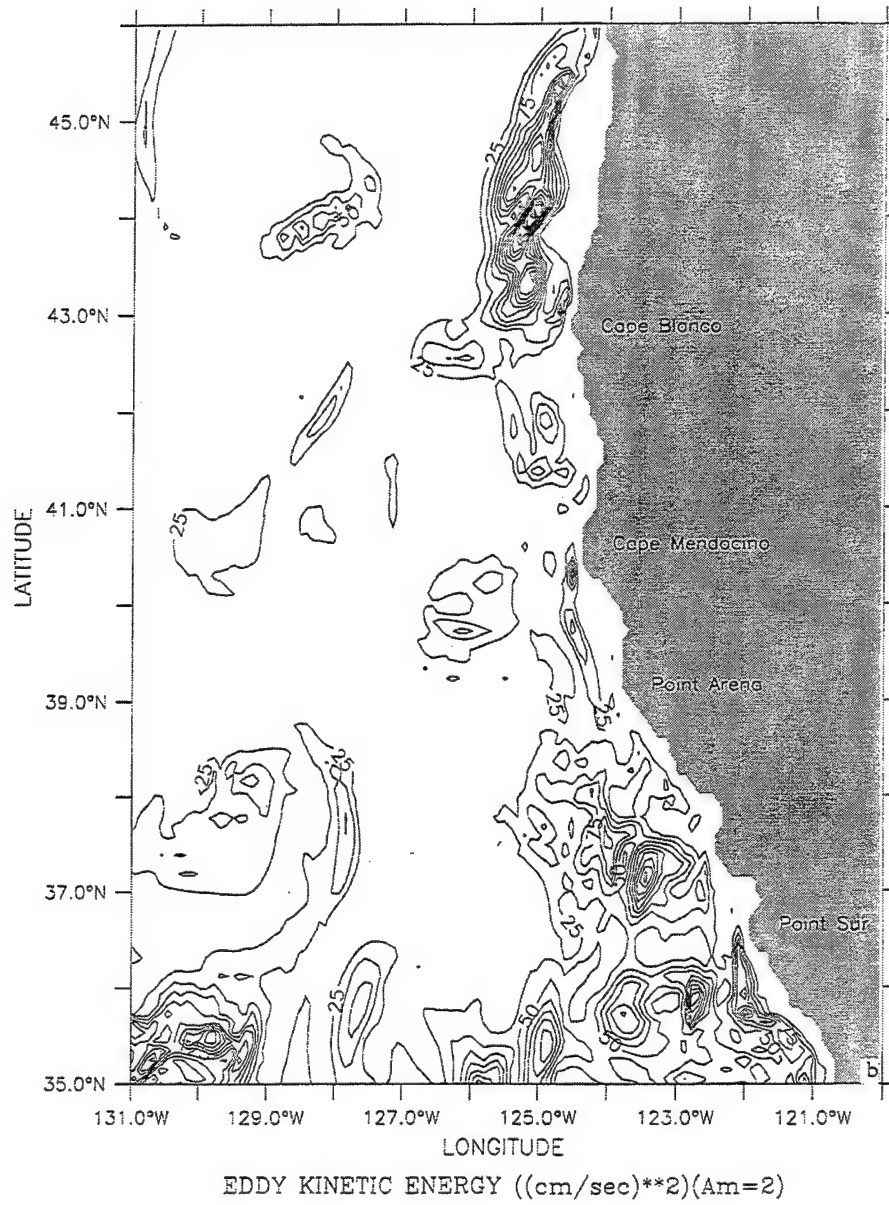
DEPTH : 13m
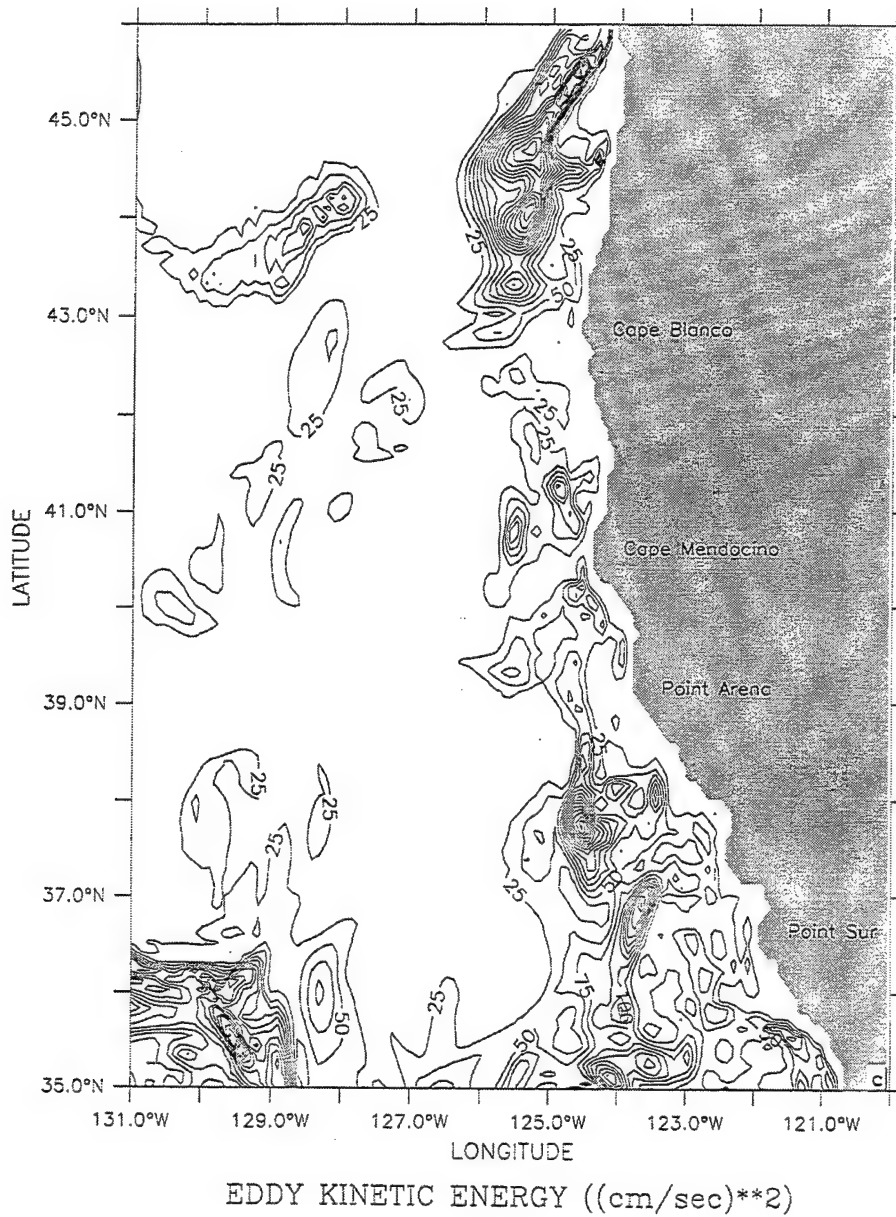
MEAN KINETIC ENERGY ((cm/sec)**2)

Figure 11. Horizontal maps at 13 m depth of mean kinetic energy (MKE) for the southern portion of the domain in model year 3 averaged for the months of (a) July and (b) October. Contour interval is 200 cm^2/s^2.

55

DEPTH : 13m

MEAN KINETIC ENERGY ((cm/sec)**2)

DEPTH : 13m

EDDY KINETIC ENERGY ((cm/sec)**2)

Figure 12. Horizontal maps at 13 m depth of eddy kinetic energy (EKE) for the southern portion of the domain in model year 3, averaged for the months of (a) July and (b) October. Contour interval is 25 cm^2/s^2.

DEPTH : 13m

EDDY KINETIC ENERGY ((cm/sec)**2)
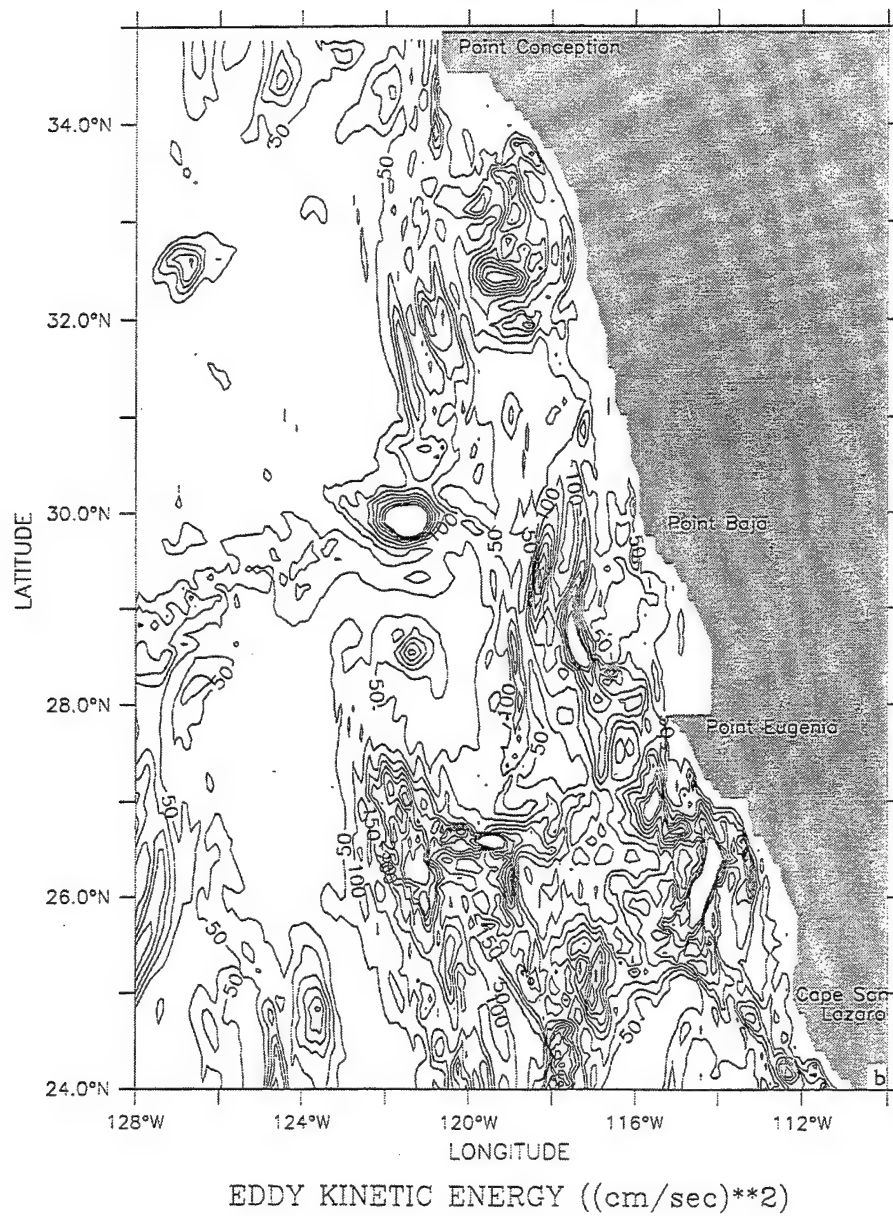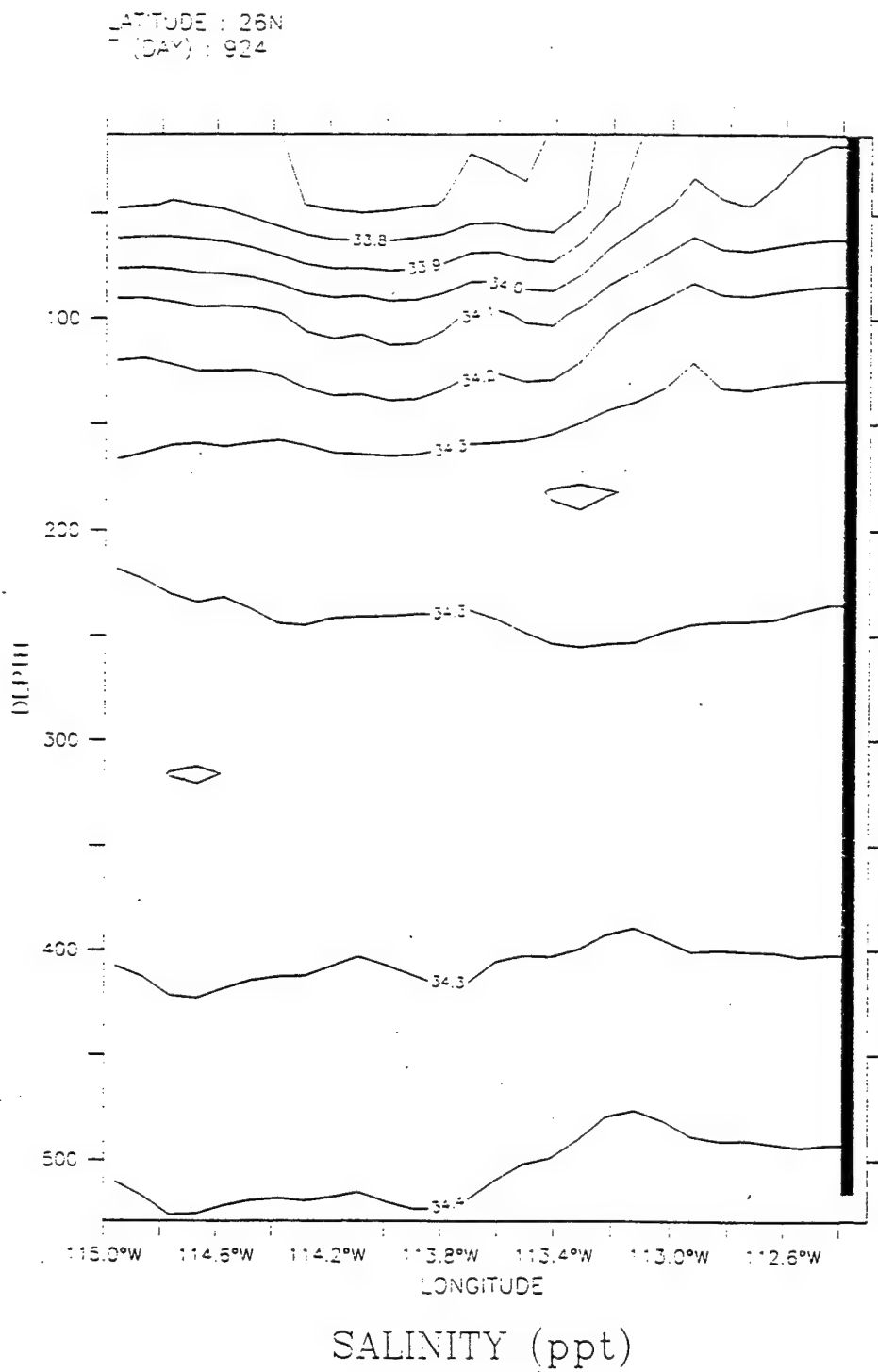
Figure 13. Cross-shore sections of salinity on day 924 (mid-July) of model year 3 at 26°
N (south of Point Eugenia). The contour interval is 0.1 psu.

MEAN MERID VELOCITY (cm/sec)
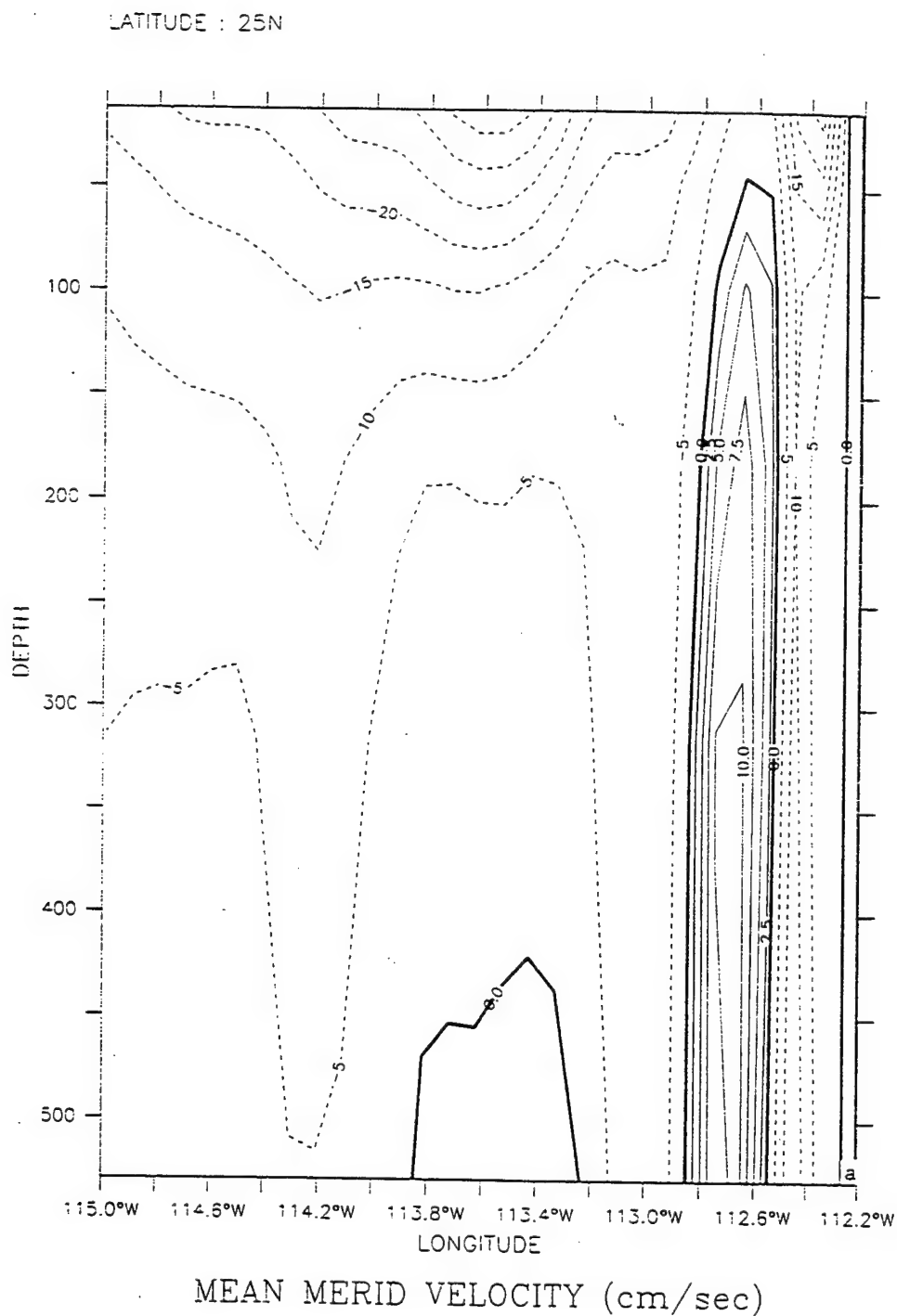
Figure 14. Cross-shore sections of mean v at 25° N (off Cape San Lazaro) for (a) January, (b) April, (c) July, and (d) October of model year 3. The contour interval is 2.5 cm/s (5 cm/s) for poleward (equatorward) flow in (a, b, d) and 5 cm/s for both in (c).
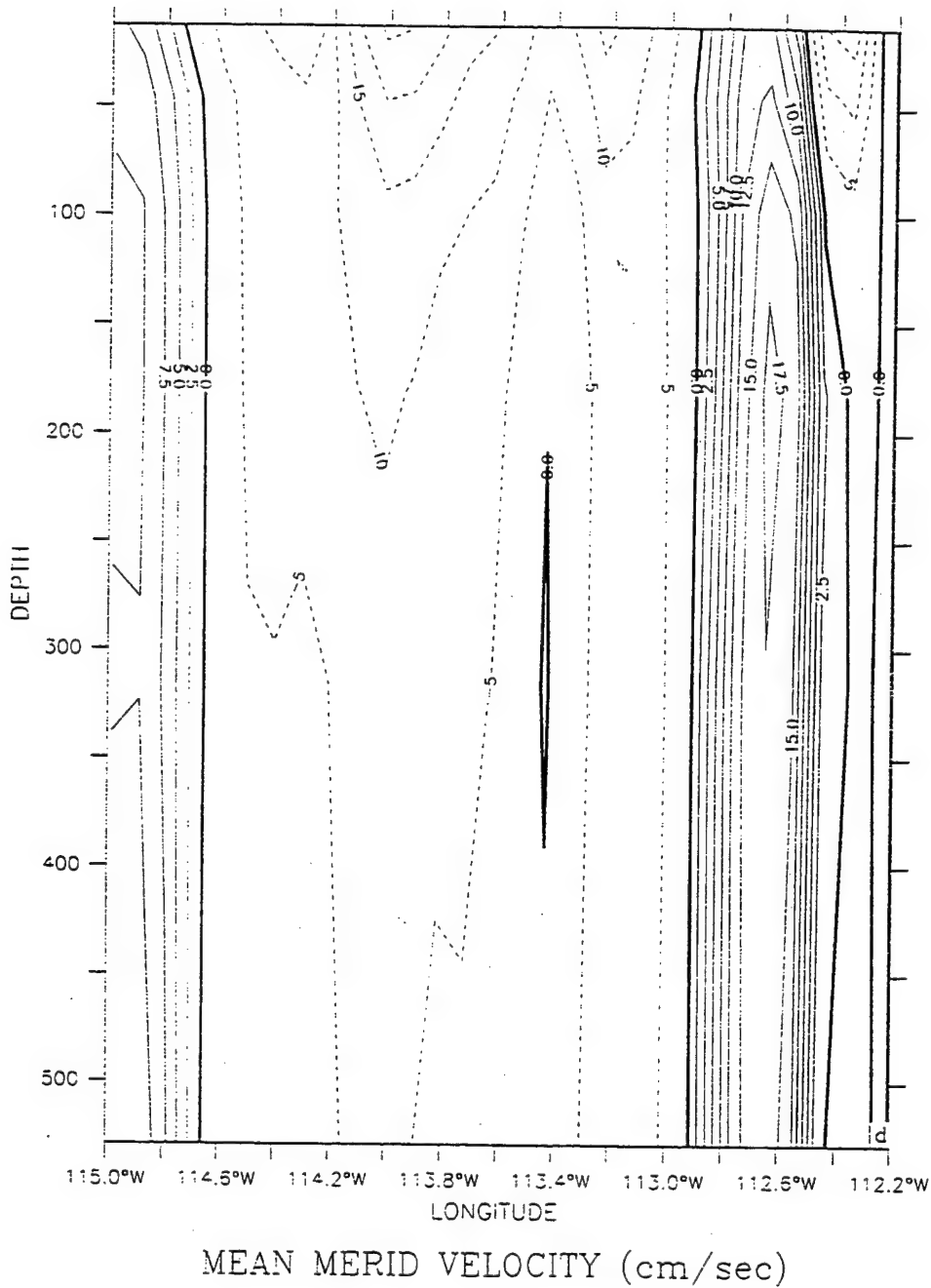
LATITUDE : 25N

MEAN MERID VELOCITY (cm/sec)

61

MEAN MERID VELOCITY (cm/sec)

62
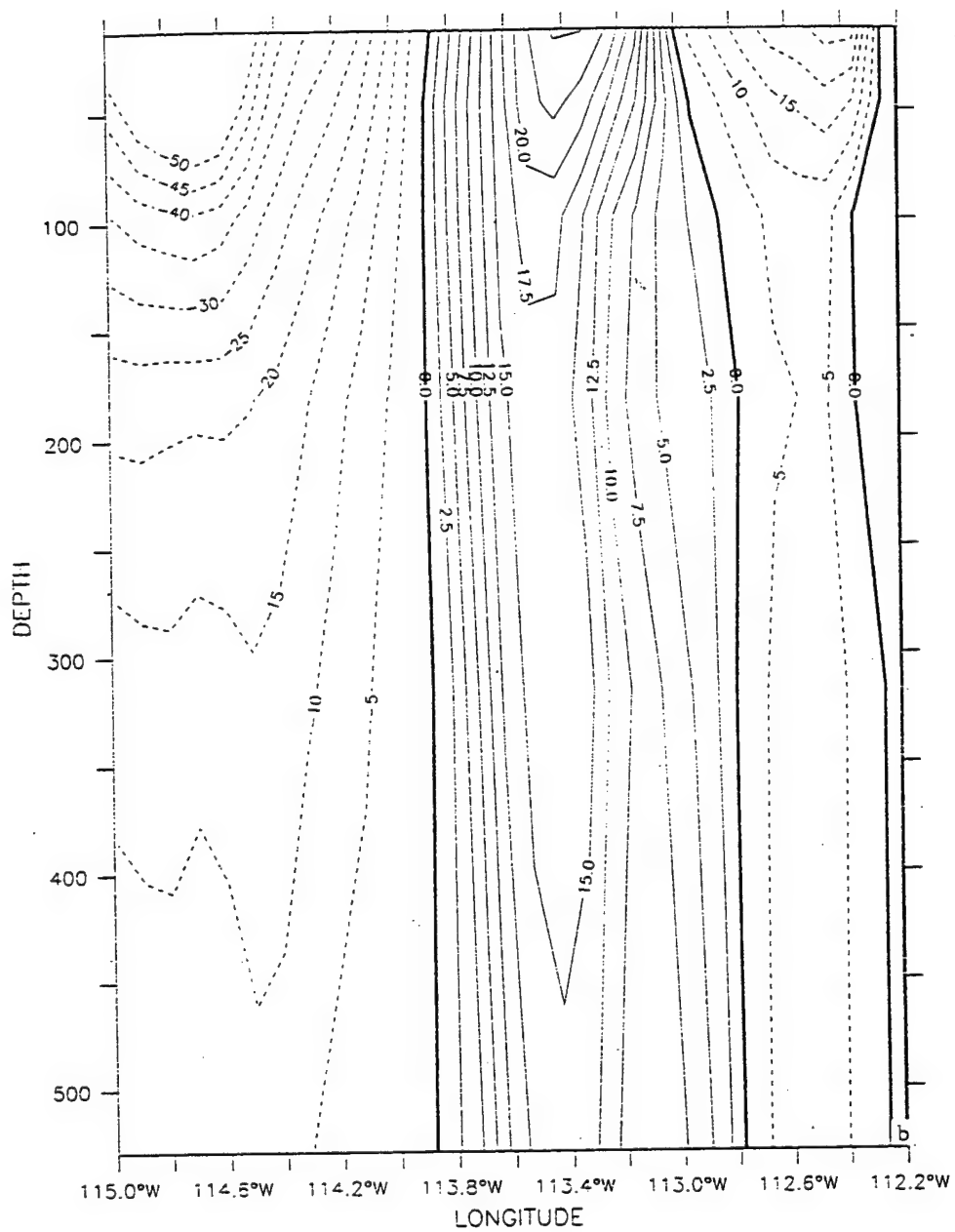
MEAN MERID VELOCITY (cm/sec)

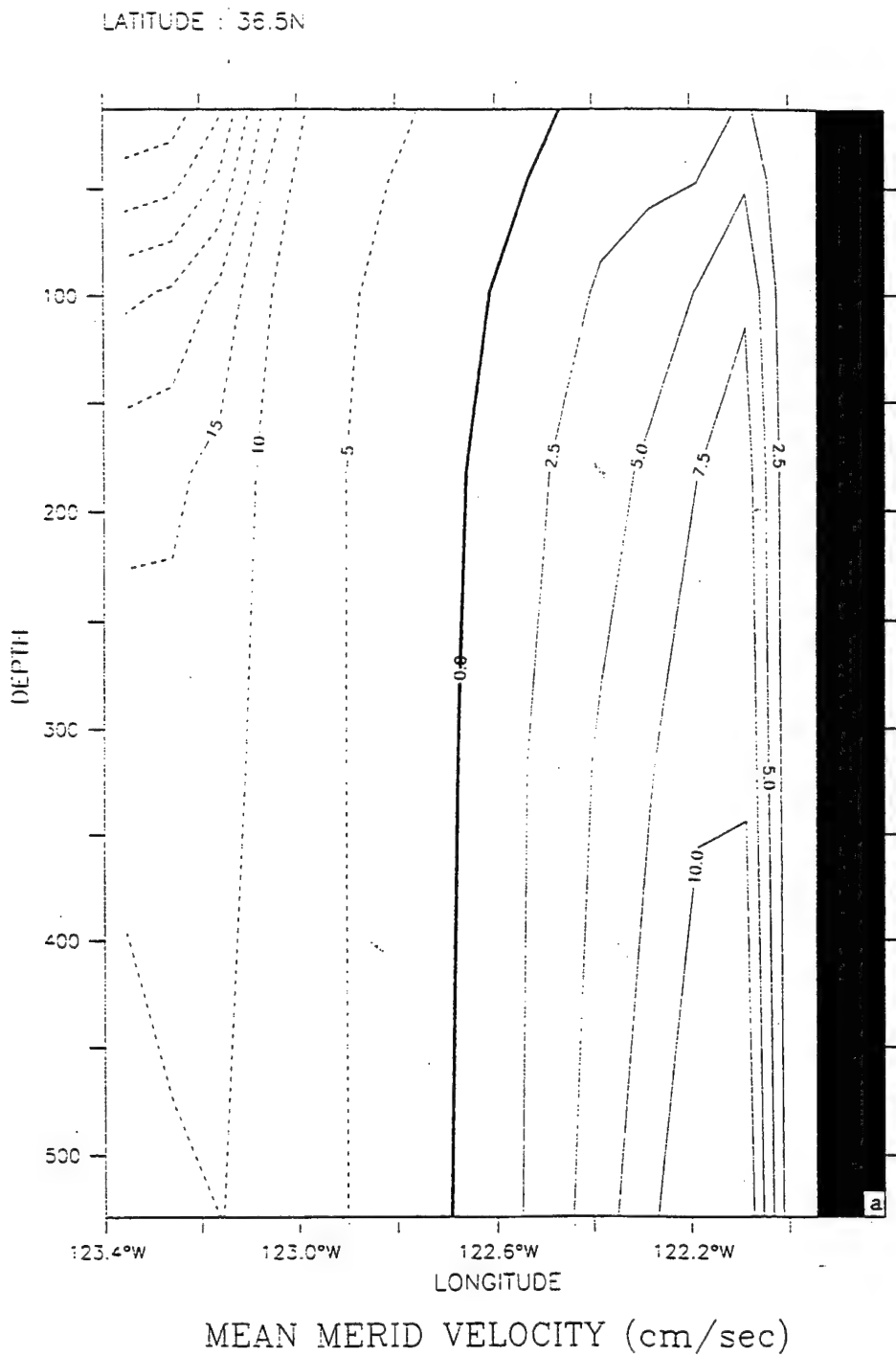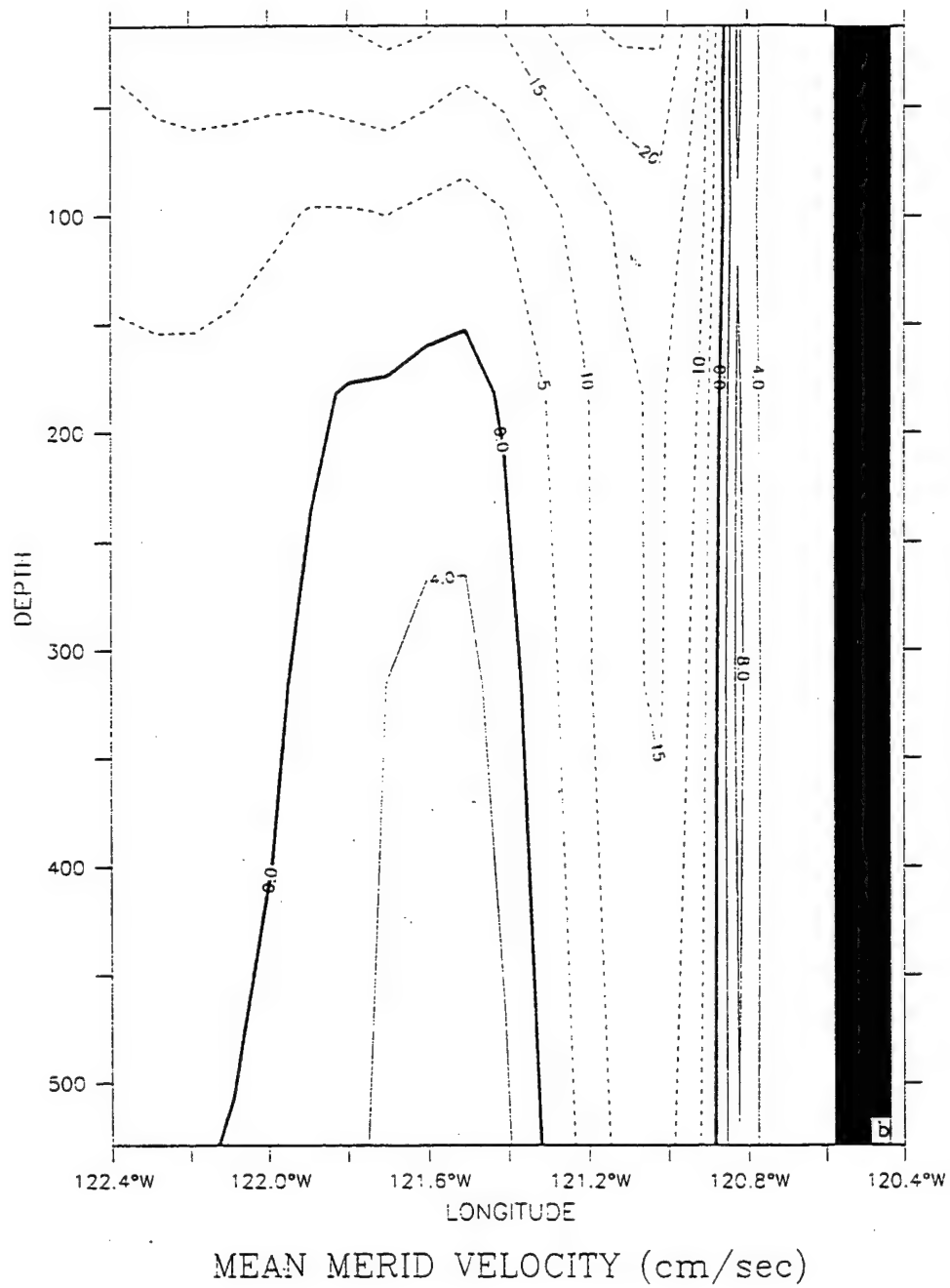MEAN MERID VELOCITY (cm/sec)
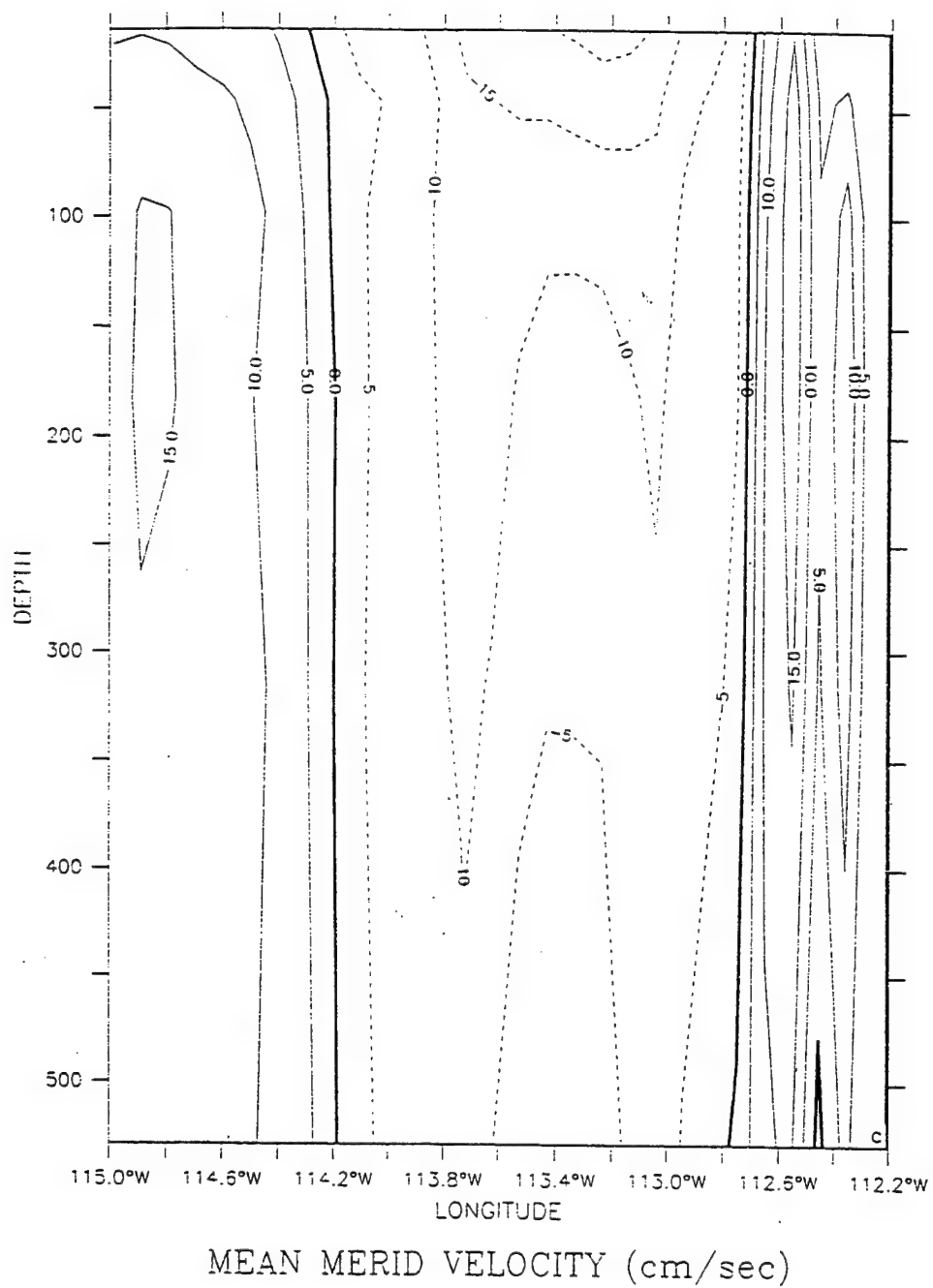
Figure 15. Cross-shore sections of mean v for January of model year 3 at (a) 36.5° N (off Point Sur) and (b) 34.6° N (off Point Conception). The contour interval is 2.5 cm/s (5 cm/s) for poleward (equatorward) flow in (a) and 4 cm/s (5 cm/s) for poleward (equatorward) flow in (b).
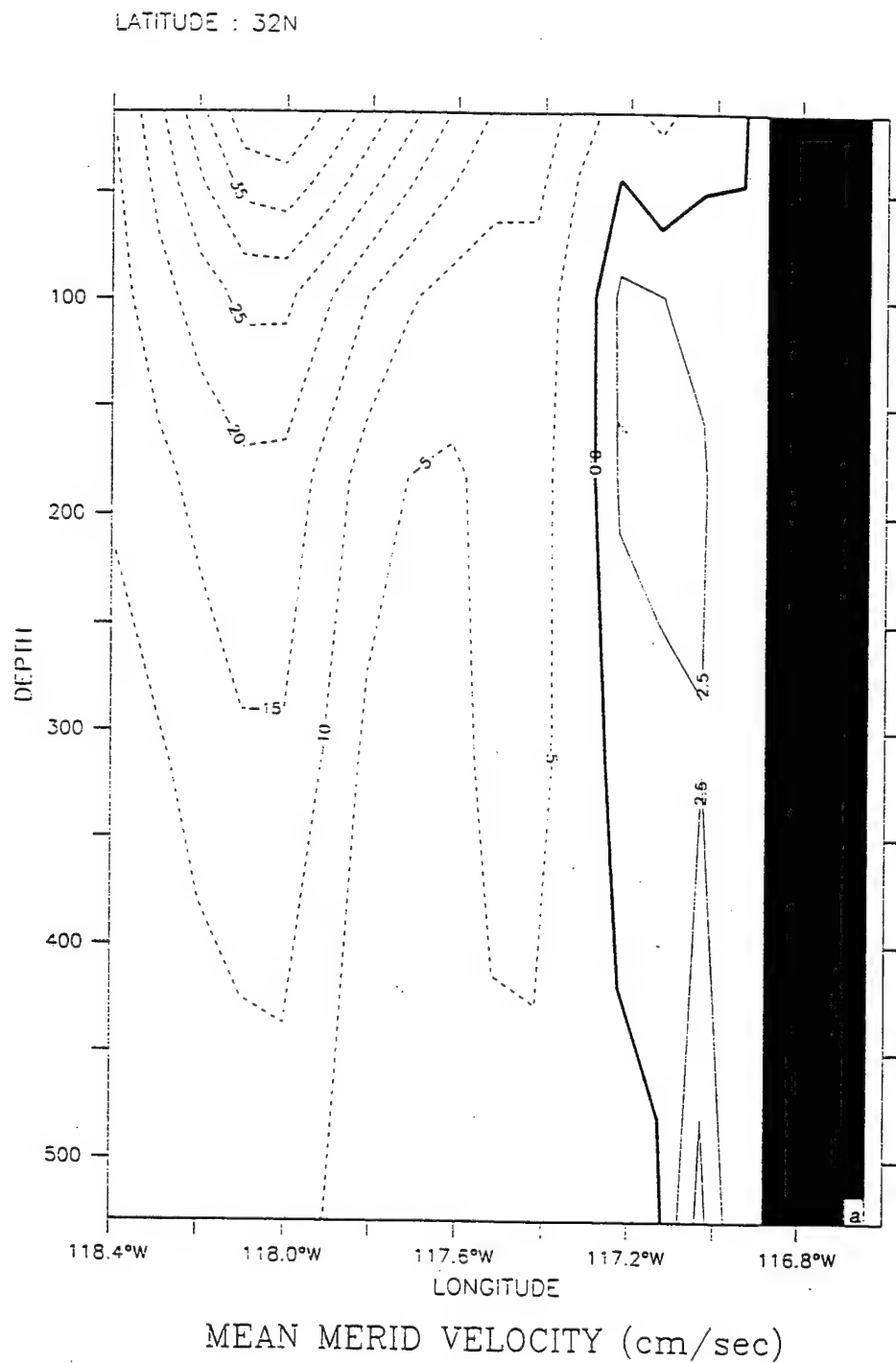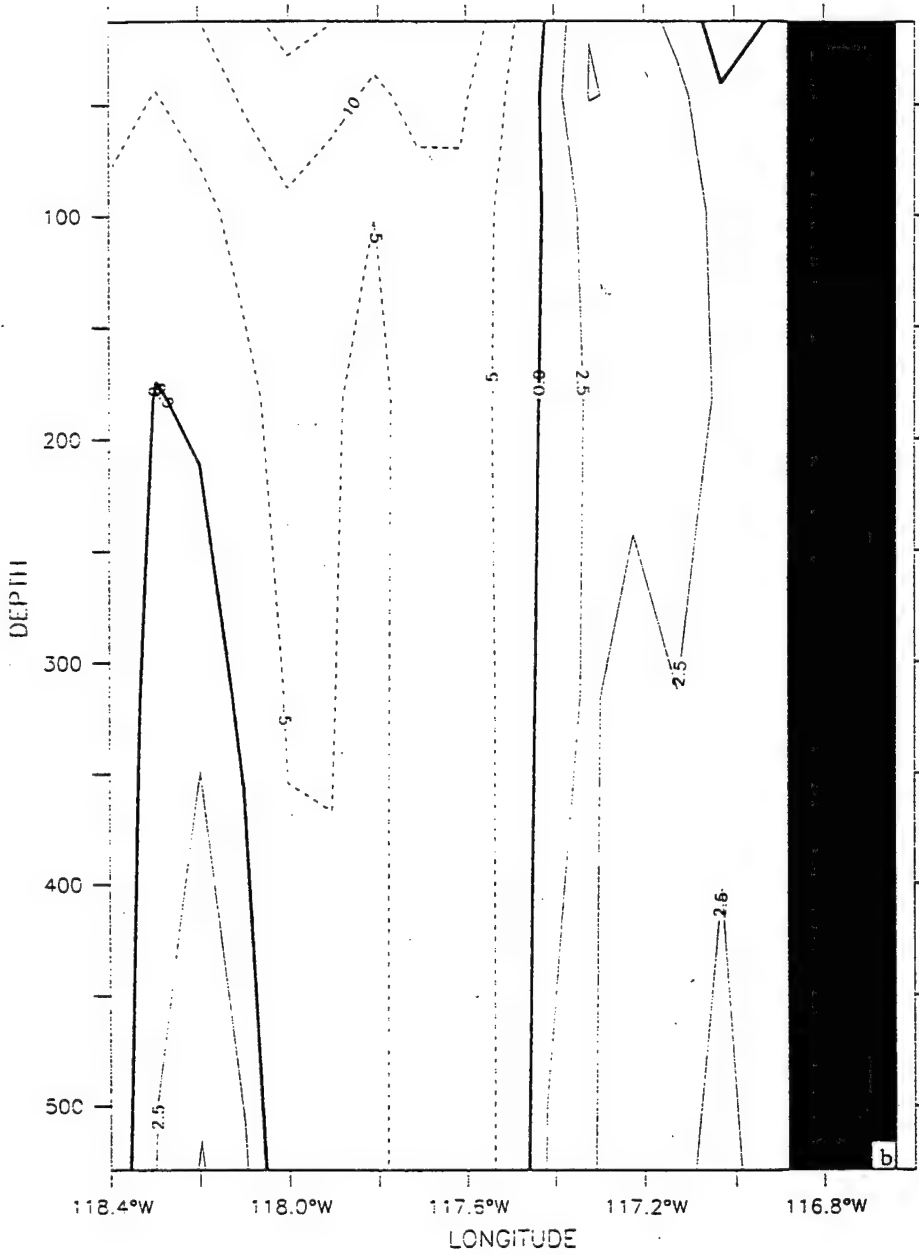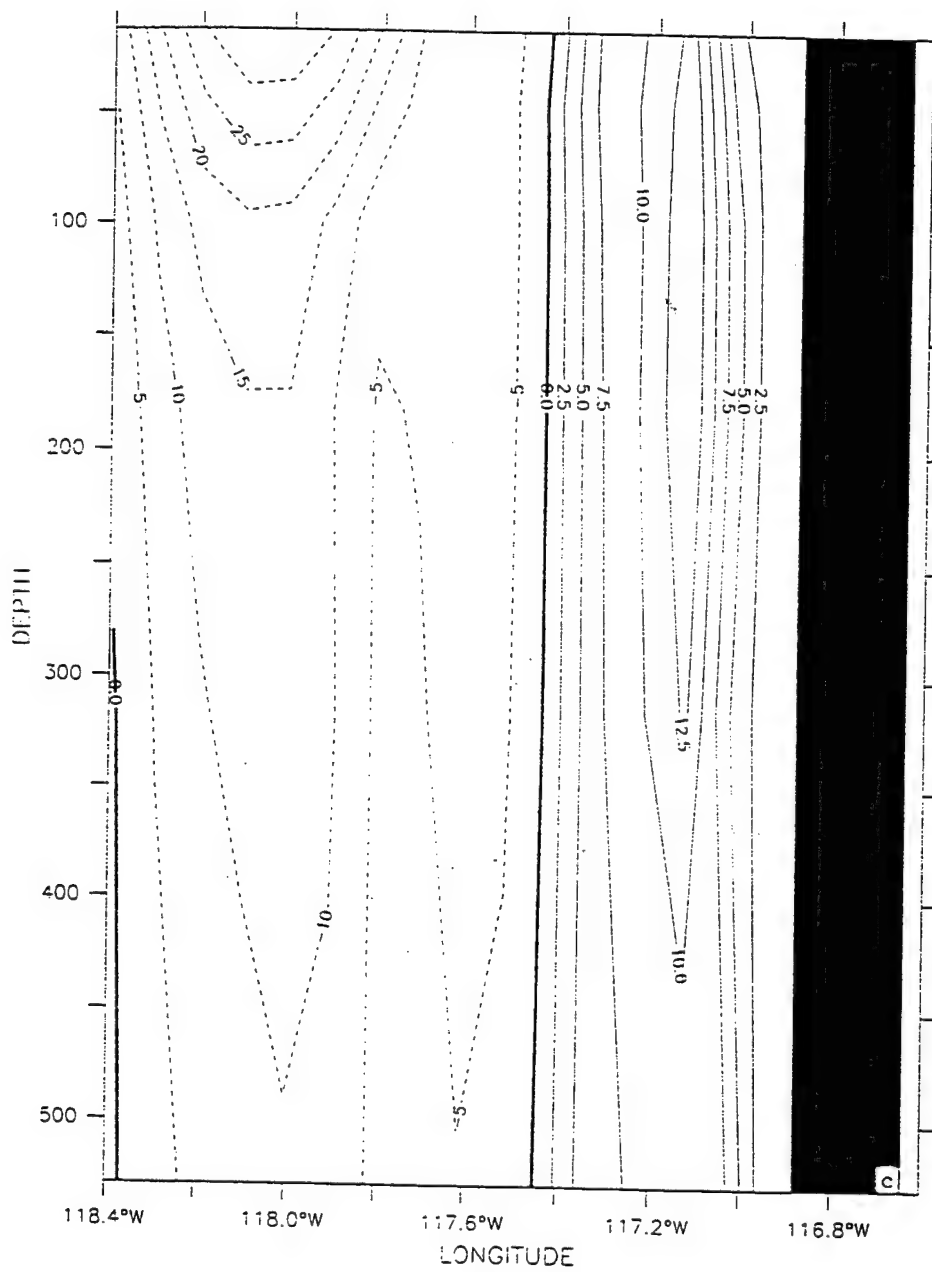
64

LATITUDE : 34.6N

MEAN MERID VELOCITY (cm/sec)

65

MEAN MERID VELOCITY (cm/sec)

Figure 16. Cross-shore sections of mean *v* at 32° N for (a) September, (b) October, and (c) November of model year 3. The contour interval is 2.5 cm/s (5 cm/s) for poleward (equatorward) flow.

66

MEAN MERID VELOCITY (cm/sec)

LATITUDE : 32N

MEAN MERID VELOCITY (cm/sec)
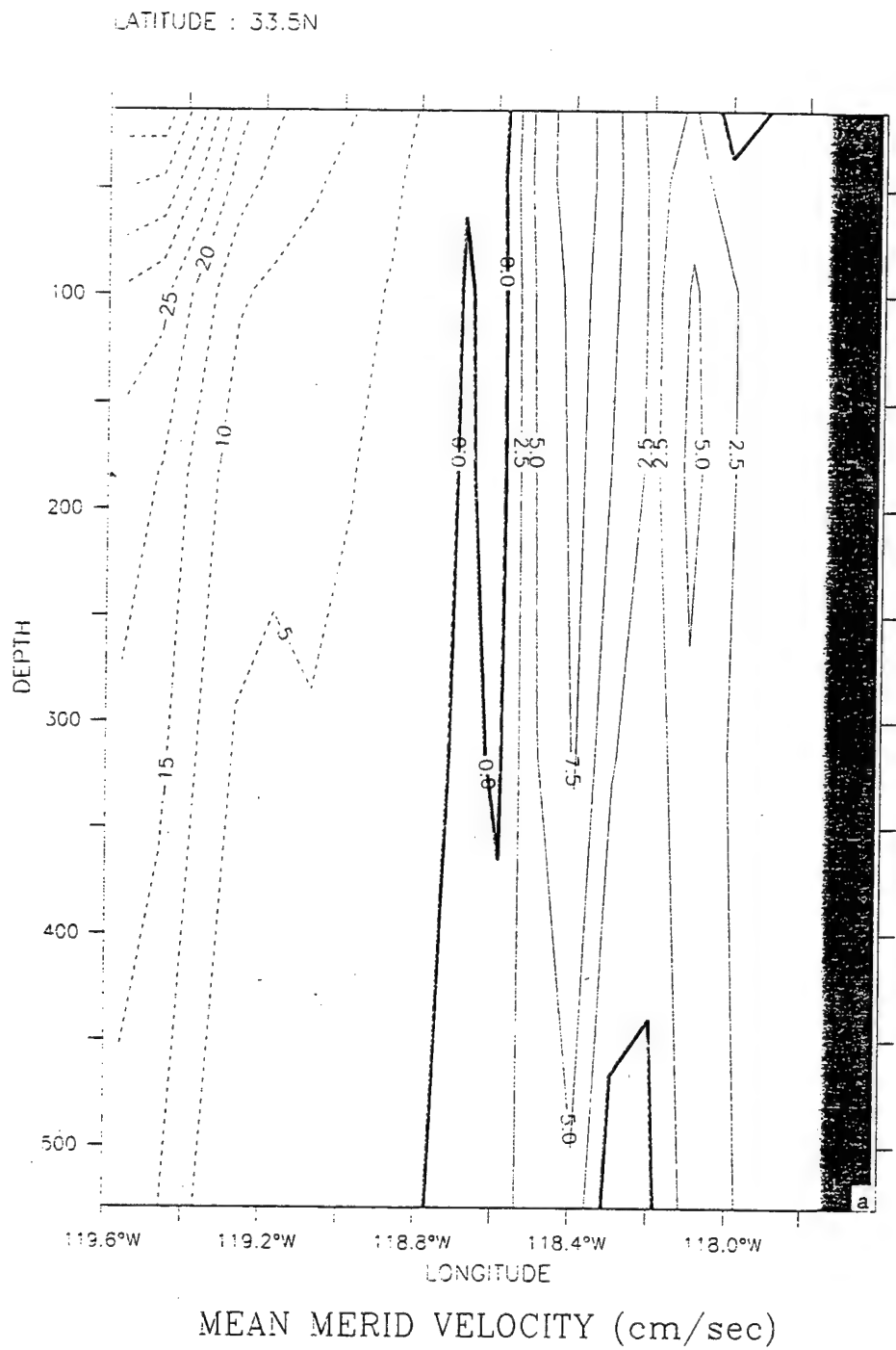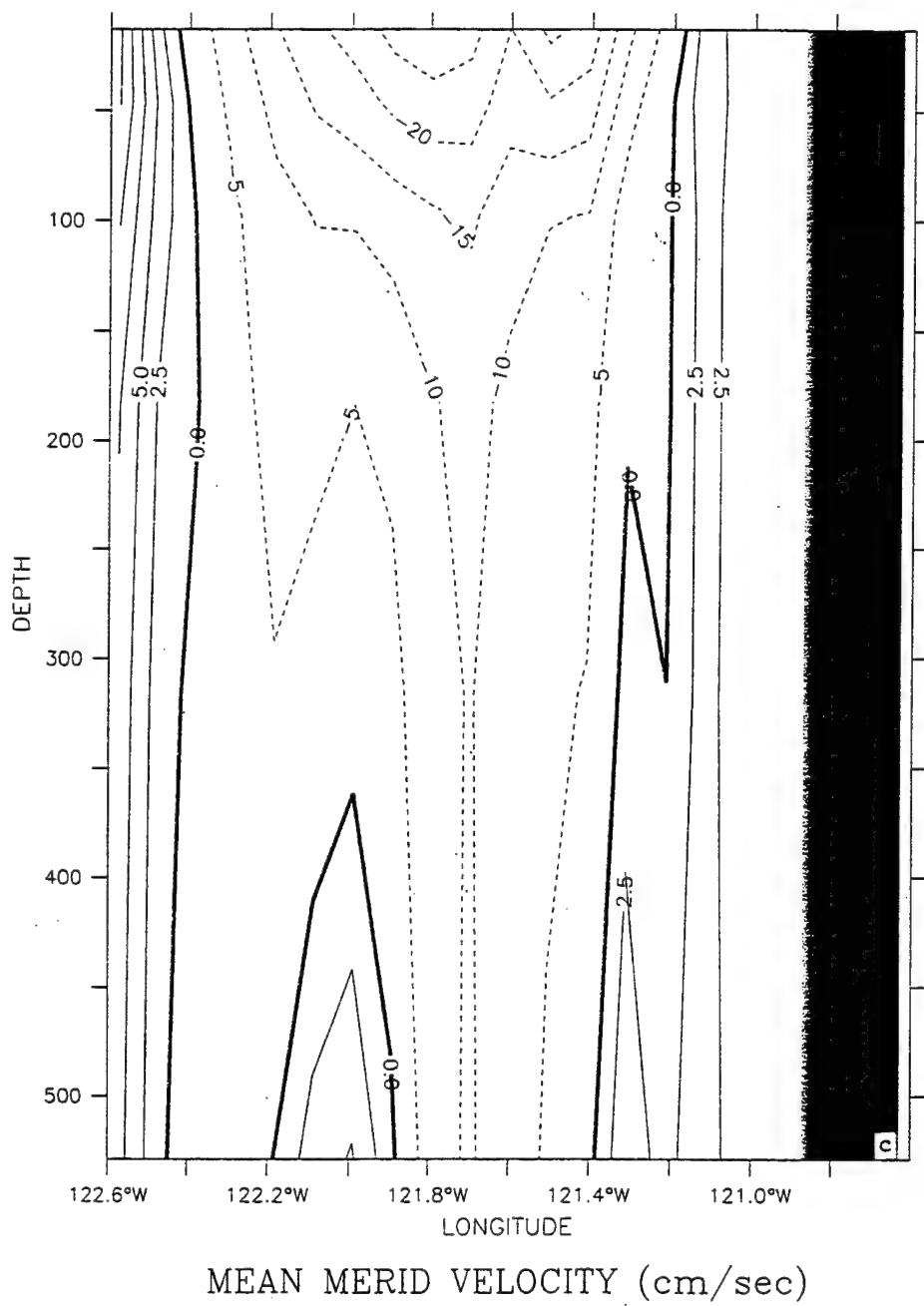
MEAN MERID VELOCITY (cm/sec)

Figure 17. Cross-shore sections of mean v for November of model year 3 at (a) 33.5° N (south of Point Conception), (b) 34.6° N (off Point Conception), and (c) 35.5° N (north of Point Conception). The contour interval is 2.5 cm/s (5 cm/s) for poleward (equatorward) flow.

LATITUDE : 34.6N

MEAN MERID VELOCITY (cm/sec)

LATITUDE : 35.5N
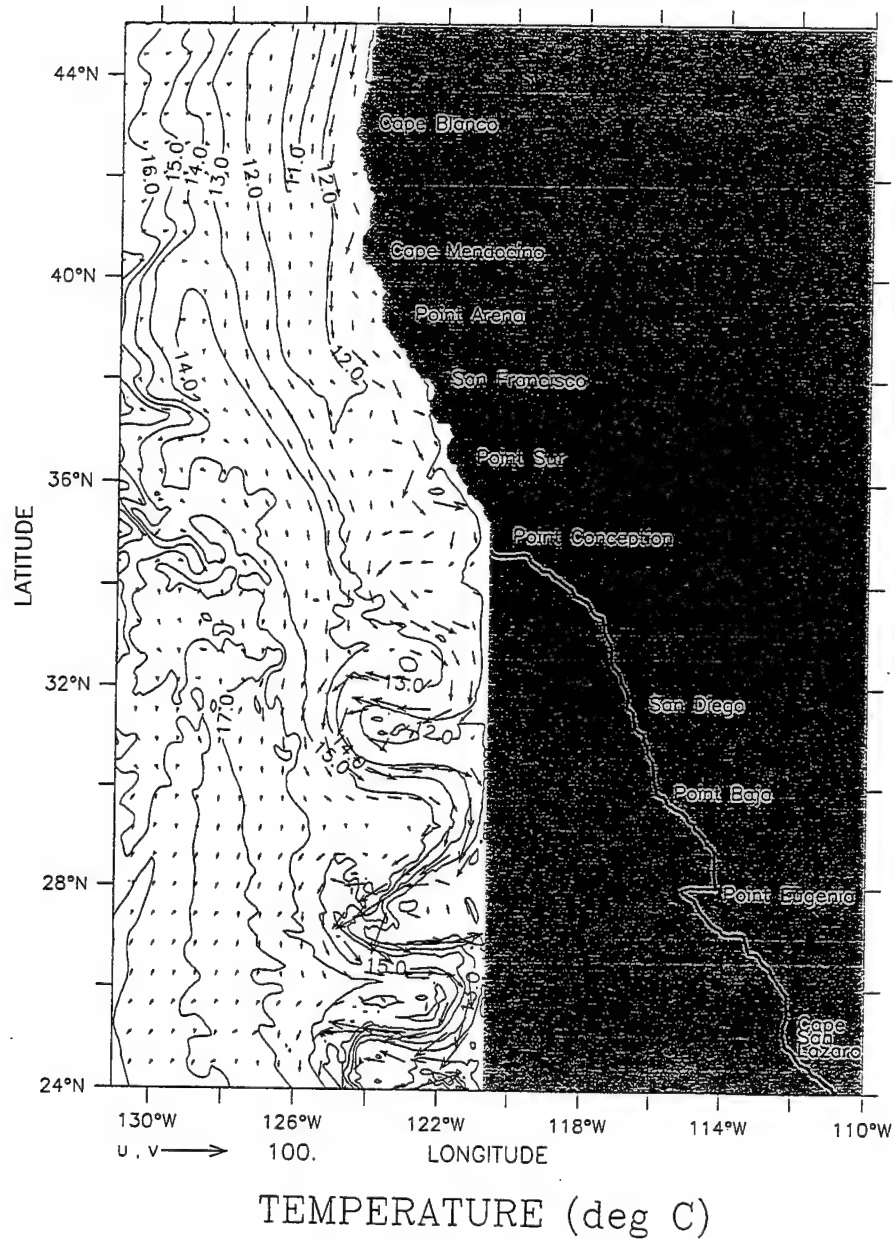

MEAN MERID VELOCITY (cm/sec)

71

DEPTH : 13m

Figure 18. The straight coastline south of Point Conception used in experiment 2 is depicted by the shaded area. Temperature contours and velocity vectors in experiment 2, for day 285 (mid-October). The contour interval is 1° C; maximum velocity vector is 100 cm/s.

72

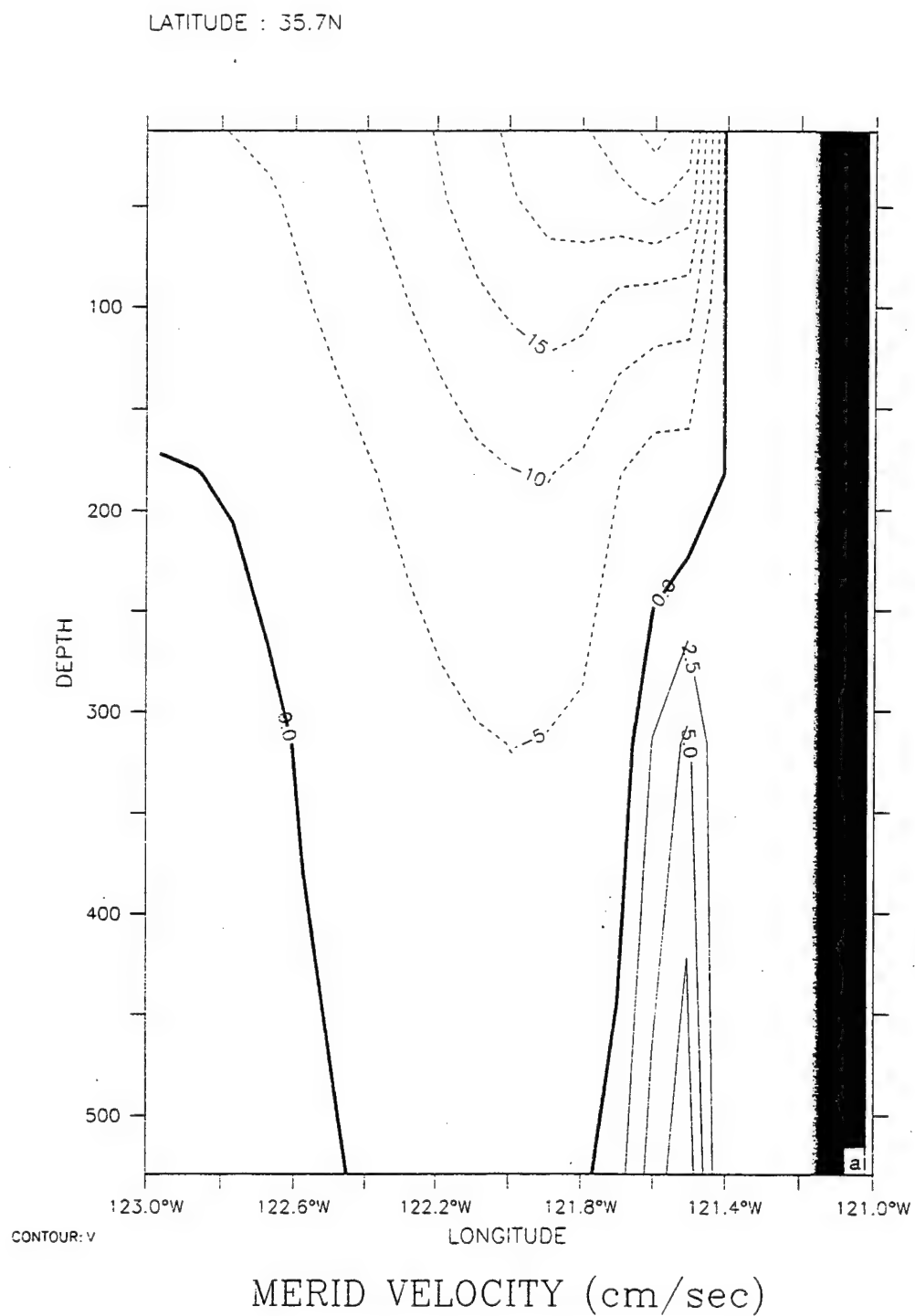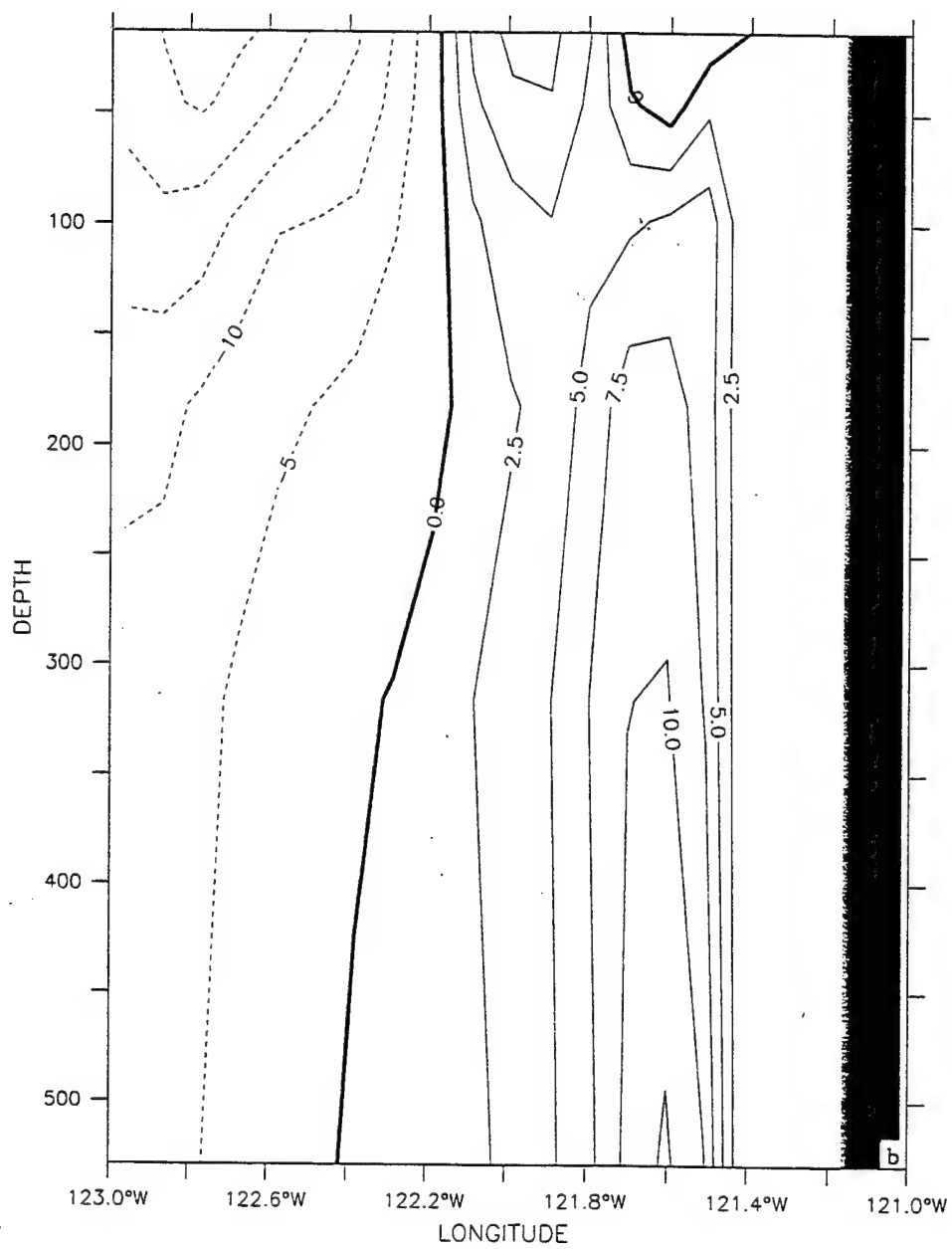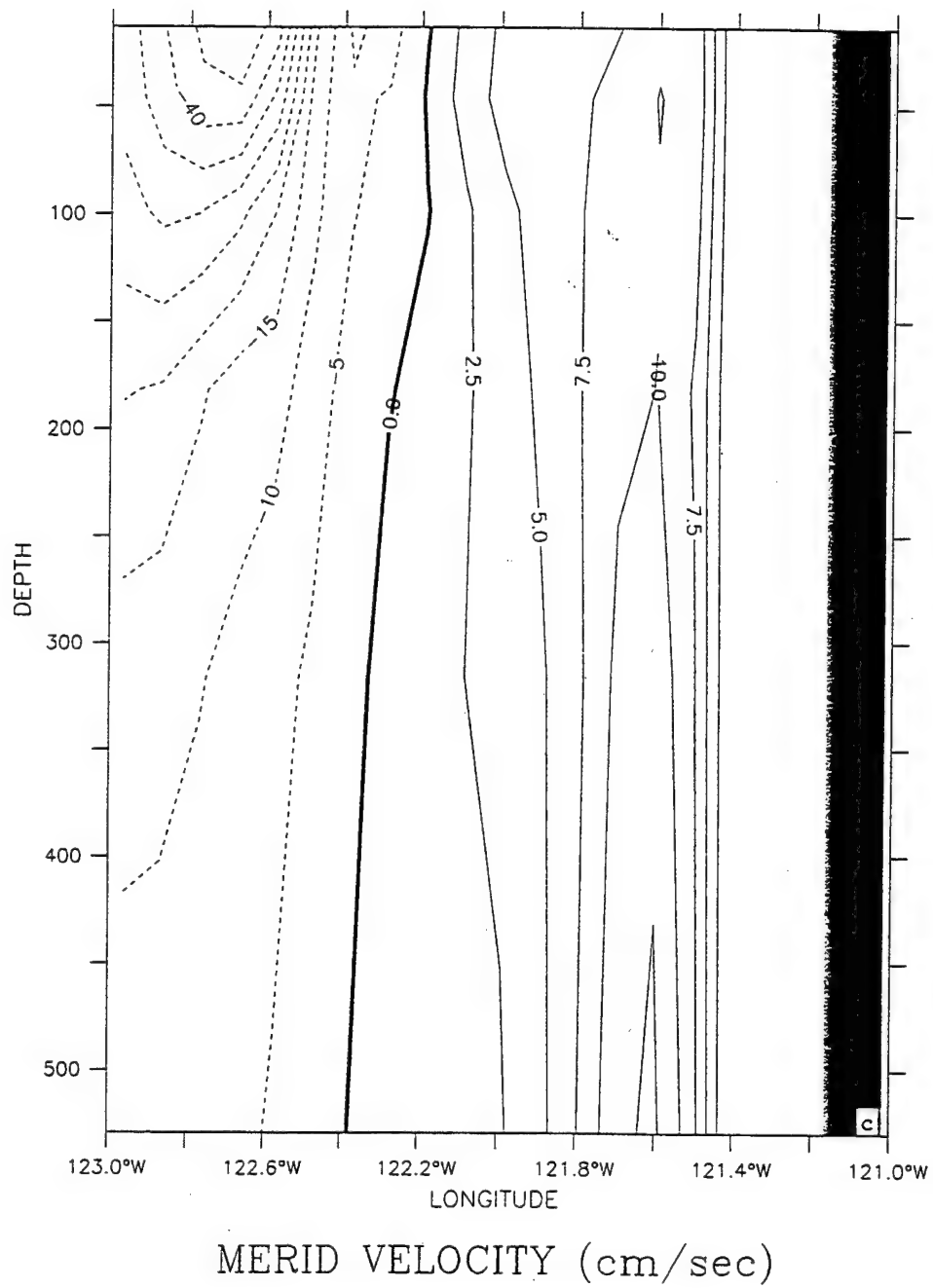LATITUDE : 35.7N

MERID VELOCITY (cm/sec)

Figure 19. Cross-shore sections of mean *v* of experiment 2 at 35.7° N in (a) mid-September, (b) mid-October and (c) mid-November. The contour interval is 2.5 cm/s (5 cm/s) for poleward (equatorward) flow.

LATITUDE : 35.7N
T (DAY) : 285

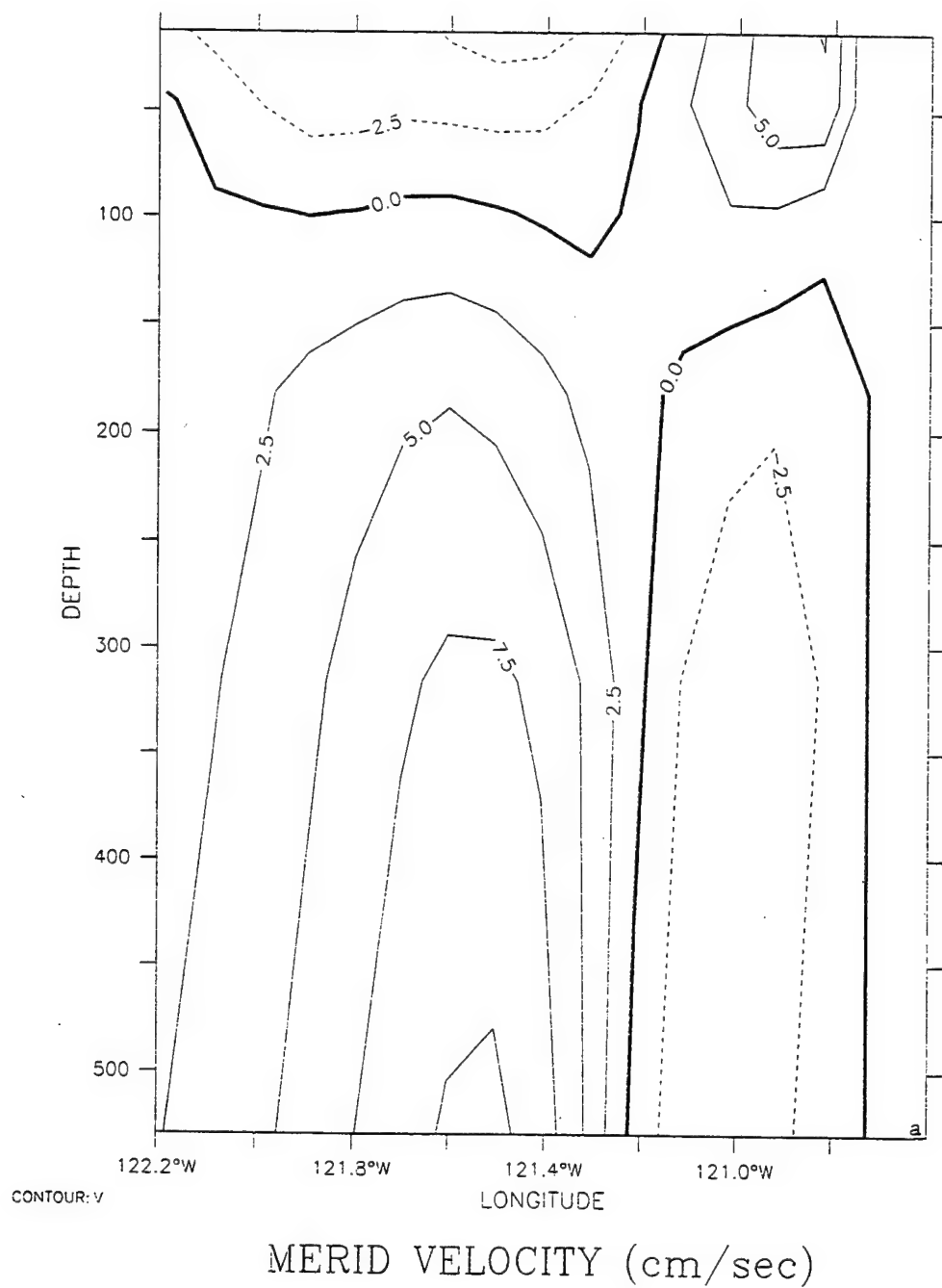MERID VELOCITY (cm/sec)

MERID VELOCITY (cm/sec)

Figure 20. Cross-shore sections of mean *v* of experiment 2 in mid-November at (a) 34.1°
N (south of Point Conception) and (b) 34.8° N (off Point Conception). The contour
interval is 2.5 cm/s in (a) and 2.5 cm/s (5 cm/s) for poleward (equatorward) flow in (b).

LATITUDE : 34.8N
T (DAY) : 315
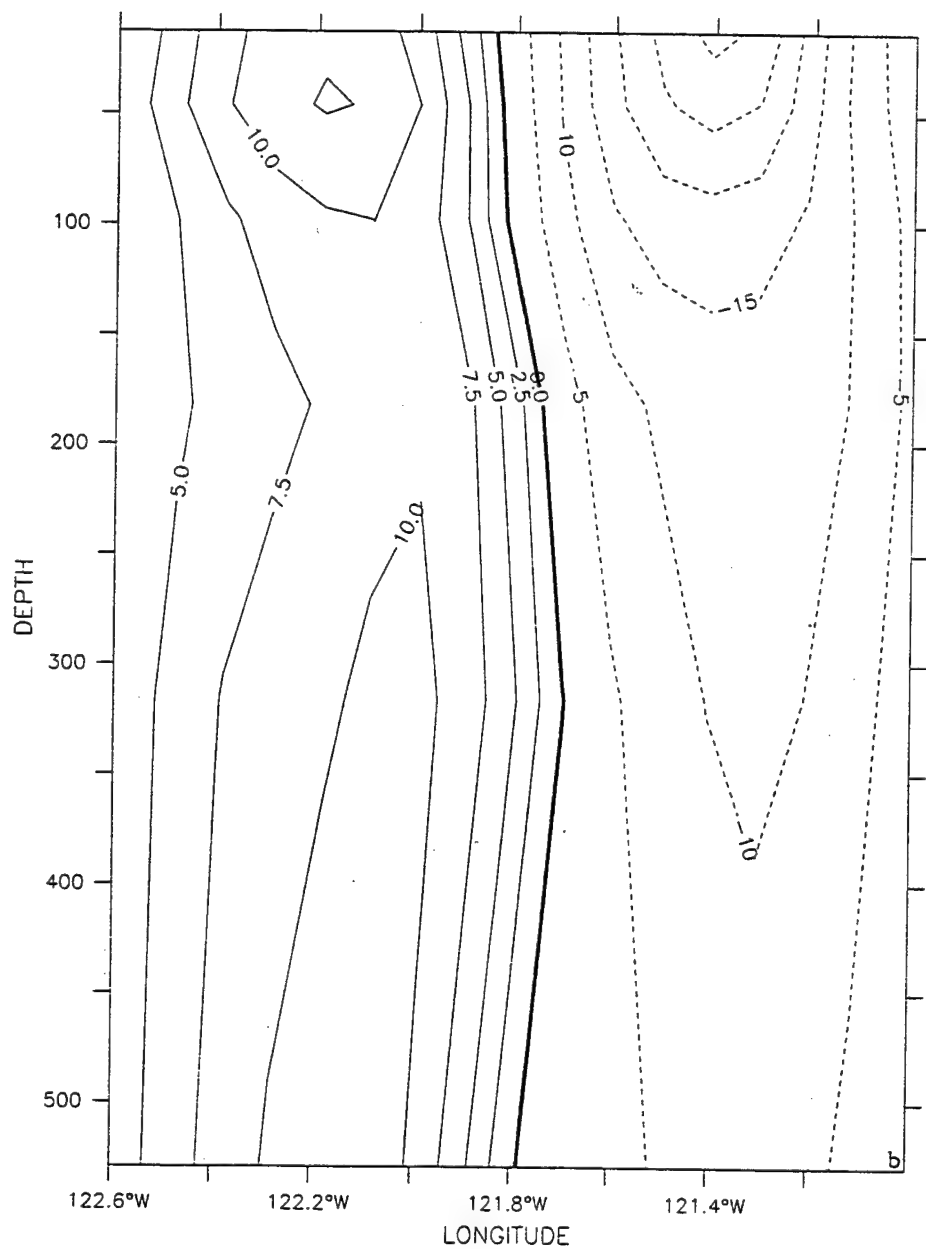
MERID VELOCITY (cm/sec)

DEPTH : 13m

KINETIC ENERGY TRANSFER ((cm/sec)**2)

Plate 1. Horizontal maps at 13 m depth of mean kinetic energy transfers (a, c) and potential energy transfers (b, d), averaged over days 180-195 in the northern portion of the domain (a, b) and the southern portion of the domain (c, d). Contour interval is 0.2 cm²/s² for (a), 2.0 cm²/s² for (b, c), and 5.0 cm²/s² for (d).

78

DEPTH : 13m

POTENTIAL ENERGY TRANSFER ((cm/sec)**2)

79

DEPTH : 13m

KINETIC ENERGY TRANSFER ((cm/sec)**2)

80

DEPTH : 13m

POTENTIAL ENERGY TRANSFER ((cm/sec)**2)

81

DEPTH : 13m

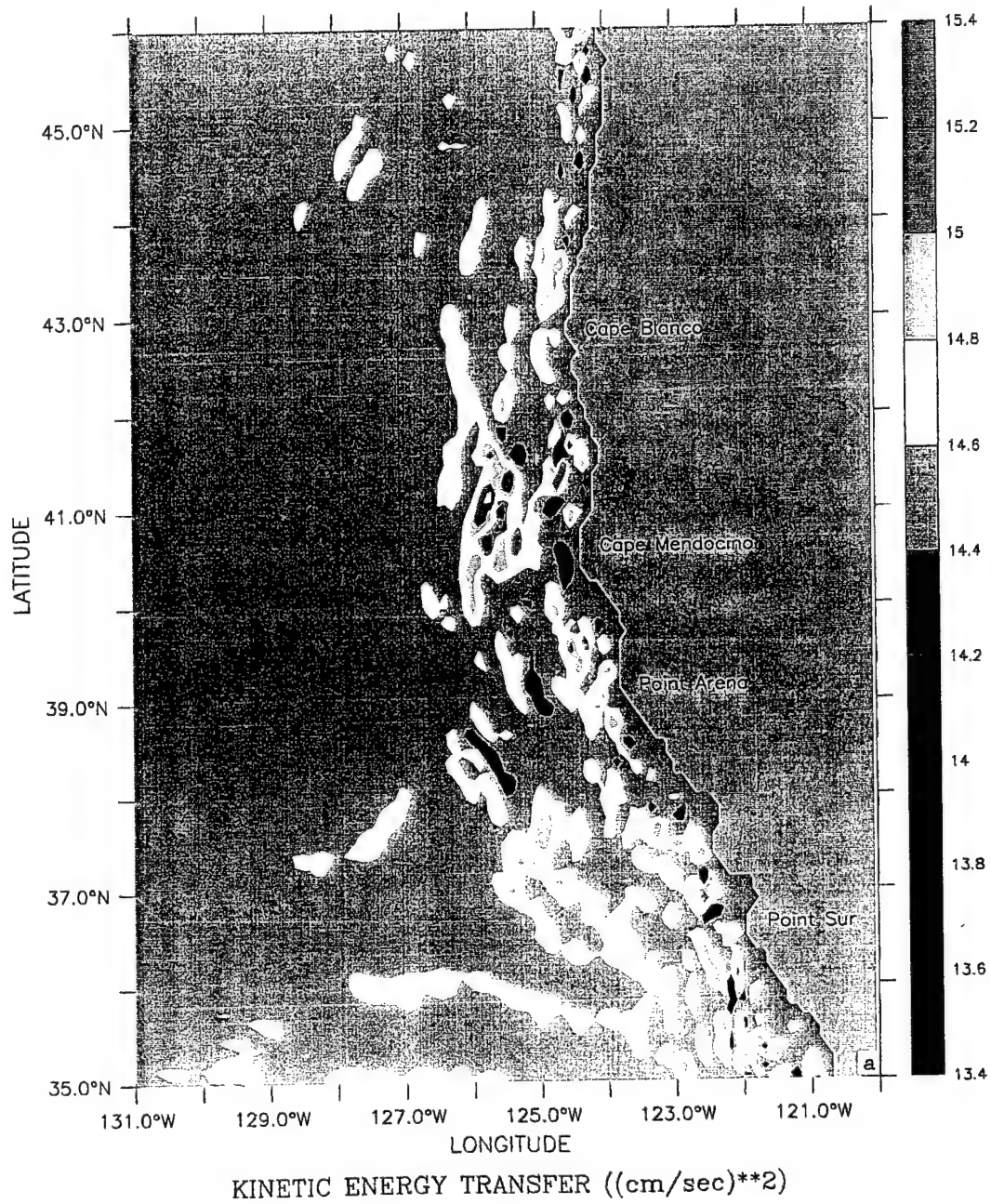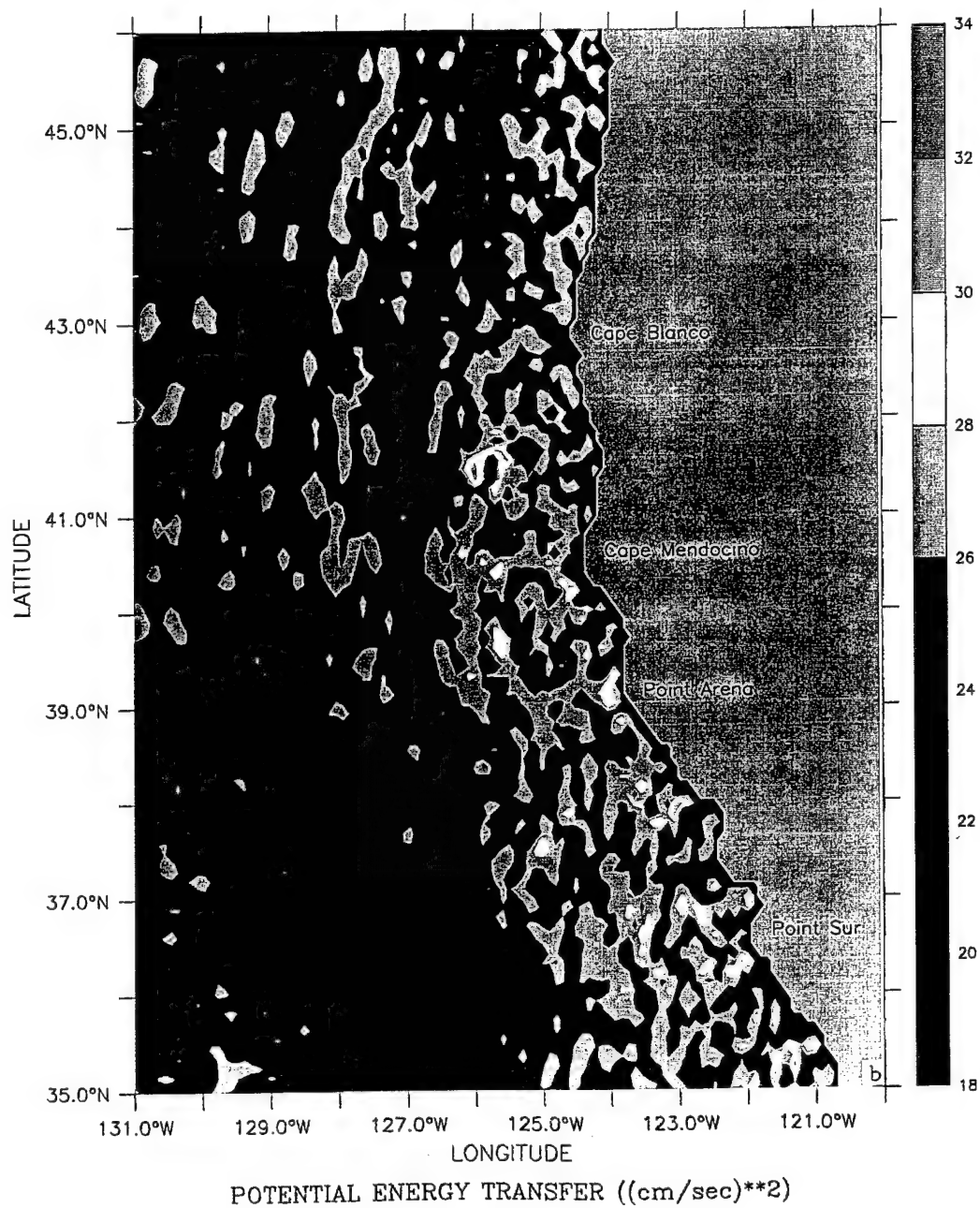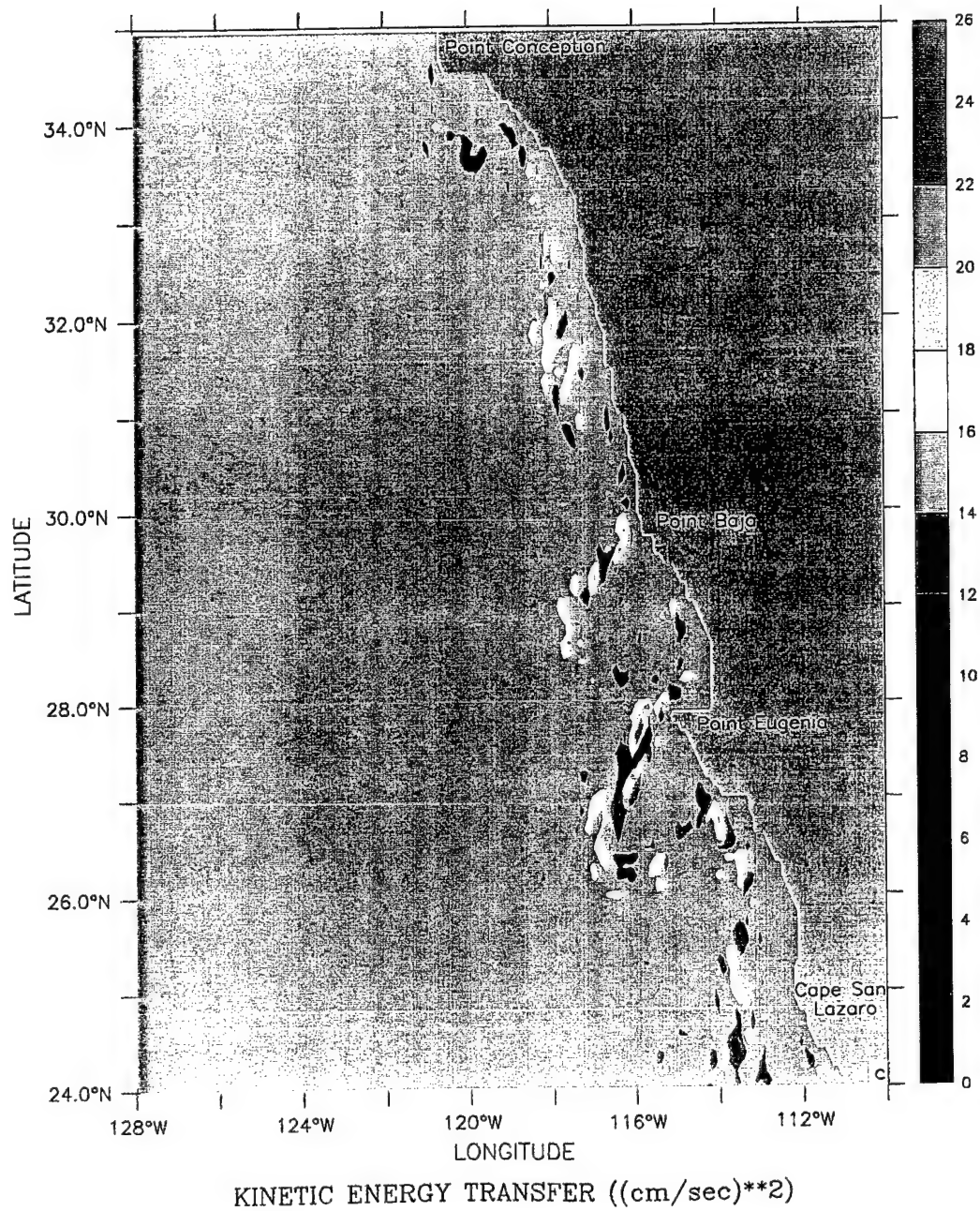KINETIC ENERGY TRANSFER ((cm/sec)**2)
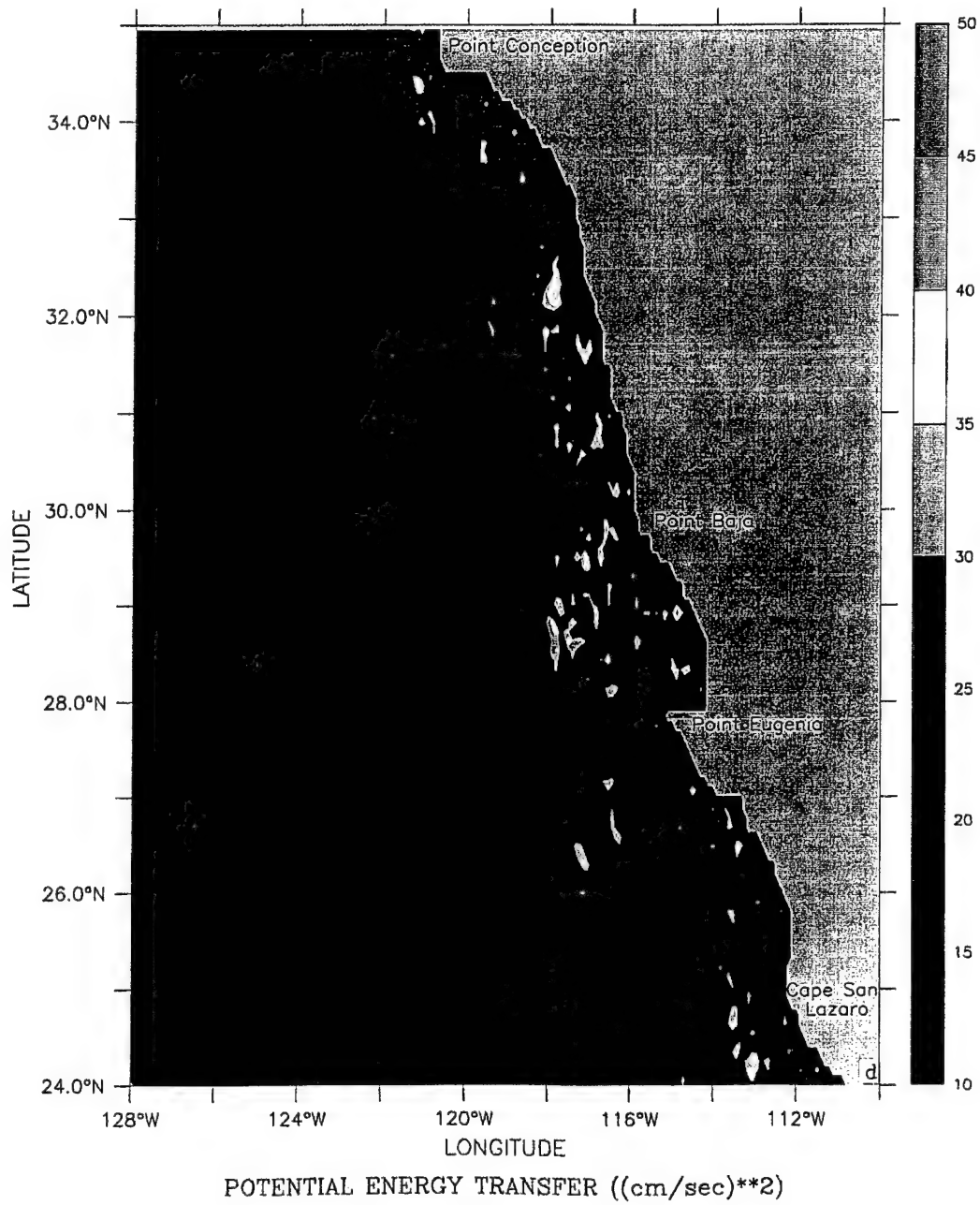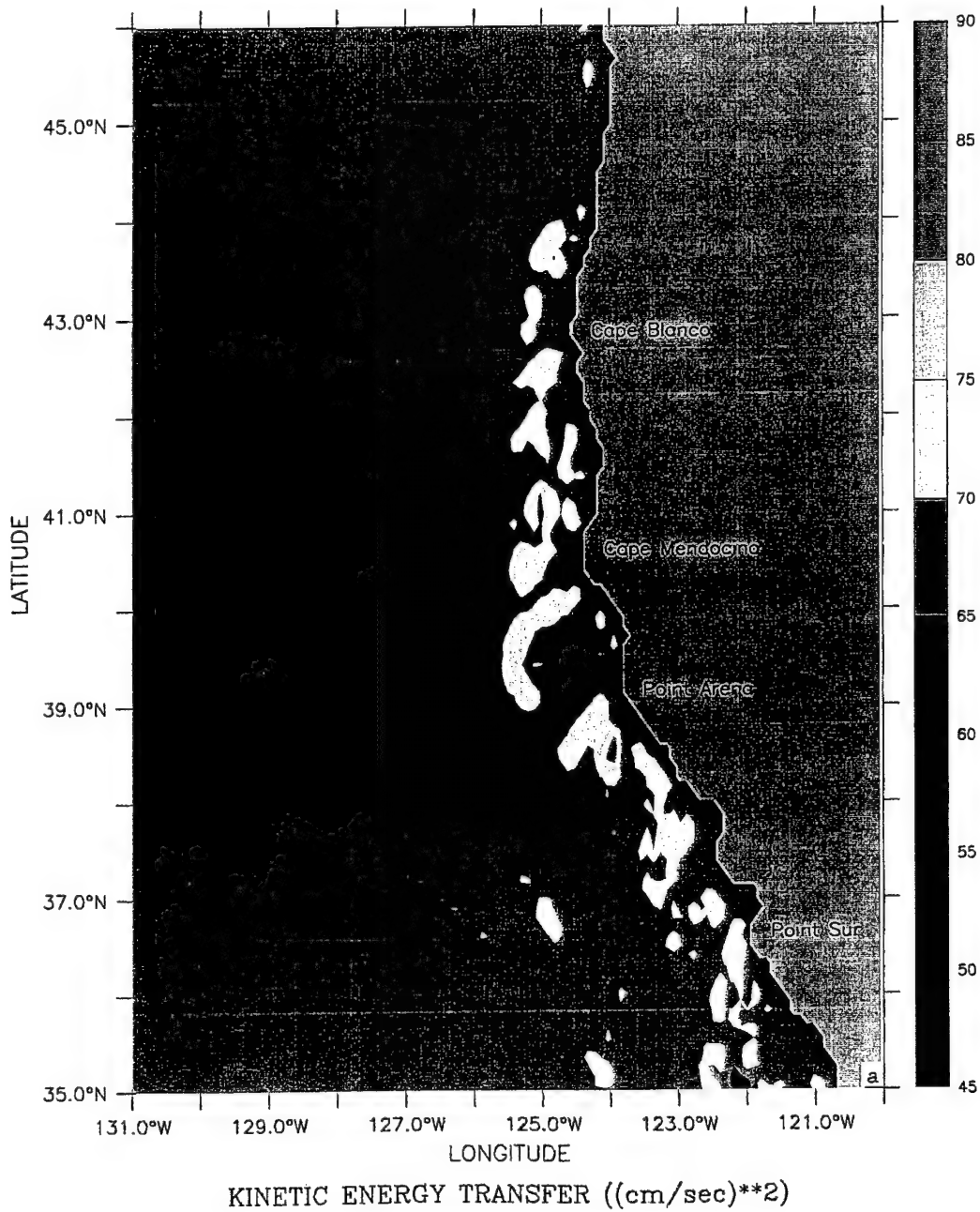
Plate 2. Horizontal maps at 13 m depth of mean kinetic energy transfers (a, c) and potential energy transfers (b, d), averaged over days 270-285 in the northern portion of the domain (a, b) and the southern portion of the domain (c, d). Contour interval is 5.0 cm²/s² for (a), (c), and (d), and 2.0 cm²/s² for (b).

82

DEPTH : 13m

POTENTIAL ENERGY TRANSFER ((cm/sec)**2)

83

DEPTH : 13m

KINETIC ENERGY TRANSFER ((cm/sec)**2)

DEPTH : 13m

POTENTIAL ENERGY TRANSFER ((cm/sec)**2)

DEPTH : 13m

LATITUDE
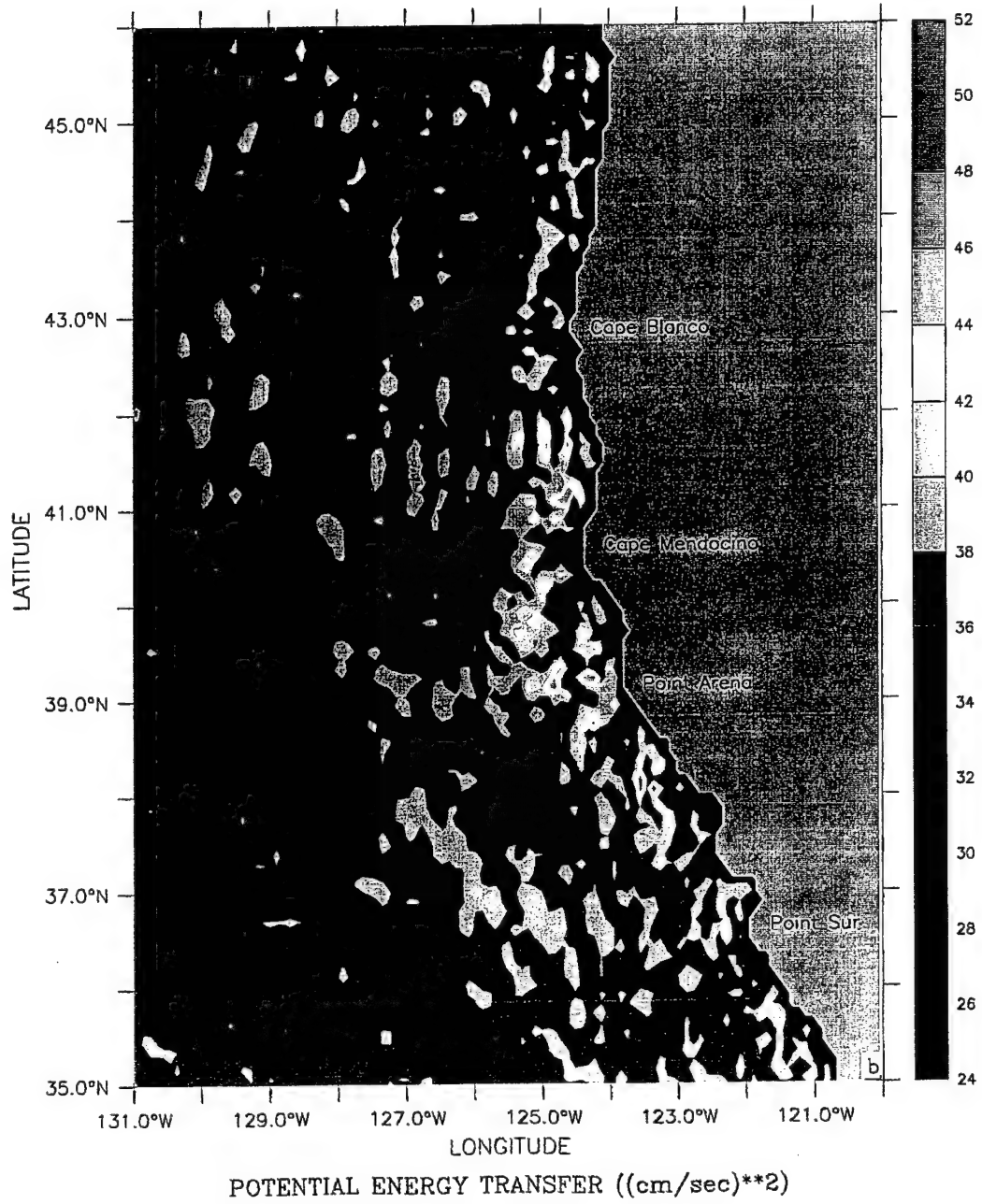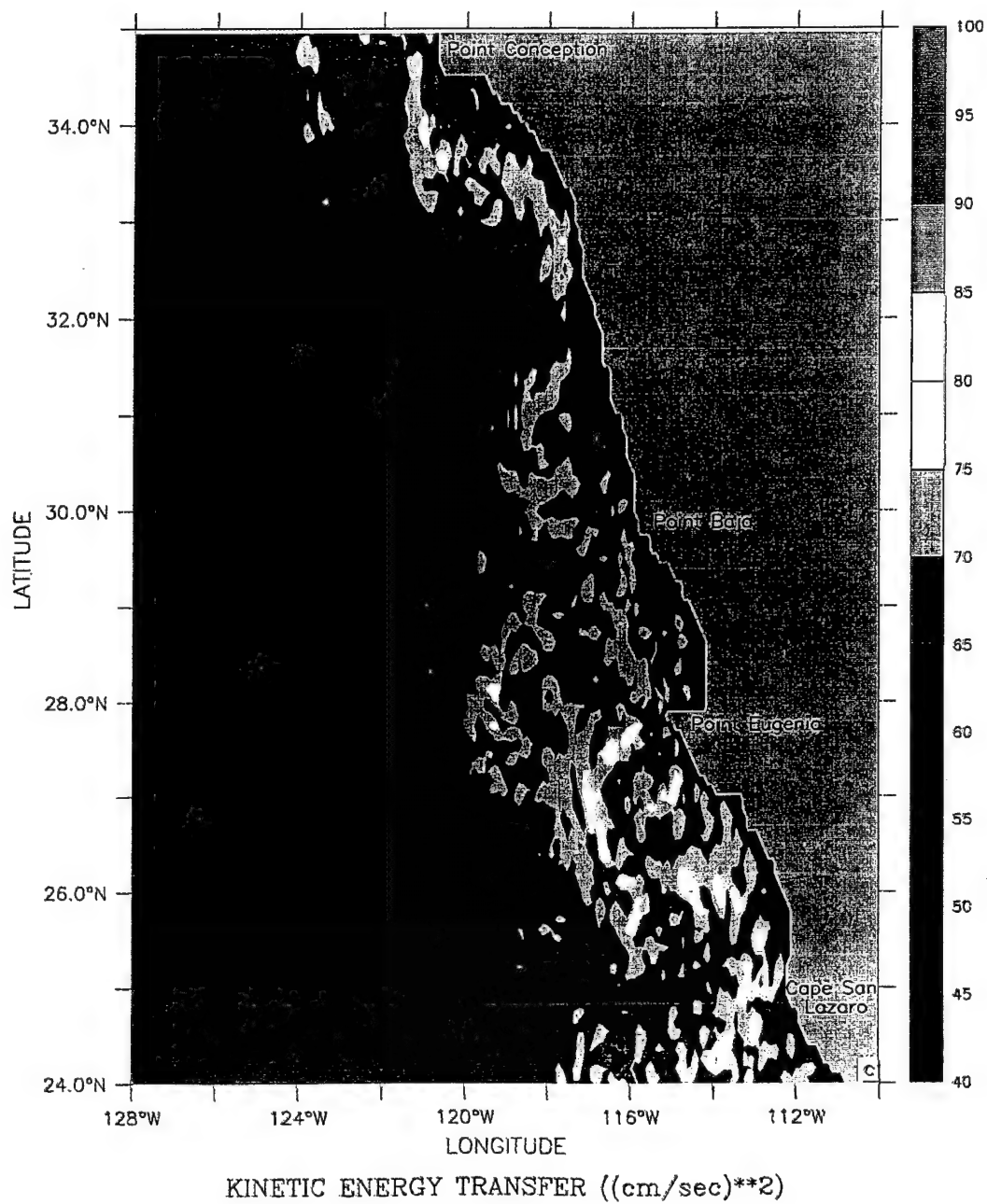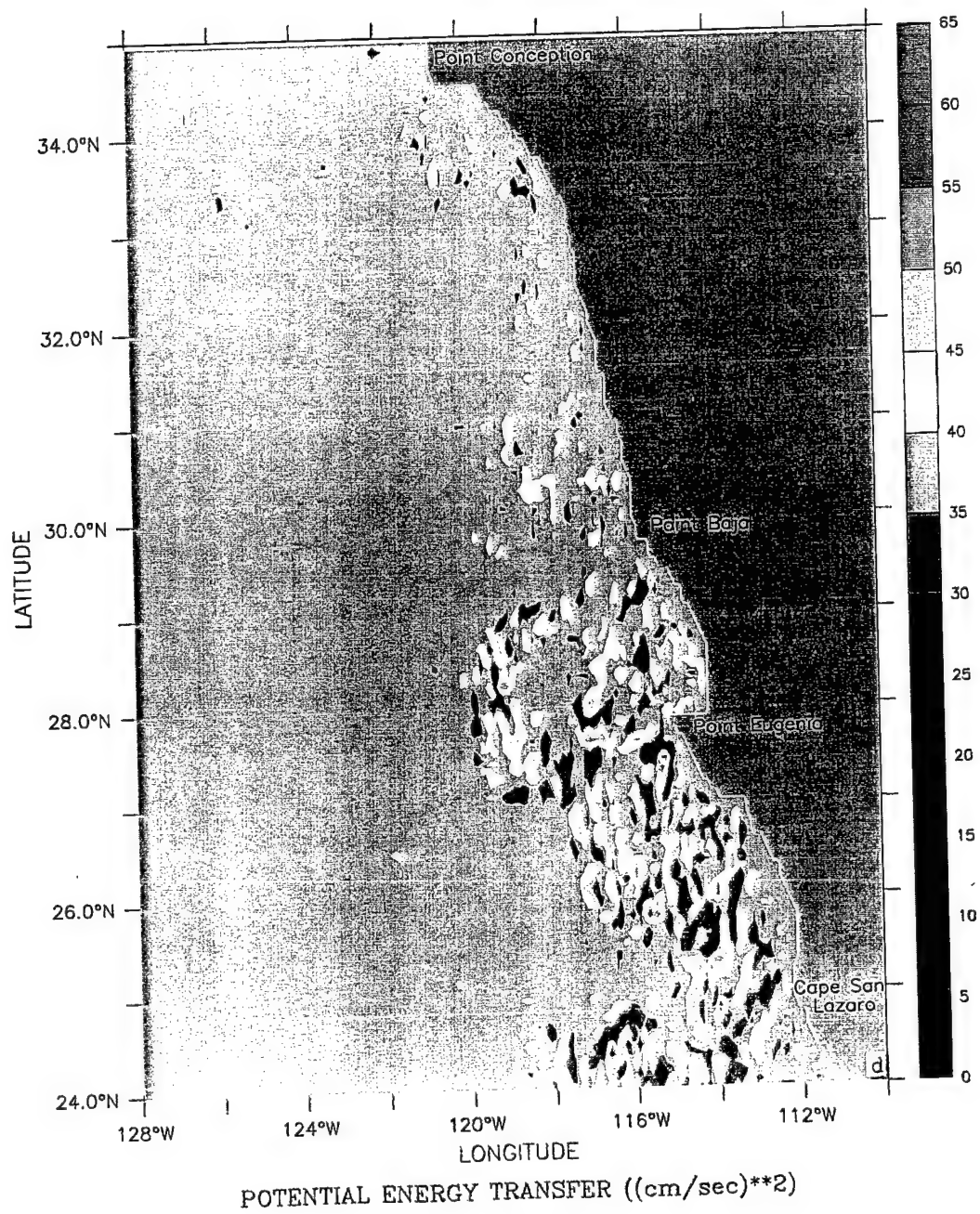
MEAN TEMPERATURE (deg C)
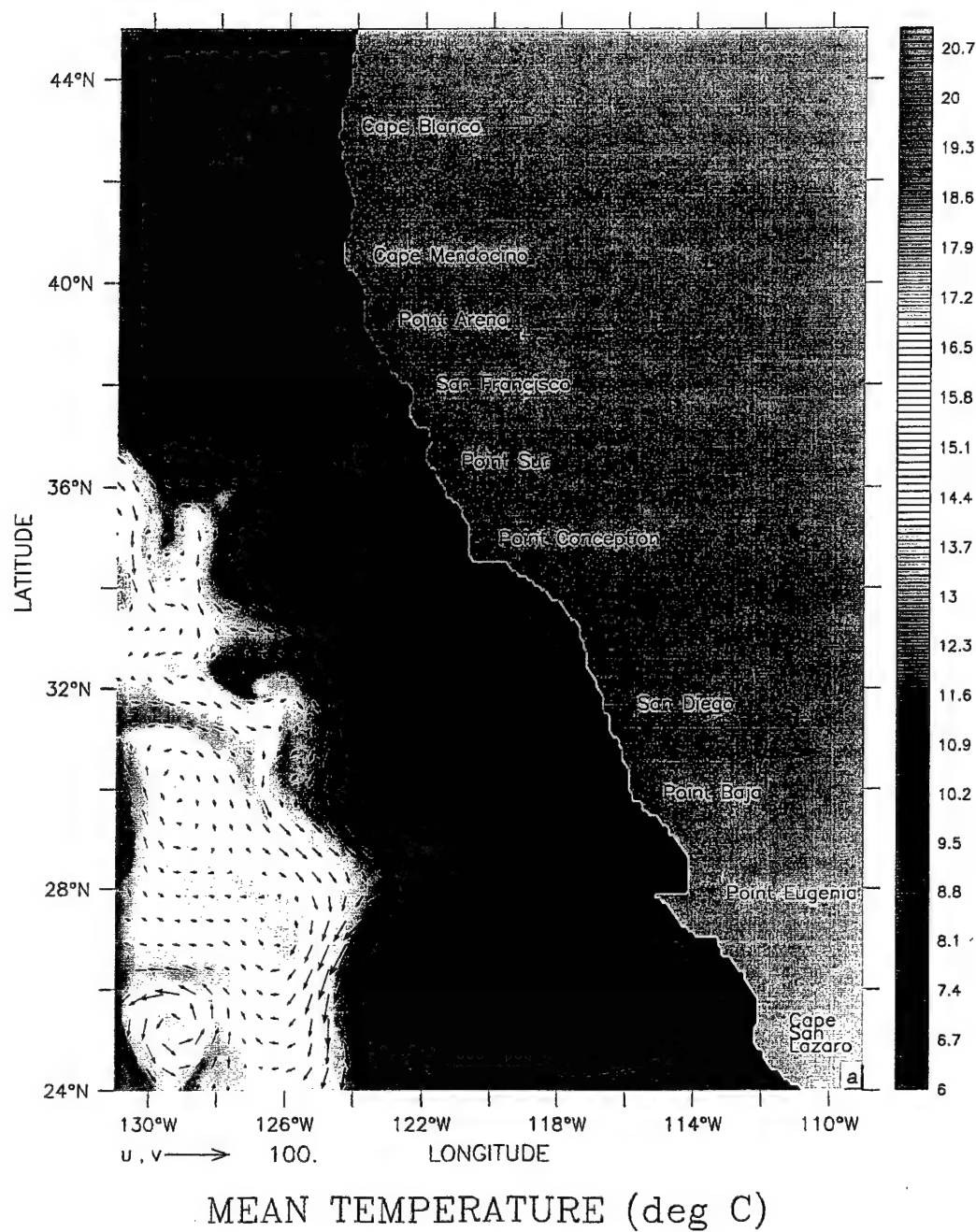
Plate 3. Mean temperature and velocity vectors at 13 m depth for (a) January, (b) April, (c) July, and (d) October of model year 3. Contour interval is 0.1° C; maximum velocity vector is 100 cm/s.

86
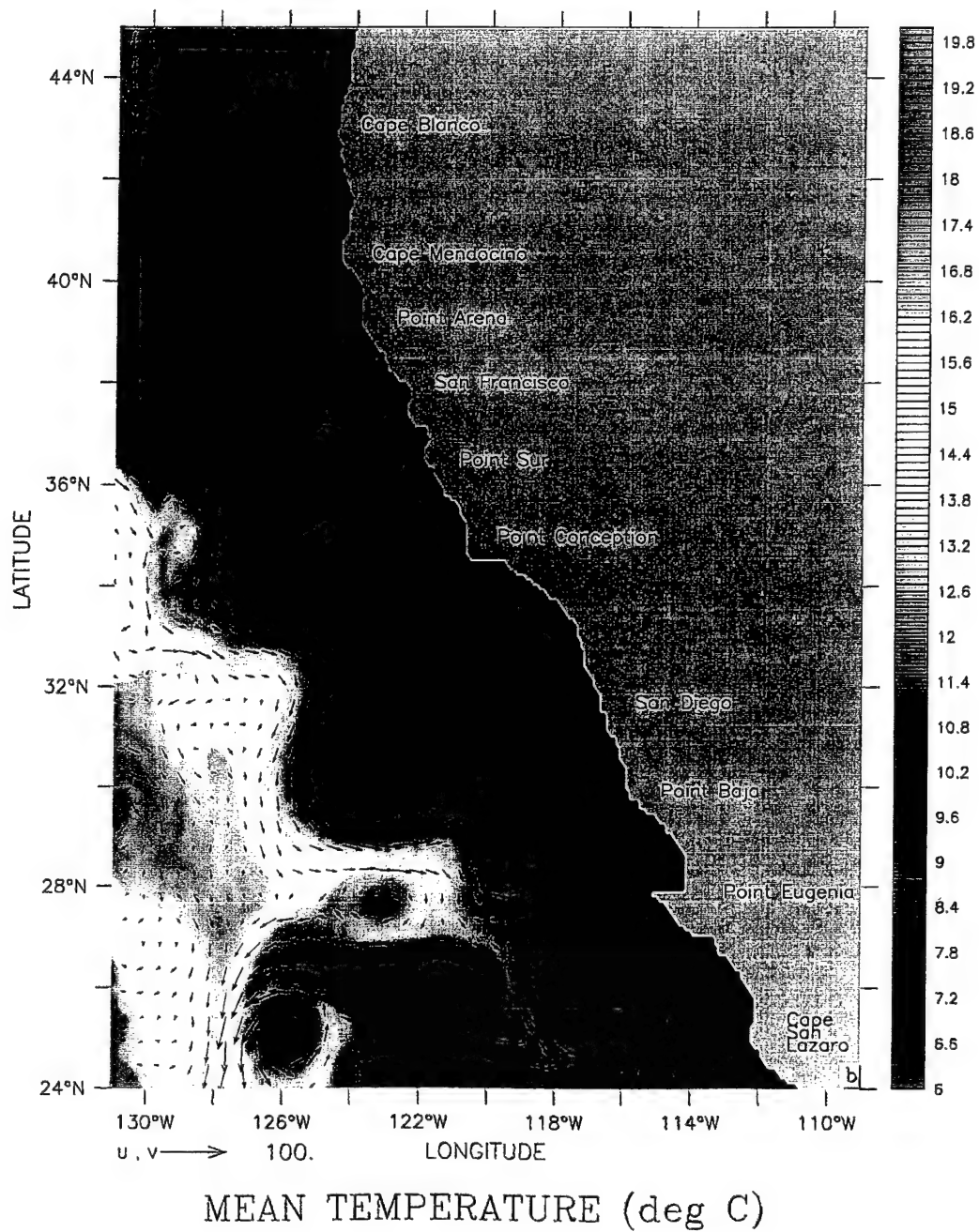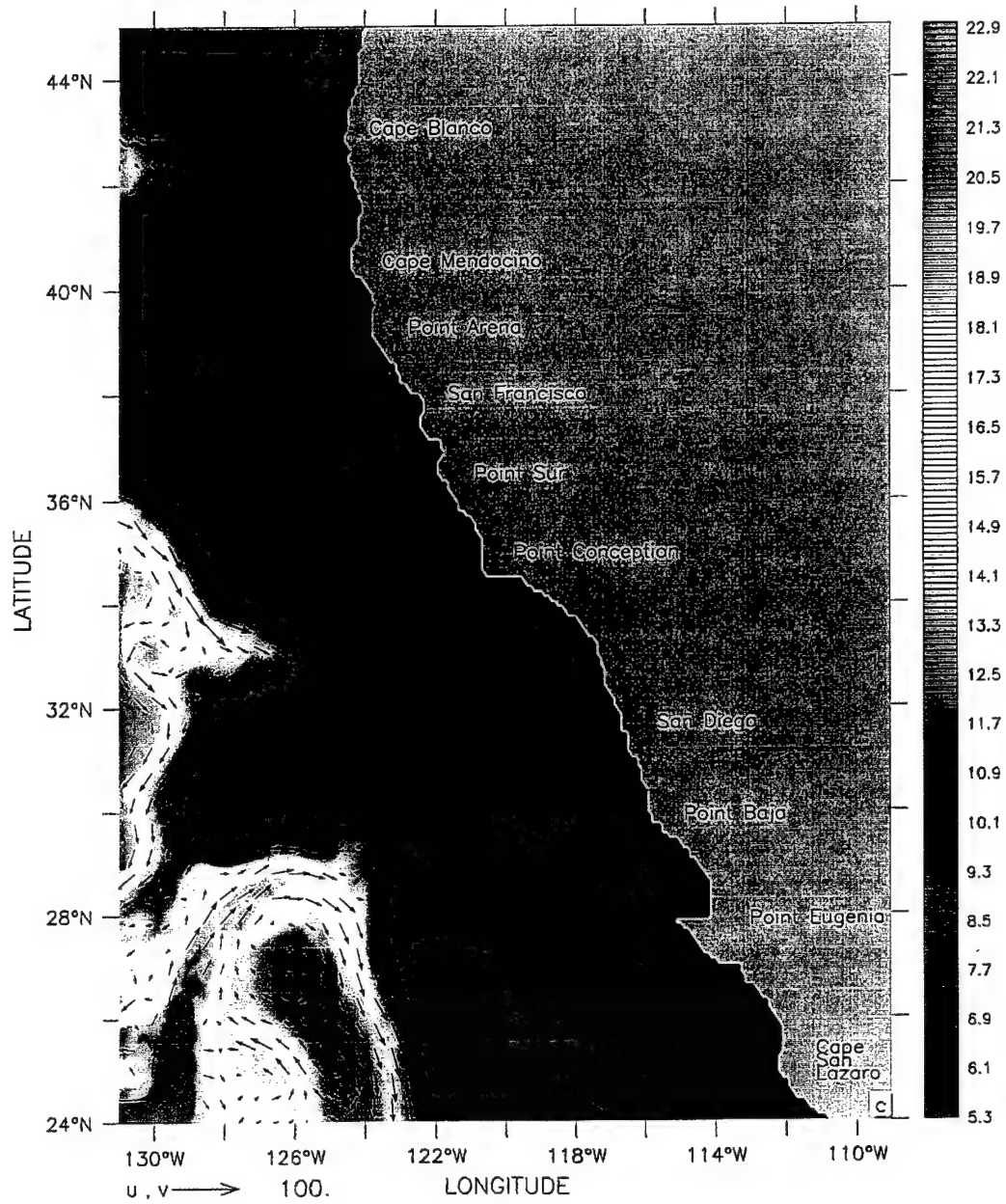
DEPTH : 13m

MEAN TEMPERATURE (deg C)

DEPTH : 13m

MEAN TEMPERATURE (deg C)

88

DEPTH : 13m

MEAN TEMPERATURE (deg C)

89
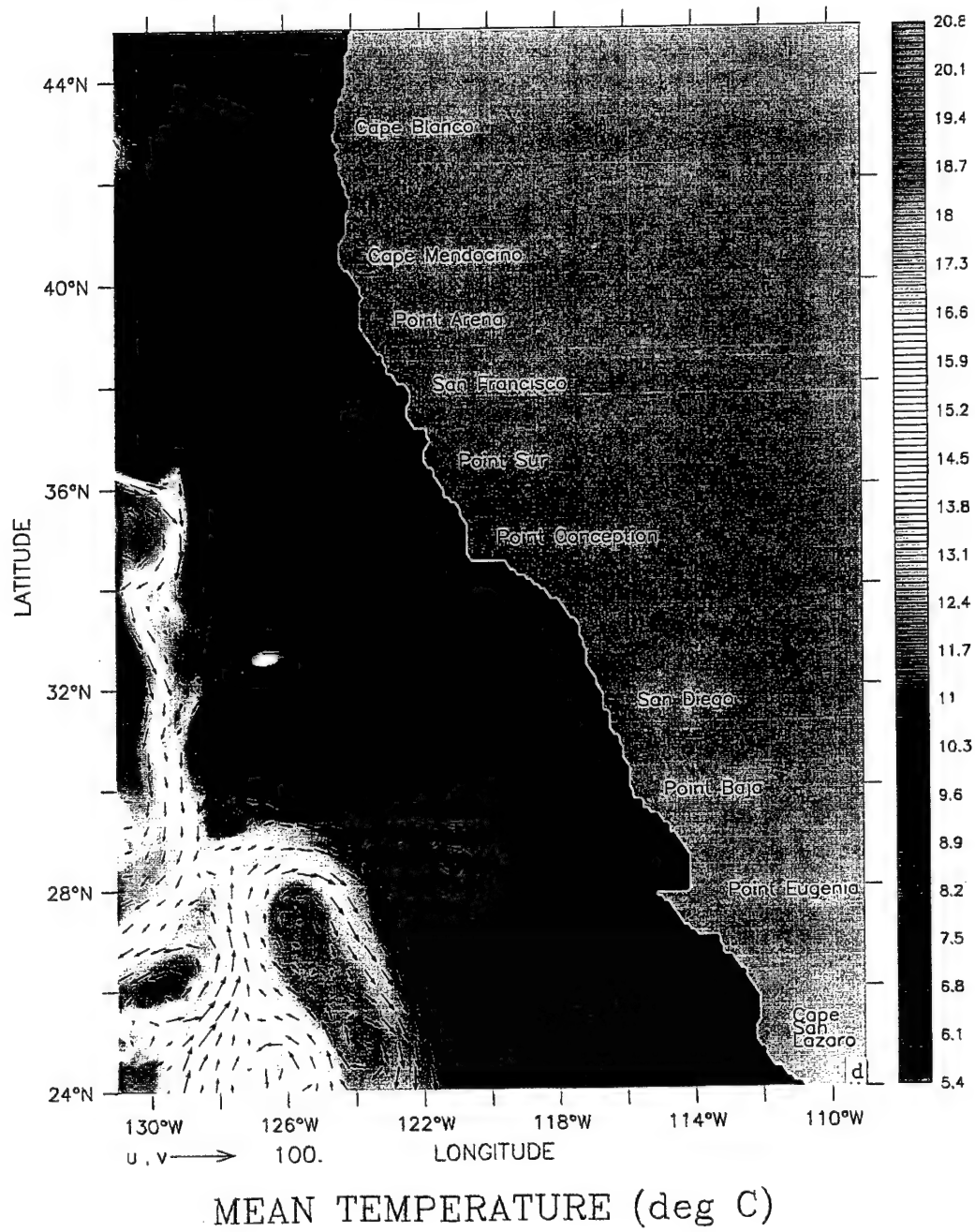
Table 1. Values of Constants Used in the Model

Constant	Value	Definition
T_0	278.2°K	Constant Reference Temperature
S_0	34.7	Constant Reference Salinity
ρ_0	1.0276 gm cm^3	Density of Sea Water At T_0 and S_0
α	2.4×10^{-4} (°K)$^{-1}$	Thermal Expansion Coefficient
β	7.5×10^{-4}	Saline Expansion Coefficient
K	10	Number of Levels In Vertical
Δx	9.0×10^5 cm	Cross-Shore Grid Spacing
Δy	1.1×10^6 cm	Alongshore Grid Spacing
H	4.5×10^5 cm	Total Ocean Depth
Δt	800 s	Time Step
f_0	0.86×10^4 s^{-1}	Mean Coriolis Parameter
g	980 cm s^2	Acceleration of Gravity
A_M	2×10^{17} cm^4 s^{-1}	Biharmonic Momentum Diffusion Coefficient
A_H	2×10^{17} cm^4 s^{-1}	Biharmonic Heat Diffusion Coefficient
K_M	0.5 cm^2 s^{-1}	Vertical Eddy Viscosity
K_H	0.5 cm^2 s^{-1}	Vertical Eddy Conductivity

LIST OF REFERENCES

Arakawa, A., and V.R. Lamb (1977) Computational design of the basic dynamical processes of the UCLA general circulation model. In, *Methods in Computational Physics*, J. Chang, editor, Academic Press, 17, pp. 173-265.

Bakun, A. and C.S. Nelson (1991) The seasonal cycle of wind stress curl in subtropical eastern boundary current regions, *Journal of Physical. Oceanography*, 21, 1815-1834.

Barth, J.A., and R.L. Smith (1996) Separation of a coastal upwelling jet and pathways for cross-shelf exchange: a Lagrangian perspective, *EOS, Transactions of the American Geophysical Union*, Ocean Sciences Meeting supplement, OS 130.

Barth, J.A., and R.L. Smith (1996) Coastal ocean circulation off Oregon: recent observations of spatial and temporal variability, in *Estuarine and Ocean Survival of Northeastern Pacific Salmon: A Workshop and Extended Abstracts*, NOAA Technical Memorandum, NMFS, NWFSC.

Barth, J.A., R.L. Smith, and A. Huyer (1994) Separation of a coastal jet and cyclogenesis during coastal upwelling, *EOS, Transactions of the American Geophysical Union*, 1994 Fall Meeting supplement, 345.

Batteen, M. L. (1997) Wind-forced modeling studies of currents, meanders, and eddies in the California Current System. *Journal of Geophysical Research*, 102, 985-1009.

Batteen, M. L., C. A. Collins, C. R. Gunderson, and C. S. Nelson (1995) The effect of salinity on density in the California Current System. *Journal of Geophysical Research*, 100, 8733-8749.

Batteen, M.L., and Y.-J. Han (1981) On the Computational noise of finite-difference schemes used in ocean models. *Tellus*, 33, 387-396.

Batteen, M.L., R.L. Haney, T.A. Tielking, and P.G. Renaud (1989) A numerical study of wind forcing of eddies and jets in the California Current System. *Journal of Marine Research*, 47, 493-523.

Batteen, M.L., M.J. Rutherford, and E.J Bayler (1992) A numerical study of wind and thermal forcing effects on the ocean circulation off Western Australia. *Journal of Physical Oceanography*, 22, 1406-1433.

Batteen, M.L., and P.W. Vance (1998) Modeling studies of the effects of wind forcing and thermohaline gradients in the California Current System, *Deep-Sea Research*, in press.

Bernstein, R.L., L.C. Breaker, and R. Whritner (1977) California Current eddy formation: Ship, air, and satellite results. *Science*, 195, 353-359.

Brink, K.H., and T.J. Cowles (1991) The Coastal Transition Zone program. *Journal of Geophysical Research*, 96, 14,637-14647.

Camerlengo, A.L. and J.J. O'Brien (1980) Open boundary conditions in rotating fluids. *Journal of Computational Physics*, 35, 12-35.

Chelton, D. B. (1984) Seasonal variability of alongshore geostrophic velocity off central California. *Journal of Geophysical Research*, 89, 3473-3486.

Davis, R.E. (1985) Drifter observations of coastal surface currents during CODE: The method and descriptive view. *Journal of Geophysical Research*, 90, 4741-4755.

Han, Y.-J., (1975) Numerical simulation of mesoscale eddies. Ph.D. thesis, University of California, Los Angles, 154 pp.

Haney, R.L. (1974) A numerical study of the response of an idealized ocean to large-scale surface heat and momentum flux. *Journal of Physical Oceanography*, 4, 145-167.

Hickey, B.M. (1979) The California Current System-Hypotheses and facts. *Progress in Oceanography*, 8, 191-279.

Hickey, B.M., (1998) Coastal Oceanography of Western North America, From the Tip of Baja California to Vancouver Island. In: *The Sea*, Volume 11, John Wiley and Sons Inc., New York, 345-393.

Holland, W.R. (1978) The role of mesoscale eddies in the general circulation of the ocean-numerical experiments using a wind-driven quasi-geostrophic model. *Journal of Physical Oceanography*, 8, 363-392.

Holland, W.R., and M.L. Batteen (1986) The parameterization of subgrid scale heat diffusion in eddy-resolved ocean circulation models. *Journal of Physical Oceanography*, 16, 200-206.

Holland, W.R., D.E. Harrison, and A.J. Semtner Jr. (1983) Eddy-resolving numerical models of large-scale ocean circulation. In: *Eddies in Marine Science*, Springer-Verlag, New York, pp. 379-403.

Huyer, A., and R.L. Smith (1974) A subsurface ribbon of cool water over the continental shelf off Oregon, Journal *of Physical Oceanography, 4*, 381-391.

Ikeda, M., L.A. Mysak, and W.J. Emery (1984) Observations and modeling of satellite-sensed meanders and eddies off Vancouver Island. *Journal of Physical Oceanography,* 14, 3-21.

Kelly, K.A., R.C. Beardsley, R. Lineburner, K.H. Brink, J.D. Paduan, and T.K. Chereskin (1998) Variability of near-surface eddy kinetic energy in the California Current based on altimetric, drifter, and moored current data. *Journal of Geophysical Research,* in press.

Levitus, S. R., Burgett, and T. P. Boyer (1994) World Ocean Atlas 1994, Volume 3: Salinity, *NOAA Atlas NESDI 3*, U. S. Department of Commerce, Washington D.C., 99 pp.

Levitus, S., and T. P. Boyer (1994) World Ocean Atlas 1994, Volume 4: Temperature. *NOAA Atlas NESDI 4*, U. S. Department of Commerce, Washington, D. C., 117 pp.

Lynn, R.S. and J.J. Simpson (1987) The California Current System: The seasonal variability of its physical characteristics. *Journal of Geophysical Research*, 92, 12947-12966.

Niiler, P.P., P.-M. Poulain, and L.R. Haury (1989) Synoptic three-dimensional circulation in an onshore-flowing filament of the California Current, *Deep-Sea Research*, 36(3), 385-405.

Pavlova, Y.V. (1966) Seasonal variations in the California Current, *Oceanology*, 6, 806-814.

Poulain, P.-M. (1990) Near-inertial and diurnal motions in the trajectories of mixed layer drifters, *Journal of Marine Research*, 48, 793-823.

Poulain, P.-M., and P.P. Niiler (1989) Statistical Analysis of the Surface Circulation in the California Current System Using Satellite-Tracked Drifters. *Journal of Physical Oceanography*, 19(10), 1588-1603.

Reid, J.L., Jr. (1963) Measurements of the California Countercurrent off Baja California. *Journal of Geophysical Research*, 68, 4819-4822.

93

Reid, J.L. Jr., G.I. Roden, and J.G. Wyllie (1958) Studies of the California Current System, *CalCOFI Rep. 6*, California Cooperative Oceanic Fisheries Investigation, La Jolla, pp. 27-56.

Semtner, A.J., and Y. Mintz (1977) Numerical simulation of the Gulf Stream and midocean eddies. *Journal of Geophysical Research*, 7, 208-230.

Strub, P.T., T.K., Chereskin, P.P. Niiler, C. James and M.D. Leveine, (1995) Altimeter-derived variability of surface velocities in the California Current System, 1, Evaluation of TOPEX altimeter velocity resolution, *Journal of Geophysical Research*, 102, 727-748.

Strub, P.T., P.M. Kosro, A. Huyer, and CTZ Collaborators (1991) The nature of the cold filaments in the California Current System, *Journal of Geophysical Research*, 96, 14743-14768.

Strub, P.T., and C. James (1995) The large-scale summer circulation of the California Current, *Geophysical Research Letters.*, 22, 207-210.

Trenberth, K.E., W.G. Large, J.G. Olsen (1990) The mean annual cycle in global ocean wind stress, *Journal of Physical Oceanography*, 20, 1742-1760.

Weatherly, G.L. (1972) A study of the bottom boundary layer of the Florida Current, *Journal of Physical Oceanography*, 2, 54-72.

Wooster, W.S., and J.L. Reid, Jr. (1963) Eastern Boundary Currents. in *The Sea*, Vol. 2, M. N. Hill, Editors, Wiley International, New York, 253-280.

INITIAL DISTRIBUTION LIST

No. Copies

1. Defense Technical Information Center...2
    8725 John J. Kingman Rd, STE 0944
    Ft. Belvoir, VA 22060-6218

2. Dudley Knox Library...2
    Naval Postgraduate School
    411 Dyer Rd
    Monterey, CA 93943-5101

3. Chairman (Code OC/Bf)..1
    Department of Oceanography
    Naval Postgraduate School
    Monterey, CA 93943-5122

4. Chairman (Code MR/Wx)..1
    Department of Meteorology
    Naval Postgraduate School
    Monterey, CA 93943-5114

5. Dr. Mary L. Batteen, (Code OC/Bv).. 3
    Department of Oceanography
    Naval Postgraduate School
    Monterey, CA 93943-5122

6. Dr. Curtis A. Collins, (Code OC/Co)..1
    Department of Oceanography
    Naval Postgraduate School
    Monterey, CA 93943-5122

7. Dr. Tom Curtin.. 1
    Office of Naval Research
    800 N. Quincy Street
    Arlington, VA 22217

8. Dr. T. Kinder..1
    Physical Oceanography Division
    Office of Naval Research
    800 N. Quiney Street
    Arlington, VA 22217

    2201 Halfmoon Crescent
    Virginia Beach, VA 23454